



HAL
open science

Multimodal Image Registration in Image-Guided Prostate Brachytherapy

Iyas Hamdan

► **To cite this version:**

Iyas Hamdan. Multimodal Image Registration in Image-Guided Prostate Brachytherapy. Signal and Image processing. Ecole nationale supérieure Mines-Télécom Atlantique, 2017. English. NNT : 2017IMTA0002 . tel-01878416

HAL Id: tel-01878416

<https://theses.hal.science/tel-01878416>

Submitted on 21 Sep 2018

HAL is a multi-disciplinary open access archive for the deposit and dissemination of scientific research documents, whether they are published or not. The documents may come from teaching and research institutions in France or abroad, or from public or private research centers.

L'archive ouverte pluridisciplinaire **HAL**, est destinée au dépôt et à la diffusion de documents scientifiques de niveau recherche, publiés ou non, émanant des établissements d'enseignement et de recherche français ou étrangers, des laboratoires publics ou privés.



IMT Atlantique
Bretagne-Pays de la Loire
École Mines-Télécom

**UNIVERSITÉ
BRETAGNE
LOIRE**

THÈSE / IMT Atlantique

sous le sceau de l'Université Bretagne Loire
pour obtenir le grade de

DOCTEUR D'IMT Atlantique

*Mention : Sciences et Technologies de l'Information
et de la Communication*

École Doctorale Sicma

Présentée par

Iyas Hamdan

Préparée dans le département Image et traitement de
l'information

Laboratoire Latim

Multimodal Image Registration in Image-Guided Prostate Brachytherapy

Thèse soutenue le 17 janvier 2017

devant le jury composé de :

Chafiaa Hamitouche

Professeure, IMT Atlantique / présidente

Nacim Betrouni

Chargé de recherche (HDR), Inserm - CHRU de Lille / rapporteur

Jocelyne Troccaz

Directrice de recherche (HDR), TIMC-IMAG – Université Grenoble Alpes / rapporteur

Dimistris Visvikis

Directeur de recherche, Latim / directeur de thèse

Guillaume Dardenne

Ingénieur de recherche, Latim / invité

Julien Bert

Ingénieur de recherche, Latim / invité

Résumé

Le cancer de la prostate est le cancer le plus fréquent chez l'homme en France et dans les pays occidentaux. Il est la troisième cause de décès liés au cancer, étant responsable d'environ 10% des morts, soit 9000 morts en France en 2015. Cependant, le taux de mortalité a diminué depuis les années 2000, ce qui est fortement lié aux progrès du traitement. Par conséquent, les programmes de dépistage et de diagnostic sont d'un grand intérêt afin de détecter le cancer à un stade précoce.

En général, le cancer de la prostate peut être détecté suivant différentes techniques. Une fois le cancer détecté, plusieurs techniques de traitement peuvent être appliquées. Les principaux traitements sont la chirurgie, la radiothérapie externe et la curiethérapie. Une surveillance active peut également être envisagée. La modalité de traitement ou de surveillance du cancer est déterminée en fonction des bénéfices et risques associés à chaque méthode et selon l'état du patient.

La curiethérapie est liée à une meilleure qualité de vie après le traitement, par rapport aux autres méthodes de traitement. La curiethérapie de la prostate consiste à insérer des sources radioactives dans la prostate, soit temporairement soit en permanence, afin de délivrer une dose d'irradiation localisée à la tumeur tout en protégeant les tissus sains environnants. Les techniques principales de curiethérapie sont le bas débit de dose (low dose rate LDR), et le haut débit de dose (high dose rate HDR). En curiethérapie LDR, les sources radioactives sont insérées de manière permanente dans la tumeur, alors qu'en curiethérapie HDR, une seule source est déplacée dans plusieurs positions dans le patient par l'intermédiaire de guides.

En curiethérapie de la prostate, la distribution de dose est calculée systématiquement en se basant sur le formalisme TG-43. Ce formalisme considère le patient comme un milieu homogène constitué d'eau, ce qui est lié à plusieurs approximations; telles que l'homogénéité des tissus et l'absence de l'atténuation entre les sources radioactives. Ces hypothèses ne sont pas précises, et

risquent de donner des estimations de dose non optimales. Afin d'améliorer la précision du planning, des images Tomodensitométriques préopératoires, appelées Computed Tomography (CT), peuvent être utilisées pour calculer une distribution personnalisée et plus précise de dose. Une fois les positions des sources déterminées, le médecin place ces sources dans leurs positions souhaitées à l'aide des images échographiques acquises par une sonde endorectale introduite dans le rectum du patient, transrectal ultrasound (TRUS). Par conséquent, comme les positions des sources sont déterminées sur l'image CT, elles doivent être transférées à l'image US. Cependant, un recalage US/CT direct et robuste est difficilement envisageable parce que les tissus mous, telle que la prostate, offrent peu de contraste en CT et en US. En revanche, l'Imagerie par Résonance Magnétique (IRM) fournit un meilleur contraste et peut, potentiellement, améliorer le traitement en améliorant la visualisation. Donc, ces trois modalités (IRM, CT et US) doivent être correctement alignées.

Le développement d'un algorithme du recalage qui aligne ces trois modalités est un problème difficile, étant donné la nature différente de ces images. En plus, ces trois modalités ne sont pas acquises simultanément, et sur différents scanners, ce qui implique différents remplissages du rectum et de la vessie ainsi que le mouvement du patient. Par conséquent, la prostate sera déformée entre les différentes acquisitions. Sans compter que lors de l'intervention, la prostate subit des déformations importantes à cause de l'insertion des aiguilles et la pression de la sonde. Pour compenser ces déformations, un recalage non-rigide est nécessaire. La précision globale de ce recalage a un impact très important sur la planification et le guidage du traitement. En effet, ce recalage devrait détecter avec précision les déformations de la prostate afin de fournir la position exacte de la tumeur; permettant de délivrer une dose élevée à la tumeur tout en protégeant les tissus sains environnants. Par conséquent, un recalage précis est nécessaire. Une méthode de recalage entièrement automatique est également souhaitée, afin de faciliter son intégration en routine clinique.

Dans ces travaux de thèse, nous proposons d'appliquer un premier recalage est donc appliqué entre les images IRM/CT dans la phase préopératoire pour la planification du traitement. Ensuite, un deuxième recalage US/IRM dans la phase peropératoire, pendant l'intervention. Les deux méthodes de recalage doivent être combinées pour former une solution complète pour la curiethérapie de la prostate guidée par l'image.

Dans le deuxième chapitre de cette thèse, nous nous concentrons sur le recalage IRM/CT. Les méthodes de recalage dédiées à la curiethérapie de la prostate proposées dans la littérature sont soit limitées aux transformations rigides seulement, elles exigent l'insertion des marqueurs dans la prostate, soit elles nécessitent une étape manuelle (identifier des points de repère anatomiques ou segmenter la prostate). Cette étape prend beaucoup de temps et est soumise à des inexactitudes de variabilités inter- et intra-observateur en fonction de l'expérience de l'utilisateur.

Nous proposons donc un recalage non rigide entre les images IRM et les images CT. Ce recalage est complètement automatique et n'exige pas d'interaction manuelle. L'approche proposée se fait en plusieurs étapes. Au début, et afin d'améliorer la robustesse et le temps de calcul, nous proposons de contraindre le recalage sur des volumes d'intérêt (VOIs). Ensuite, un premier recalage affine est appliqué pour aligner globalement les deux images. Ce recalage est également utilisé comme une initialisation pour un deuxième recalage non-rigide basé sur l'utilisation des B-Splines qui est censé détecter les déformations locales de la prostate. En ce qui concerne les VOIs, ils ont été automatiquement déterminés en détectant tout d'abord la position de la prostate. Pour cela, un algorithme de rendu volumique (MIP pour maximum intensity projection) est appliqué afin d'améliorer la visualisation des os et des structures d'atténuations élevées dans le CT. A partir de cet image, et en se basant sur l'anatomie du pelvis, la coupe contenant la prostate ainsi que différentes structures osseuses peut être automatiquement détectée et extraite du CT. Une méthode de seuillage automatique (Otsu's thresholding) est ensuite appliquée sur cette coupe suivie par des opérations morphologiques pour séparer les os et les tissus mous et supprimer tous les artéfacts restant dans l'image, respectivement. Ensuite, un seuillage basé sur les unités Hounsfield est utilisé pour enlever les tissus mous et ne garder que les os dans l'image. Des algorithmes de connected-component labelling sont appliqués par la suite pour détecter les contours et les différents labels dans l'image. Finalement, un volume, déterminé autour du pelvis, est utilisé pour contraindre le recalage affine, alors qu'un volume autour la prostate seulement est utilisé pour le deuxième recalage non-rigide.

Pour les deux étapes (affine et non-rigide), un recalage basé intensité est utilisé malgré le fait que les images sont issues de différentes modalités et, par conséquent, leurs intensités n'ont pas de relation simple. Néanmoins, ces modalités sont informatives de la même anatomie, ce qui signifie qu'elles contiennent des informations mutuelles entre elles. Un critère de similarité appelé information mutuelle (MI pour mutual information) est donc utilisé pour calculer le degré de

dépendance entre les images IRM et CT. Le MI est calculé directement à partir des valeurs des voxels plutôt que des structures géométriques, telles que les points de repère ou les surfaces. Donc, ce critère ne nécessite aucune interaction manuelle, ce qui facilite l'automatisation de ce recalage.

La transformation qui maximise l'information mutuelle entre les deux images est déterminée itérativement en utilisant un optimiseur de descente de gradient à pas régulier (regular step gradient descent optimiser en anglais). Cet optimiseur est une forme de descente de gradient, qui évite de prendre des pas trop grand. Une fois la transformation qui aligne les deux images est déterminée, elle est appliquée sur une de ces deux images (le CT dans notre cas). Afin de calculer l'intensité de cette image à des positions non rigides, un interpolateur est utilisé. L'image déformée est donc rééchantillonnée sur la grille de l'image fixe en utilisant un mapping inverse. En ce qui concerne l'efficacité de temps de calcul, la méthode du recalage préopératoire prend en moyenne 2.0 ± 0.25 minutes pour donner des résultats sur une machine Intel® Core™ i7-3840QM CPU @ 2.80 GHz. Puisque cette méthode est réalisée dans la phase préopératoire, avant l'intervention, elle est donc compatible avec les contraintes de temps en routine clinique.

Concernant le deuxième recalage entre US/IRM dans la phase peropératoire, qui est le troisième chapitre de cette thèse, les méthodes dédiées à la prostate (biopsie ou curiethérapie) proposées dans la littérature sont soit limitées aux transformations rigides seulement, soit elles nécessitent une étape manuelle comme pour le recalage entre IRM/CT. Cette étape prend beaucoup de temps et est soumise à des inexactitudes en fonction de l'expérience de l'utilisateur. Quelques méthodes dans la littérature utilisaient un recalage basé intensité. Cependant, une interaction manuelle était toujours nécessaire afin d'initialiser le recalage, soit le recalage était limité à des transformations rigides seulement. Une nouvelle méthode de recalage US/IRM a été proposée pour les applications de neurochirurgie guidées par l'image. Il s'agit de mettre en corrélation l'intensité de l'image US avec l'intensité de l'image IRM, mais également avec son gradient. Ce critère de similarité est appelé le LC^2 (linear correlation of linear combination).

Les images US sont généralement appelées des images de gradient, car ses images sont essentiellement liées aux interfaces entre les différentes structures. L'amplitude de l'écho est proportionnelle à la différence entre les impédances acoustiques des couches de tissu successives. Par conséquent, l'intensité de l'image US devrait être élevée aux interfaces entre les différents tissus et zéro dans le même tissu. Cependant, ce n'est pas vraiment le cas puisqu'il peut y avoir

des réflexions dans le même tissu à cause des petites inhomogénéités. Par conséquent, ces ondes entrantes et sortantes forment un bruit dans l'image, appelé speckle. Les régions homogènes par conséquent apparaissent dans les images US avec une intensité moyenne non nulle. Puisque ces réflexions sont presque invisibles dans l'IRM, elles doivent être prises en compte lors du recalage. C'est pour cela que cette méthode propose de mettre en corrélation l'intensité de l'image US avec l'intensité et le gradient de l'image IRM. Par contre, une initialisation manuelle reste nécessaire, et de plus le recalage est basé sur une transformation rigide.

L'amélioration de cette méthode a été proposée dans la thèse en incluant des transformations non rigides pour des applications dédiées à la prostate.

Nous proposons donc un recalage non rigide entre les images US et les images IRM pour la curiethérapie de la prostate. L'approche proposée peut également être appliqué dans des applications dédiées à la biopsie de la prostate, où un recalage entre les images US et IRM est également nécessaire. Ce recalage est complètement automatique et n'exige aucune interaction manuelle. Au début, et afin d'améliorer la robustesse et le temps de calcul, nous proposons de contraindre le recalage sur des VOIs. Ensuite, un premier recalage affine est appliqué pour aligner globalement les deux images, et initialiser un deuxième recalage non-rigide, basé sur B-Splines, afin de détecter les déformations locales de la prostate. Vu que les déformations de la prostate lors de l'intervention sont importantes, nous utilisons une approche multi-résolution pour éviter les minima locaux et améliorer le temps de calcul.

En ce qui concerne les VOIs, un VOI autour la prostate a été déterminé automatiquement pour chaque modalité. Pour l'image IRM, le même VOI qui a été utilisé pour le recalage non rigide dans la phase préopératoire est utilisé également pour le recalage peropératoire. Ce VOI a été déterminé sur l'image CT, mais il peut être projeté sur l'image IRM, puisque le CT et l'IRM sont déjà alignés avant l'intervention. Quant au VOI utilisé pour l'image US, sa détermination se fait en plusieurs étapes. Tout d'abord, la coupe centrale du volume US est extraite. A partir de cette coupe, les contours de la prostate sont détectés automatiquement en utilisant la méthode de radial bas-relief (RBR). Cette méthode consiste à superposer l'image originale sur l'image négative, légèrement décalée. Ensuite, une bounding box est définie autour de ces contours, représentant le VOI sur l'image US.

Pour les deux étapes du recalage peropératoire (affine et non-rigide), un recalage basé intensité est utilisé avec le LC^2 comme critère de similarité. Pour chaque pixel de l'image, le LC^2 local est

calculé, considérant une région d'intérêt centré sur ce pixel. Ensuite, le LC^2 global est calculé en utilisant la moyenne pondérée des mesures locales calculées pour chaque pixel de l'image. Les poids étant les écarts type des régions d'intérêt autour de chaque pixel dans l'image US.

La transformation qui maximise ce critère entre les images US et les images IRM est déterminée itérativement en utilisant un optimiseur. Etant donné que la dérivé de cette fonction de coût est difficile à calculer, un optimiseur qui n'exige pas les dérivés est considérée pour ce recalage; Amoeba (nelder-mead downhill simplex). Cet optimiseur a plusieurs avantages par rapport aux autres optimiseurs, étant plus robuste, facile à implémenter, et en plus, la probabilité de tomber sur un maxima locaux est minimale. Une fois la transformation qui aligne les deux images est déterminée, elle sera appliquée sur une de ces deux images (l'IRM dans notre cas). Afin de calculer l'intensité de cette image à des positions non rigides, un interpolateur est utilisé. L'image déformée est donc rééchantillonnée sur la grille de l'image fixe en utilisant un mapping inverse.

En ce qui concerne l'efficacité de temps de calcul, la méthode du recalage peropérateur prend en moyenne 2.75 ± 0.25 heures pour donner des résultats sur une machine Intel® Core™ i7-3840QM CPU @ 2.80 GHz. Puisque cette méthode est réalisée dans la phase peropérateur, au cours de l'intervention, elle doit être compatible avec les contraintes de temps au bloc opératoire. Le LC^2 est calculé pour chaque pixel de l'image indépendamment des résultats sur les autres pixels, son calcul peut donc être parfaitement parallélisable. Par conséquent, une solution basée sur l'utilisation des cartes graphiques (GPU pour graphics processing unit) a le potentiel d'améliorer ce temps de calcul. Une première estimation a consisté à trouver la transformation qui aligne des images US et IRM 2D, où seul le calcul du LC^2 est implémenté sur GPU et le reste du processus de recalage reste sur le CPU. Dans le cas d'images 2D, le calcul du LC^2 , pour une seule itération, a pris 3.23 secondes sur CPU. Une première version non optimale sur GPU (NVIDIA TITAN X Pascal, contenant 3584 cores) a donné les mêmes résultats en 80 ms, soit un facteur de x40. Par conséquent, en faisant une extrapolation sur la totalité de la procédure de recalage, le temps de calcul pourrait être potentiellement réduit à 3.75 minutes en utilisant une seule carte graphique. Compte tenu de la possibilité d'utiliser 4 GPUs dans une station de travail, ce temps de calcul pourrait donc être réduit à 56 secondes. Le calcul du LC^2 a été implémenté sur GPU avec une version non optimisée. Don, cette implémentation pourrait encore être optimisée afin d'améliorer davantage le temps de calcul.

Finalement, dans le quatrième chapitre de cette thèse, les deux méthodes de recalage (pré et peropératoire) ont été validées en utilisant des critères d'évaluation qualitatifs et quantitatifs. Concernant le recalage IRM/CT préopératoire, des jeux de données cliniques sont utilisés pour la validation. Quant au recalage US/IRM peropératoire, la méthode a été d'abord validée sur un fantôme de la prostate pour évaluer sa faisabilité et, par la suite, elle a été validée sur des jeux de données cliniques.

Etant donné que la représentation anatomique de la prostate dans les images de fantôme est beaucoup plus simple que celle dans les vrais patients (notamment les tissus hétérogènes), un fantôme de la prostate est utilisé pour l'évaluation préliminaire de la faisabilité et de la précision de la méthode. Ce fantôme doit modeler la prostate et imiter son mouvement; donc un fantôme réaliste et déformable est nécessaire. Vu la nature différente des images US et IRM (notamment le bruit speckle présent dans les images US), deux fantômes synthétiques différents ont été fabriqués et testés; un pour chaque modalité. Une acquisition IRM (T1) est ensuite faite sur la plateforme Neurinfo, située dans le centre hospitalier universitaire (CHU) de Rennes. Des acquisitions US sont également faites sur la plateforme Ultrasonix au LaTIM - CHU de Brest en utilisant une sonde TRUS endorectale.

En ce qui concerne les jeux de données cliniques, le recalage IRM/CT est validé sur 8 patients traités par une curiethérapie de la prostate. Pour chaque patient, les images IRM et CT sont acquises dans la phase préopératoire avec un certain temps entre les deux acquisitions (l'IRM est faite pour le diagnostic alors que le CT est fait pour le planning du traitement). Les images ont été acquises dans deux centres différents, CHU de Brest et CHU de Poitier, et en utilisant des systèmes d'acquisitions différents.

D'une autre part, et après avoir validé le recalage US/IRM sur un fantôme de la prostate, il a été validé sur 3 jeux de données cliniques. Pour chaque patient, les images IRM sont acquises dans la phase préopératoire dans des cliniques externes, tandis que les images US sont acquises dans la phase peropératoire pendant l'intervention au CHU de Brest.

Puisqu'il n'y avait pas de vérité terrain pour évaluer le recalage, une première évaluation a été faite en utilisant une approche de segmentation. Un expert a manuellement segmenté la prostate dans les deux images, après le recalage. Une évaluation visuelle du chevauchement des frontières de la prostate a été considérée pour évaluer le recalage. Pour tous les jeux de données, les résultats étaient visuellement acceptables et aucun décalage résiduel n'a pu être observé. Les

contours de la prostate, après le recalage, étaient continus entre les deux images à recaler, indiquant que la méthode était capable d'aligner ces images.

Ensuite, et pour évaluer quantitativement le chevauchement des contours de la prostate, ces contours ont été utilisés pour déterminer la bounding box qui englobe la segmentation manuelle de la prostate dans les deux images, après le recalage. La comparaison entre ces boxes a montré de bons résultats en termes de taille, avec des différences de moins d'un seul voxel.

Par la suite, et pour déterminer quantitativement le degré de chevauchement entre les contours de la prostate dans les deux images, après le recalage, la distance Hausdorff a été utilisée. Le décalage moyenne entre les contours de la prostate dans les images IRM et CT après le recalage non rigide était de 1.15 ± 0.20 mm. Pour le recalage US/IRM, cette valeur était de 1.44 ± 0.06 mm. Quant à la valeur maximale de l'erreur de décalage entre les contours de la prostate dans les deux images, cette valeur était toujours inférieure à 2 mm dans tous les cas pour les deux recalages pré- et peropératoire, ce qui répond à la précision clinique désirée.

Finalement, l'indice de sorensen-dice (DSC pour dice similarity coefficient) a été également utilisé pour déterminer le degré de chevauchement entre les contours de la prostate dans les deux images après le recalage. DSC était égal à 0.96 et 0.97 pour le recalage préopératoire et peropératoire, respectivement, sachant que la valeur de DSC se situe entre 0 (pas de chevauchement) et 1 (chevauchement complet).

Pour conclure, l'approche proposée dans ce travail permet d'aller vers un protocole de curiethérapie guidée par l'imagerie multimodale qui puisse améliorer la précision globale de cette procédure en explorant l'information fournie par des modalités différentes; CT, IRM et US. Un premier module dans la phase préopératoire consiste à aligner les images IRM avec les images CT afin d'améliorer la précision de l'estimation de dose ainsi que la visualisation de cette distribution de dose par rapport à la tumeur. Pendant l'intervention, un deuxième module s'agit d'aligner avec précision les images US peropératoires avec les images IRM préopératoires pour améliorer la visualisation, et par conséquent, le placement des sources radioactives dans leurs positions souhaitées.

L'approche proposée est entièrement automatique afin de faciliter son intégration au bloc opératoire. En plus, cette approche était capable de compenser les déformations de la prostate qui se produisent entre les acquisitions de différentes modalités.

Bien que ce travail ait été dédié à la curiethérapie de la prostate, cette approche peut être potentiellement appliquée dans d'autres applications de radiothérapie guidée par l'image (IGRT pour image-guided radiation therapy), comme la radiothérapie externe, la biopsie et la dosimétrie après l'implantation des sources radioactive (post-implant dosimetry). En IGRT, le CT est généralement utilisé pour calculer une distribution de dose personnalisée. Le CT fournit un bon contraste pour les sources radioactives, par contre les tissus mous sont mal visualisés. L'IRM est donc utilisée de plus en plus dans les applications de l'IGRT grâce à son meilleur contraste des tissus mous qui permet une distinction entre les tissus cancéreux et sains. Donc un recalage entre les images IRM et CT est nécessaire. Concernant le recalage US/IRM, il peut également être appliqué dans d'autres applications telles que la biopsie de la prostate; qui se fait normalement en utilisant l'US. Alors un recalage US/IRM a le potentiel d'améliorer la visualisation et par conséquent la précision de ce traitement.

Malgré ces résultats plutôt encourageants, les travaux futurs impliqueront une évaluation plus approfondie sur plus de jeux de données afin d'évaluer la fiabilité et l'efficacité de cette méthode avant de l'intégrer au bloc opératoire.

Abstract

Prostate cancer is the most common cancer in men in France and western countries. It is the third leading cause of death from cancer, being responsible for around 10% of deaths. Brachytherapy, a radiotherapy technique, is associated with a better health-related quality of life after the treatment, compared to other treatment techniques. Prostate brachytherapy involves the implantation of radioactive sources inside the prostate to deliver a localized radiation dose to the tumor while sparing the surrounding healthy tissues. Multi-modal imaging is used in order to improve the overall accuracy of the treatment. The pre-operative Computed Tomography (CT) images can be used to calculate a personalized and accurate dose distribution. During the intervention, the surgeon utilizes a real-time guiding system, Transrectal Ultrasound (TRUS), to accurately place the radioactive sources in their desired pre-planned positions. Therefore, if the positions of the sources were determined on CT, they need to be transferred to US. However, a robust and direct US/CT registration is hardly possible since they both provide low soft tissue contrast. Magnetic Resonance Imaging (MRI), on the other hand, has a superior contrast and can potentially improve the treatment planning and delivery by providing a better visualization. Thus, these three modalities (MRI, US and CT) need to be accurately registered. To compensate for prostate deformations, caused by changes in size and form between the different acquisitions, non-rigid registration is essential. Fully automatic registration methodology is necessary in order to facilitate its integration in a clinical workflow. At first, we propose a registration between pre-operative MR and CT images based on the maximization of the mutual information in combination with a deformation field parameterized by cubic B-Splines. We propose to constrain the registration to volumes of interest (VOIs) in order to improve the robustness and the computational efficiency. The proposed approach was validated on clinical patient datasets. Quantitative evaluation indicated that the overall registration error was of 1.15 ± 0.20 mm; which satisfies the desired clinical accuracy. Then, we propose a second intra-operative US/MRI registration, where a multi-resolution approach is implemented to reduce the probability of local minima and improve the computational efficiency. A similarity measure, which correlates

intensities of the US image with intensities and gradient magnitude of the MRI, is used to determine the transformation that aligns the two images. The proposed methodology was validated on a prostate phantom at first to assess its feasibility. Subsequently, the method was validated on clinical patient datasets and evaluated using qualitative and quantitative criteria, resulting in a registration error of 1.44 ± 0.06 mm. The approach proposed in this work allows going towards a multimodal protocol for image-guided brachytherapy which can improve the overall accuracy of this procedure. Despite such encouraging results, future work will involve further evaluation on a larger number of datasets in order to assess the reliability and the efficiency of this methodology before integrating it in a clinical workflow.

Contents

1.	<u>Introduction</u>	1
1.1	<u>Prostate Cancer</u>	2
1.1.1	<u>Prostate</u>	2
1.1.2	<u>Risk factors</u>	3
1.1.3	<u>Diagnosis</u>	3
1.1.4	<u>Treatment</u>	6
1.2	<u>Brachytherapy</u>	12
1.2.1	<u>Clinical context</u>	13
1.3	<u>Objectives of the thesis: Image-guided brachytherapy</u>	15
1.4	<u>Conclusion</u>	19
	<u>References</u>	20
2.	<u>Pre-operative MRI/CT Registration</u>	23
2.1	<u>Principles of image registration</u>	23
2.1.1	<u>Classification of registration methods</u>	24
2.1.2	<u>Components of registration</u>	28
2.2	<u>State of the art of MRI/CT registration</u>	30
2.3	<u>Proposed MRI/CT registration approach</u>	33
2.3.1	<u>VOIs determination</u>	34
2.3.2	<u>Registration</u>	40
2.4	<u>Implementation</u>	46
2.5	<u>Conclusion</u>	48
	<u>References</u>	49

3.	<u>Intra-operative US/MRI Registration</u>	53
3.1	<u>State of the art of US/MRI registration</u>	53
3.1.1	<u>Surface-based registration methods</u>	54
3.1.2	<u>Point-based registration methods</u>	56
3.1.3	<u>Intensity-based registration methods</u>	59
3.2	<u>Proposed US/MRI registration approach</u>	61
3.2.1	<u>Optional preprocessing</u>	62
3.2.2	<u>VOIs determination</u>	63
3.2.3	<u>Registration</u>	68
3.3	<u>Implementation</u>	73
3.3.1	<u>GPUs</u>	74
3.3.2	<u>GPU implementation</u>	75
3.4	<u>Conclusion</u>	77
	<u>References</u>	78
4.	<u>Evaluation and Results</u>	81
4.1	<u>Prostate phantom</u>	81
4.1.1	<u>MRI phantom</u>	81
4.1.2	<u>US phantom</u>	83
4.2	<u>Clinical patient datasets</u>	86
4.2.1	<u>Pre-operative MRI/CT registration</u>	86
4.2.2	<u>Intra-operative US/MRI registration</u>	87
4.3	<u>Evaluation metrics</u>	88
4.3.1	<u>Visual assessment</u>	88
4.3.2	<u>Quantitative criteria</u>	88
4.3.3	<u>Reproducibility and robustness</u>	89
4.4	<u>Results</u>	90
4.4.1	<u>Pre-operative MRI/CT registration</u>	90
4.4.1.1	<u>Setting the parameters of the optimizer</u>	90
4.4.1.2	<u>Evaluation metrics</u>	93
4.4.2	<u>Intra-operative US/MRI registration</u>	102

4.4.2.1	Prostate phantom	102
4.4.2.2	Clinical patient datasets	103
A.	Mutual Information	103
B.	LC²	104
C.	Evaluation metrics	106
4.4.3	Final US/CT registration	111
4.5	Conclusion	112
	References	113
5.	Discussion and Conclusion	115
5.1	Pre-operative phase	116
5.2	Intra-operative phase	119
5.3	Conclusion and future work	121
	References	125
	List of figures	127
	List of tables	131
	List of abbreviations and acronyms	132
	List of publications	135

Introduction

Prostate Cancer (PCa) is the second most frequent diagnosed cancer after breast cancer in Europe. Figure 1.1 shows the new cases diagnosed with cancer in Europe in 2012. In France, 385000 new cases were diagnosed with cancer (211000 in men and 174000 in women) in 2015. Breast cancer is the most common cancer in women with 55000 new cases in 2015. PCa, on the other hand, is the most common cancer in men, outnumbering lung and colorectal cancers [1, 2], with 72000 new cases in 2015.

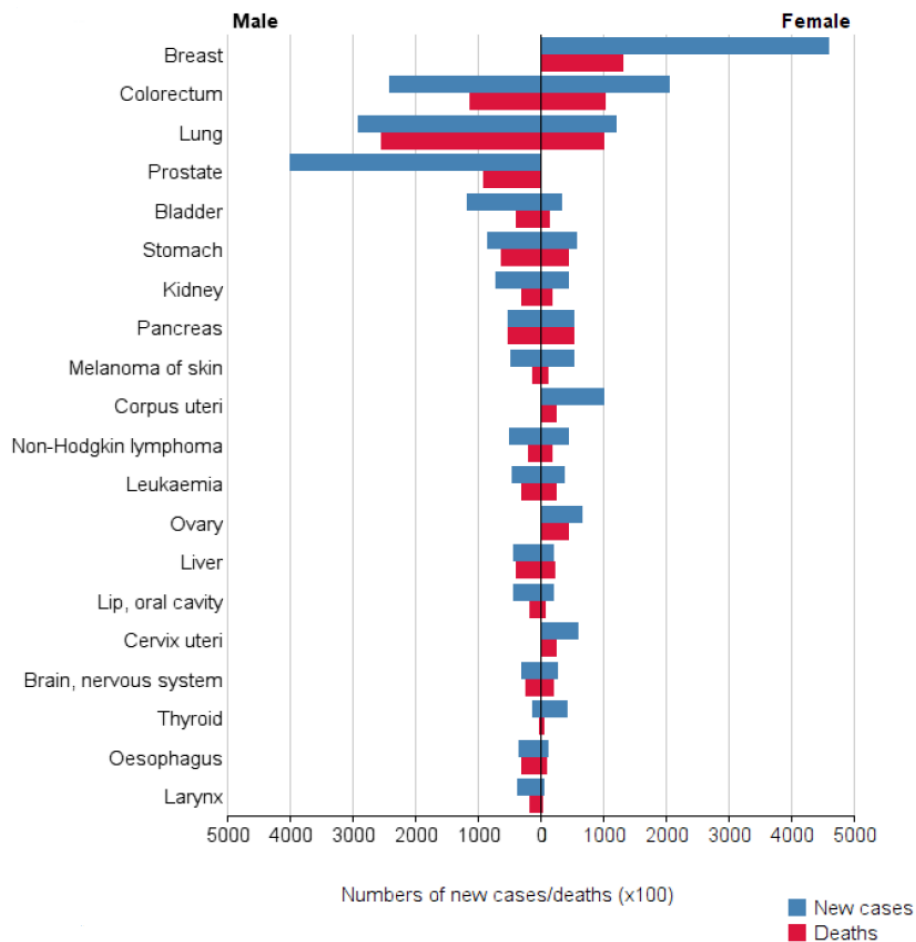


Figure 1.1. New cases diagnosed with cancer in Europe in 2012, image www.globocan.iarc.fr.

Curing PCa is still a challenging public health problem with around 9000 deaths in France in 2015, making it the third leading cause of death from cancer in men. The mortality rate however has declined since 2000, which is highly linked to the advancements in the treatment. Therefore, screening and diagnosis programs are of much interest in order to detect the cancer at early stages since the survival rate is highly dependent on the lead-time from diagnosis [3, 4].

1.1. Prostate cancer:

1.1.1. Prostate:

The prostate is a small organ of the male reproductive and urinary system with its main function being to secrete part of the seminal fluid. Its exact size varies from one man to another, but normally the prostate of an adult is between 15 cm³ and 30 cm³ with the size of a walnut. The anterior part of the prostate is wrapped around the urethra at the base of the bladder, and the posterior part is in front of the rectum, as shown in the figure 1.2(a). It is surrounded by lymphatic and blood vessels and it sits under the seminal vesicles. The prostate can be divided into four main zones; the peripheral zone, the central zone, the transition zone and the anterior fibro-muscular zone (also known as stroma). These different zones are illustrated in figure 1.2(b).

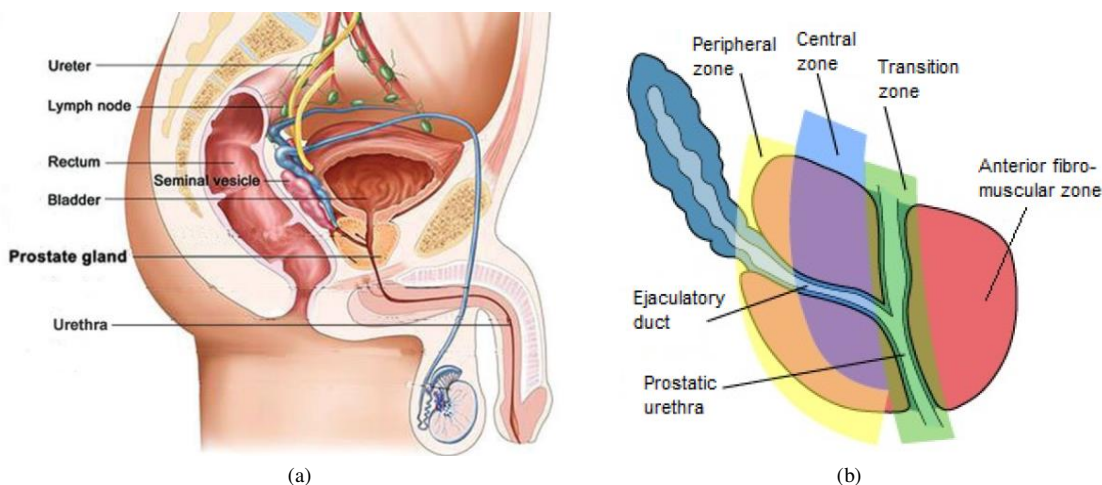


Figure 1.2. The prostate (a) anatomy, image from www.zmescience.com, (b) zones of the prostate, image from www.pathologyoutlines.com.

The central zone surrounds the ejaculatory ducts and accounts for around 2.5% of prostate cancers. The transition zone surrounds the proximal urethra and accounts for 10-20% of prostate cancers. This zone is the region of the prostate gland which grows throughout life and is

responsible for prostatic enlargement. As for the peripheral zone, the closest zone to the rectum, it is the sub-capsular portion of the posterior part of the prostate which surrounds the distal urethra. This zone accounts for up to 70% of the entire volume of the prostate, making it the origin of 70-80% of prostatic cancers [5].

1.1.2. Risk factors:

PCa starts from prostate tissues when cells lose normal control of growth and division. These cells may multiply and even spread from the prostate to other parts of the body, such as bones and lymph nodes. It often has no early symptoms, but in late stages it may cause pain in the pelvis, difficulties urinating, blood in the urine and erectile dysfunction. Unlike other types of cancer, the causes and the origins of PCa are not known. However, a few factors were proven to increase the risk of developing this cancer [6]:

- Age: almost all cases diagnosed with PCa are in men over 50 years old.
- Ethnic group: it is more common in men of African descent than in Asian descent.
- Family history: having a first-degree family member diagnosed with PCa can increase the risk of developing a cancer.
- Obesity.
- Exercise: men who exercise more often have lower risks of developing PCa.
- Diet: a diet high in calcium, red meat or milk products and low in certain vegetables may increase the risk of developing PCa.

1.1.3. Diagnosis:

Generally, PCa is suspected on the basis of Digital Rectal Examination (DRE) and Prostate-Specific Antigen (PSA) levels. However, a definitive diagnosis depends on the histopathological verification of adenocarcinoma in prostate biopsy cores or operative specimens.

Most prostate cancers are located in the peripheral zone, which is in direct contact with the rectum wall. Therefore a DRE, where the clinician palpates the prostate through the rectum wall, may detect PCa. A study in [7] showed that 18% of patients are diagnosed with PCa using DRE alone when the volume is more than 0.2 cm³.

Another tool that helps diagnosis is a blood test that measures the level of PSA. PSA is a protein produced by the epithelial cells of the prostate. It is organ- but not cancer-specific, therefore abnormal PSA levels in the blood may indicate the presence of PCa. However, if PSA level is elevated, it could be mainly, but not necessarily, due to PCa since there are also other causes of high PSA such as inflammation, infection, enlarged prostate, etc. [8]. Although the PSA blood test is more effective than DRE, it also introduces a high risk of over-diagnosis considering that sometimes men with cancer may have normal PSA levels. Thus, its use is being discussed in all major urological societies [9].

DRE and PSA tests can sometimes help detect early PCa. However, they can also miss the presence of the cancer even if it exists (false negative) or give an indication of the presence of the cancer when it is not present (false positive). Therefore, they cannot give a definite indication whether or not the PCa exists. However, when one of the two tests gives abnormal results, a biopsy is then performed in order to confirm the diagnosis.

Another diagnosis tool is the Transrectal Ultrasonography (TRUS), where an ultrasound probe is used to analyze the prostate. The presence of hypoechoic area in the peripheral zone may be a good indication of PCa. However, TRUS low quality images may not be reliable and cannot replace systematic biopsies of the prostate.

Therefore, the only definitive way to confirm PCa is the biopsy. Transrectal biopsy with TRUS guidance is the current clinical standard for PCa diagnosis. A TRUS probe is equipped with a needle guide to access the prostate and remove tissue samples for further histological examination. The guide aligns the needle trajectory with the TRUS image plane in order to correctly visualize the trajectory on the image for a more precise needle placement. The TRUS probe is therefore introduced in the patient's rectum and advanced to the base of the bladder, where the seminal vesicles can be visualized, as shown in figure 1.3. Images are then acquired while the probe is being moved back, from the prostate base to the prostate apex, out of the patient's rectum. Since 70-80% of cancers are located in the peripheral zone, an initial biopsy is performed where the needle is laterally directed to that zone.

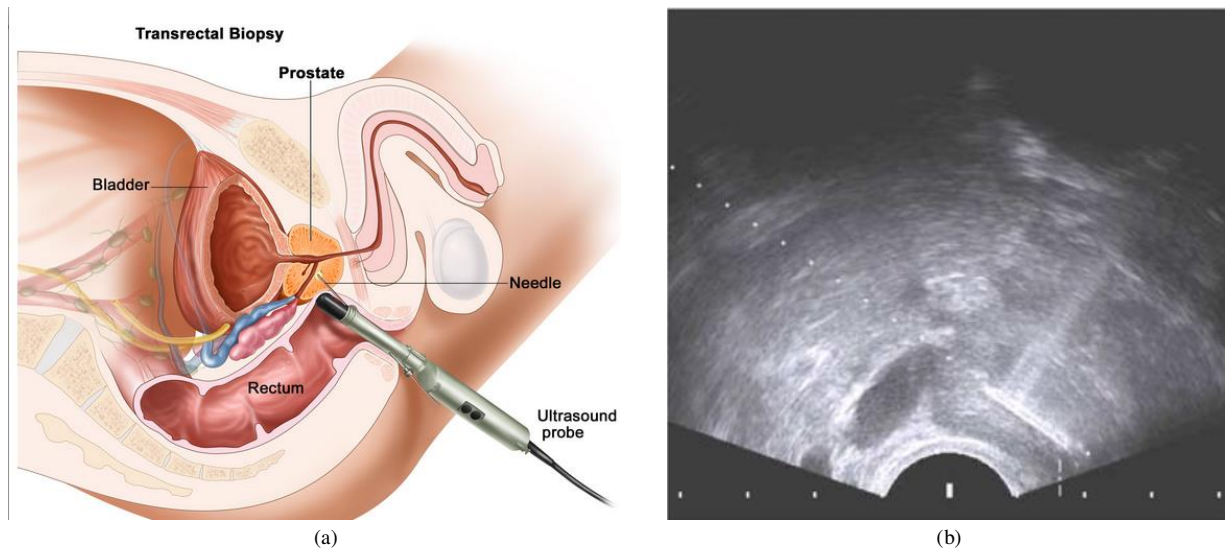


Figure 1.3. Prostate biopsy (a) transrectal approach, image from www.cancer.gov. (b) needle trajectory in TRUS, image from www.bkmed.com.

Although the transrectal approach is widely used, it may miss however 20-30% of significant cancers [10]. Therefore, some clinicians prefer to use a transperineal approach (see figure 1.4) which provides a superior detection ratio. However, this approach is complicated since the needle must be correctly positioned with respect to the targeted sample which may change during the intervention due to prostate deformations caused by the insertion of the needle and the TRUS probe pressure.

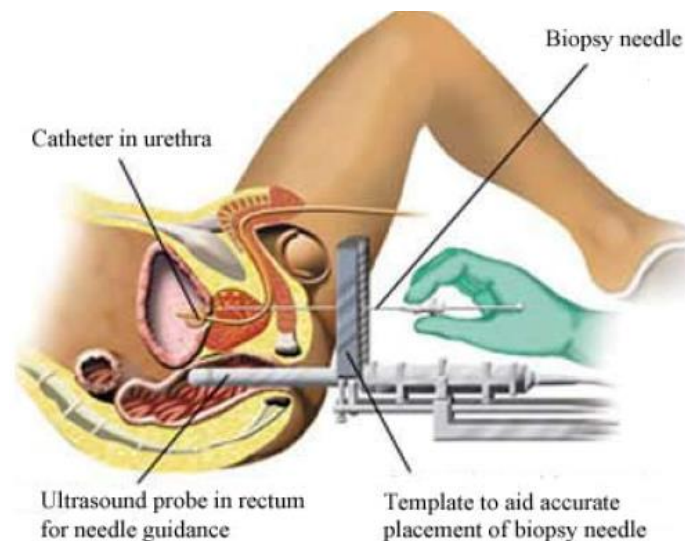


Figure 1.4. Prostate biopsy using transperineal approach, image from www.duooxfordshire.org.uk.

Improvements in Magnetic Resonance Imaging (MRI) allowed the discovery of a powerful tool for PCa detection, characterizing and staging the extent of the cancer. Multiparametric (mp) MRI, functional forms of imaging used to supplement standard anatomical T1 and T2-weighted

imaging, was extensively investigated in recent years making this technique an important diagnosis tool. Several functional sequences of choice may be considered; such as the Dynamic Contrast-Enhanced (DCE) MRI and the Diffusion-Weighted Imaging (DWI). It was proven that mpMRI, with its superior performance characteristics of the detection and localization of PCa, can achieve a positive predictive value of up to 98% for PCa, whereas the detection rate using T2-weighted MRI alone was of 68% [11]. MpMRI provides detailed anatomical and functional information that cannot be obtained from the TRUS. Therefore, in the future paradigm of PCa detection, mpMRI may be performed after a suspicious PSA to confirm whether the cancer is present or not. In this paradigm, unnecessary biopsies may be avoided in the case of false positive diagnosis. On the other hand, if the mpMRI confirmed the presence of PCa, an accurate targeted biopsy can be performed by combining this imaging modality with the TRUS.

1.1.4. **Treatment:**

Several types of treatments may be considered, depending on the stage and location of the cancer, the benefits and risks associated with each treatment technique, and according to the patient's condition. These techniques include:

1- Active surveillance:

Active surveillance is a way of monitoring PCa for signs of tumor progression. A DRE and PSA blood test are performed periodically (around 6 months) along with a repeat biopsy (every year). If these tests indicated that the cancer is growing or spreading outside the prostate, a treatment might be warranted. Active surveillance can be considered as an option for localized PCa in cases where the patient decides not to undergo any kind of treatment immediately or in cases where life expectancy is limited. It is usually considered based on several factors; age, medical condition, PSA stage, amount of cancer in the biopsy, etc...

2- Prostatectomy:

Prostatectomy is a surgical treatment that may be considered when the cancer is at early-stage or is localized in the prostate only [12]. It consists in removing part (for benign conditions) or the whole volume (for malignant cancer) of the prostate along with the seminal vesicles.

This surgical removal is performed in different ways; an open surgery (an incision through the abdomen allows removing the prostate from behind the pubic bone), laparoscopically (using a robot), through the urethra or through the perineum. After the surgery, and in order to verify that the tumor has been removed, a biopsy is performed. According to the result of the biopsy, a complimentary treatment may be prescribed using another kind of treatment; such as radiation therapy or hormone therapy (see next paragraphs). Radical prostatectomy is linked with several side effects including urinary incontinence and erectile dysfunction [13]. Moreover, prostatectomy leads to infertility [14]. On the other hand, urination is less painful in patients undergoing prostatectomy when compared to other radiation therapy techniques [15].

3- External Beam Radiation Therapy (EBRT):

EBRT is a type of radiation therapy that consists in destroying the cancerous cells by irradiating the prostate with an external source of ionizing radiation. X-rays are produced by a linear accelerator (linac) (see figure 1.5). Linac transmits photon beams in different angles in order to irradiate the whole volume of the structure of interest. These angles are determined using radiological images where the tumor's location is mapped out at first, and then X-ray beams are delivered to that location. The treatment planning is highly dependent on the placement of the patient. Linac rotates around a point, called isocenter, which is situated at 100 cm from the source of the radiation and should be placed in the center of the target volume. In order to correctly place the isocenter, the treatment planning system determines how the patient should be placed on the table. The radiotherapist prescribes the dose that should be applied on the tumor. Afterwards, and using the treatment planning system, the dose distribution is calculated using Computed Tomography (CT) images, as shown in figure 1.6.

For PCa, EBRT is usually performed in the cases of a localized cancer as well as when the tumor is locally advanced. It can also be applied after prostatectomy if a biopsy indicated that the tumor has not been removed during the surgery. The main drawback of EBRT is that the X-ray beams, when pointed at the organ of interest, are delivered to that organ as well as the areas around it. Side effects are usually limited to the part of the patient's body that received the radiation. They include however urinary incontinence and erectile dysfunction.



Figure 1.5. Truebeam™, a linear accelerator used for EBRT, image from www.varian.com.

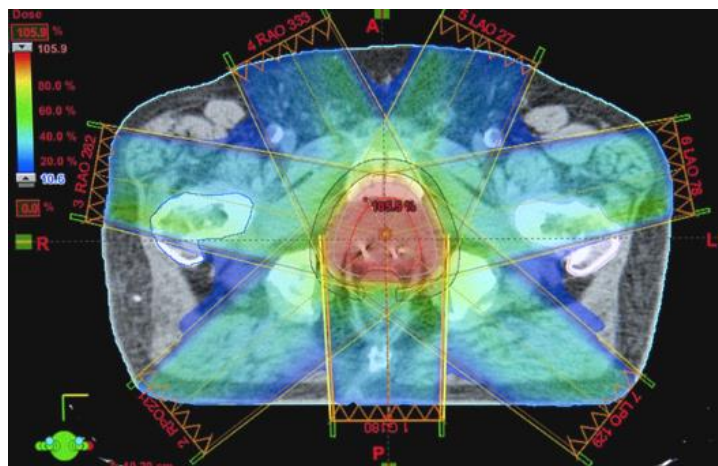


Figure 1.6. Prostate radiotherapy using 7 beams, image from <http://chestercountyhospital.org>.

4- Brachytherapy:

Brachytherapy, also known as internal radiotherapy, is a type of radiation therapy where the irradiation is delivered by inserting radioactive sources inside the structure of interest, temporarily or permanently. In the case of PCa, radioactive sources are inserted via needles that go through the perineum. Brachytherapy has the advantage of delivering a high dose of irradiation to the prostate while sparing the surrounding healthy tissues; namely the rectum and bladder. According to [2, 15], brachytherapy has several advantages and better quality-of-life when compared to other treatment techniques:

- It is minimally invasive
- It requires a short hospital stay
- Patient exposure to ionizing radiation is minimized, compared to EBRT.
- Lower cost.

In the United States, 60000 patients underwent brachytherapy in 2006, which represents 35% of the treatment techniques. In other countries such as Germany, Netherlands, England and Spain, brachytherapy represents between 5 and 12 % only. In France, despite the very encouraging results of this treatment, the ratio is still as low as 3%. This is due to the late and insufficient valorization that does not reflect the actual costs of the medical work and the necessary environment. Major urological French and European societies consider brachytherapy as a standard treatment for PCa, they also encourage exploiting this technique since it has several advantages when compared to other techniques [2]. The number of treatments with this technique is however increasing from one year to another; from 1636 in 2007 it has reached 4000 treatments in 2015.

Unlike other techniques, brachytherapy has been practiced for almost two decades in France. The feedback from the research and practice that has been done on brachytherapy gave very good long-term results and a better quality-of-life for patients undergoing this treatment when compared to other treatment techniques; making brachytherapy the current technique of choice when treating early-stage prostate cancers. In addition, brachytherapy also allows focal treatments, which are characterized by having minimum side effects.

5- Hormone therapy:

Hormone therapy, also called Androgen Deprivation Therapy (ADT), consists in reducing the levels of male hormones (androgens) which stimulate prostate cancer cells to grow. Testosterone is the main androgen responsible for prostate cancer cells growth. Therefore, ADT involves blocking the testosterone from being released into the prostate. This may make the prostate shrink or grow more slowly but generally, when applied alone, it does not cure prostate cancer. This kind of treatment is delivered mainly to older men, men diagnosed with a cancer where lymph nodes are involved or a cancer accompanied by extensive metastases.

Although most of prostate cells respond to the removal of this hormone, some cells grow independently of androgens, and therefore are not affected by this kind of therapy. Side effects of hormone therapy include erectile dysfunction, loss of bone density, low red blood cell counts, loss of muscle mass and physical strength.

6- Chemotherapy:

Chemotherapy is a type of therapy that makes use of chemicals, or anti-cancer drugs, to destroy the cancerous cells. It is generally used in certain cases where the cancer is hormone-resistant. The efficacy of chemotherapy depends on the type and stage of the cancer. It is usually used to relieve symptoms associated with metastatic disease. However, this treatment is sometimes completely ineffective in cases such as brain tumors. The main inconvenience of this kind of treatment is that it has, as any other drug, several side effects on the body including hair loss, nausea, vomiting, diarrhea, fatigue (low red blood cell counts) and increased chance of infections (low white blood cell counts).

7- High-Intensity Focused Ultrasound (HIFU):

HIFU can also be considered when the radiation treatments fail in the case of a low risk cancer or a localized PCa. It consists in destroying cancerous cells by heating the prostate. TRUS is used to transmit ultrasonic beams, in duration of five seconds, to a target localized zones of the prostate. HIFU has the advantage of being radiation-free and therefore no irradiation-related side effects are caused by such a treatment. It is also non-invasive, so no incisions are made like in the case of a prostatectomy. HIFU is performed in only 180 centers around the world, 38 of which are in France. The French Association of Urology (L'association française d'urology) recommends HIFU when the patient is over 70 years old and when the prostate volume is less than 40 cm³ [16]. According to [16], patients who underwent HIFU have less urinary incontinence when compared to other treatments. However, some medical associations do not recommend HIFU because they think that more research should be done including clinical trials evaluating the quality-of-life and the long-term survival of patients undergoing this kind of treatment [17].

8- Cryotherapy:

Similarly to HIFU, cryotherapy is another focal treatment that can also be considered when the radiation treatments fail in the case of a low risk or localized PCa. This treatment consists in decreasing the growth and reproduction of cancerous cells by freezing the prostate tissues. It is used to treat localized cancers while sparing other prostate tissues, but also low volume cancers. Its main objective is to provide adequate cancer control while minimizing the side effects [18]. However, this technique is still under evaluation for the treatment of PCa.

9- Other focal therapies:

While cryotherapy and HIFU are currently the two modalities with the most long-standing experience in focal therapy, other Focal Laser Ablation (FLA) techniques are currently under investigation; such as Photodynamic Therapy (PDT) and Laser Interstitial Thermo Therapy (LTIT). FLA is an intermediate option between active surveillance and radical prostatectomy for small and low risk PCa. In such laser-based procedures, laser energy is used to ablate only the index lesion while minimizing the damage to the surrounding structures [19]. Light energy is delivered to target cancerous cells via a fiber-optic catheter. Subsequently, computer-guided laser ablation is performed under real-time MRI guidance. FLA techniques have fewer side effects than other treatments, and they are minimally invasive procedures [20]. However, these techniques are still under evaluation and need more clinical trials to study their safety and effectiveness.

In this work, we will focus on brachytherapy considering that it has been practiced and investigated since the 90's with good long-term results showing several advantages; better quality-of-life and fewer side effects when compared to other treatment techniques [2, 15].

Hereafter, the clinical context of brachytherapy is explained in details. The problems and the challenges in this kind of treatment are highlighted, leading to the proposed approach that overcomes these problems.

1.2. **Brachytherapy:**

Brachytherapy is an intra-operative radiotherapy technique for the irradiation of tumors by placing radioactive sources within the structures of interest. Considering its delivery mechanisms, it can be divided into two types; High Dose Rate (HDR) and Low Dose Rate (LDR). HDR brachytherapy consists in placing small catheters in the organ of interest, and then a single high activity radioactive source is inserted temporarily at different positions within the organ. Catheters are then pulled out easily and no radioactive material is left in the organ.

LDR brachytherapy involves placing multiple low activity radioactive sources permanently inside the organ of interest. These radioactive sources give off their radiation after some time, and then remain in the organ permanently.

Several kinds of radioactive sources may be used in brachytherapy [21]; Cesium-131 (half-life 9.7 days, average photon energy 30.4 keV), Palladium-103 (half-life 17 days, average photon energy 20.8 keV) and more often the Iodine-125 (half-life 59.4 days, average photon energy 28.5 keV), illustrated in figure 1.7.



Figure 1.7. Radioactive sources used in brachytherapy, image from <https://en.wikipedia.org>.

The choice and the number of radioactive sources to be inserted are based on both the volume of the organ to be treated and the prescribed dose. In the case of PCa, Iodine-125 and Palladium-103 are used in brachytherapy because of their low energy which allows a localized irradiation. A comparison between the radiobiological results achieved using different kinds of sources was done in [22]. This study demonstrated that Palladium should be used in cases where tumors are rapidly growing, while Iodine is more adapted to cases where the cancer growth is slow; such as prostate cancer.

Approximately, between 70 and 100 radioactive sources are inserted into the prostate where they irradiate this organ over several weeks or months and then remain inside the prostate permanently as they become gradually inactive. Since these radioactive sources are inserted into, or very close to, the tumor, they can deliver a high localized dose of radiation to the tumor while sparing the surrounding healthy tissues.

1.2.1. Clinical context:

Brachytherapy is commonly used for cervical, prostate, breast, and skin cancer. In the case of early-stage prostate cancer, patients undergoing LDR brachytherapy have generally better urinary continence and sexual functions compared to other radiotherapy techniques [23]. Hereafter, we will explain the clinical context of LDR prostate brachytherapy, which may apply to HDR as well.

In LDR prostate brachytherapy, the patient lies in a lithotomy (gynecological) position under general anesthesia. The surgeon utilizes TRUS in order to localize the wall of the rectum as well as the prostate (figure 1.8(a)). A urinary catheter is also inserted in the urethra of the patient in order to visualize it. Once the prostate and the other organs at risk (urethra and rectum) are localized, the surgeon delineates these structures manually. Afterwards, the treatment planning system calculates the dose distribution. Empty needles are then inserted in the prostate through a grid, also called template, fixed on the TRUS in front of the perineum of the patient, as shown in figure 1.8(b). This insertion is done with the help of TRUS images that provide the surgeon with a real-time guidance to help him correctly place the needles in the prostate. Finally, the radioactive sources are inserted manually, one by one, while withdrawing the needles slowly from the prostate (figure 1.8(a)).

Several problems may arise when following this clinical approach used nowadays. First of all, the TRUS image is not well adapted to visualizing the prostate or its interfaces with the surrounding organs due to its low soft tissue contrast [30]. Therefore, the delineation process is complicated and time consuming. Moreover, it is subject to intra- and inter-observer variability inaccuracies depending on the surgeon's experience.

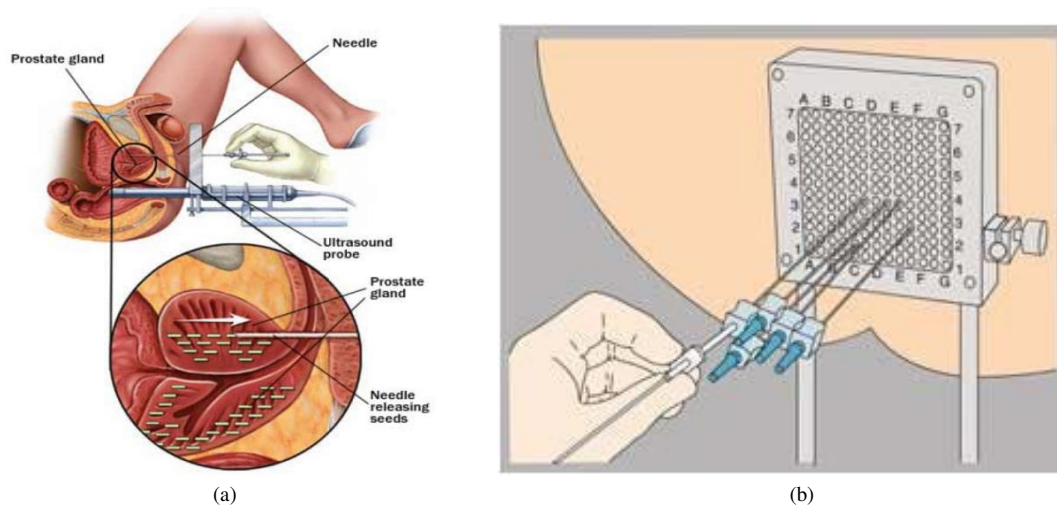


Figure 1.8. Needle insertion in brachytherapy using (a) TRUS, image from www.mayoclinic.com. (b) the template, image from https://en.wikipedia.org/wiki/Prostate_brachytherapy.

A second drawback is the accuracy of the dosimetry estimation. The dose distribution is routinely calculated based on the American Association of Physicists in Medicine (AAPM) task group TG-43 formalism. This formalism considers the patient as a homogenous water medium, which is associated with several approximations such as tissue homogeneity and the absence of inter-seed attenuation [24]. This hypothesis is not accurate and may lead to non-optimal dose estimations [25]. Finally, the prostate suffers from deformations during this intervention, caused by the insertion of needles and the pressure of the TRUS, these deformations need to be taken into account to have a more precise treatment.

To overcome all these challenges, different medical imaging modalities can be used. Medical images are being a vital component of clinical applications; not only for the purpose of diagnosis but also in treatment planning, delivery and evaluation after the intervention. Radiotherapy, which is a treatment involving the use of ionizing radiation on tumors, is one of the applications whose evolution has been clearly linked to medical imaging [26]. The use of imaging systems during the radiation therapy, called Image-Guided Radiation Therapy (IGRT), has the potential of improving the precision and the overall accuracy of the planning as well as the delivery of the treatment [27].

1.3. Objectives of the thesis: Image-guided brachytherapy:

The objective of this work is to propose a multimodal approach that can improve the overall accuracy of prostate brachytherapy treatment planning and delivery. This approach aims to precisely plan the positions of the radioactive sources as well as improve the visualization during the intervention in order to correctly place these sources in their pre-planned positions. The proposed approach needs to be automatic, user-friendly and, above all, accurate in order to facilitate its integration in a clinical workflow.

In brachytherapy, the dose distribution is currently calculated using the TG-43 formalism. The TRUS is used to visualize the dose distribution and to help the clinician place the radioactive sources in their pre-planned positions. Figure 1.9 illustrates the clinical workflow followed nowadays in prostate brachytherapy. As previously stated in section 1.2.1., once the dose distribution is calculated, using the treatment planning system, the surgeon starts inserting the sources, via needles that enter through the perineum, under the guidance of TRUS.

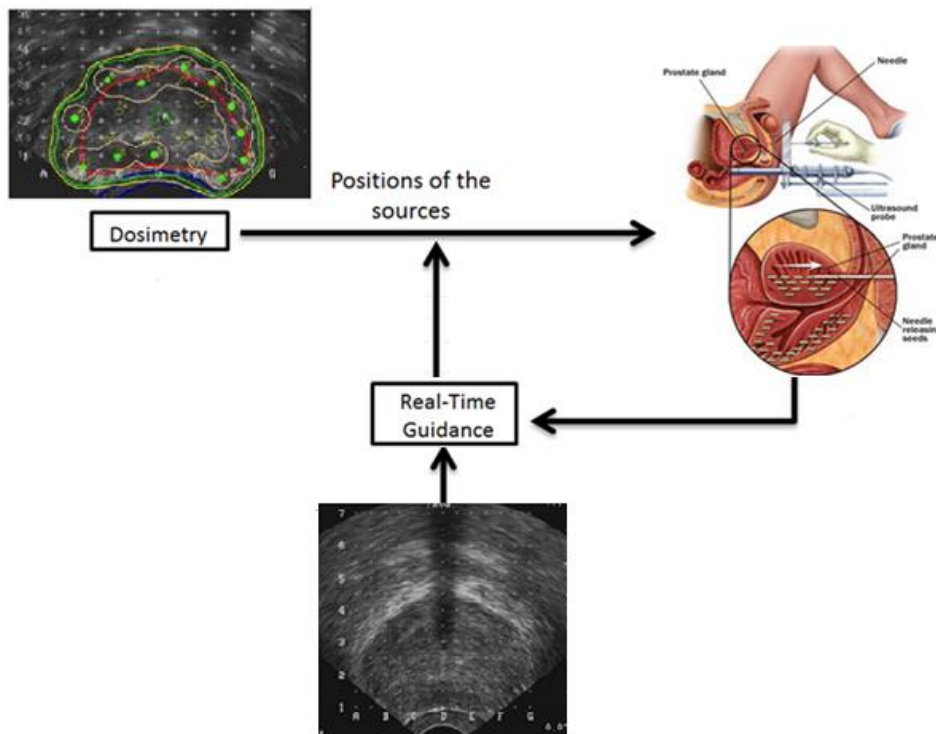


Figure 1.9. Clinical workflow of prostate brachytherapy.

Multimodal imaging could potentially improve the overall accuracy of the treatment. First of all, and for a more accurate dose estimation, CT images can be used in brachytherapy treatment planning in order to calculate a Personalized Dose Distribution (PDD) based on tissues electron

density values. A PDD that considers soft tissue heterogeneities, based for example on the use of Monte Carlo simulations, can significantly reduce dosimetry errors [28].

Therefore, in this case, optimal positions of radioactive sources would be expressed in CT reference while the insertion is done under TRUS guidance. In order to make use of the information coming from both modalities, the positions of the sources must be transferred between CT and Ultrasound (US). In other words, the information must be geometrically aligned to a common coordinate system, a process referred to as image registration. However, a robust and direct registration between these two modalities is hardly possible since they both provide low soft tissue contrast and therefore are not well suited for the visualization of the prostate (figure 1.10(a), 1.10(b)).

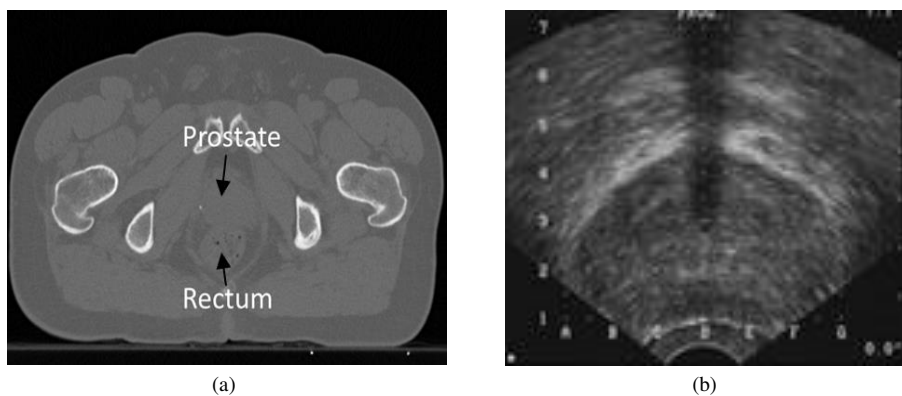


Figure 1.10. (a) CT and (b) TRUS images of the prostate.

Moreover, CT is known to often overestimate the size of the prostate when compared to other modalities, such as the MRI [29]. US, on the other hand, has a tendency to underestimate the extent of lesions [30]. MRI, however, can be an advantage in the pelvic region compared to CT because of its superior soft tissue contrast (figure 1.11) [31].

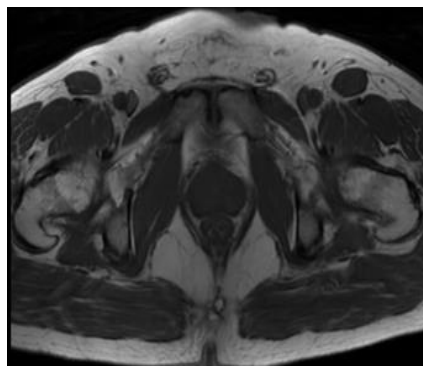


Figure 1.11. MRI of the prostate.

Therefore, the use of MRI could potentially improve brachytherapy planning but also treatment guidance by providing a better visualization with respect to the tumor's location as well as the organs at risk. Moreover, MRI is generally acquired for the diagnostic before the treatment, so this proposed approach does not require an acquisition of a new modality. Nevertheless, CT is essential for dose calculations since, unlike MRI, it is directly related to electron density.

In order to explore the information provided by all modalities (US, MRI and CT), it is essential that these 3D image datasets are accurately spatially aligned. The workflow of the proposed approach for image-guided brachytherapy is illustrated in figure 1.12. A first registration between MR/CT images is required in the pre-operative phase for the treatment planning. A second registration is required during the intervention between MR/US images for the treatment delivery. These two registration methods have to be combined so to that an integrated solution can be proposed for image-guided brachytherapy procedures.

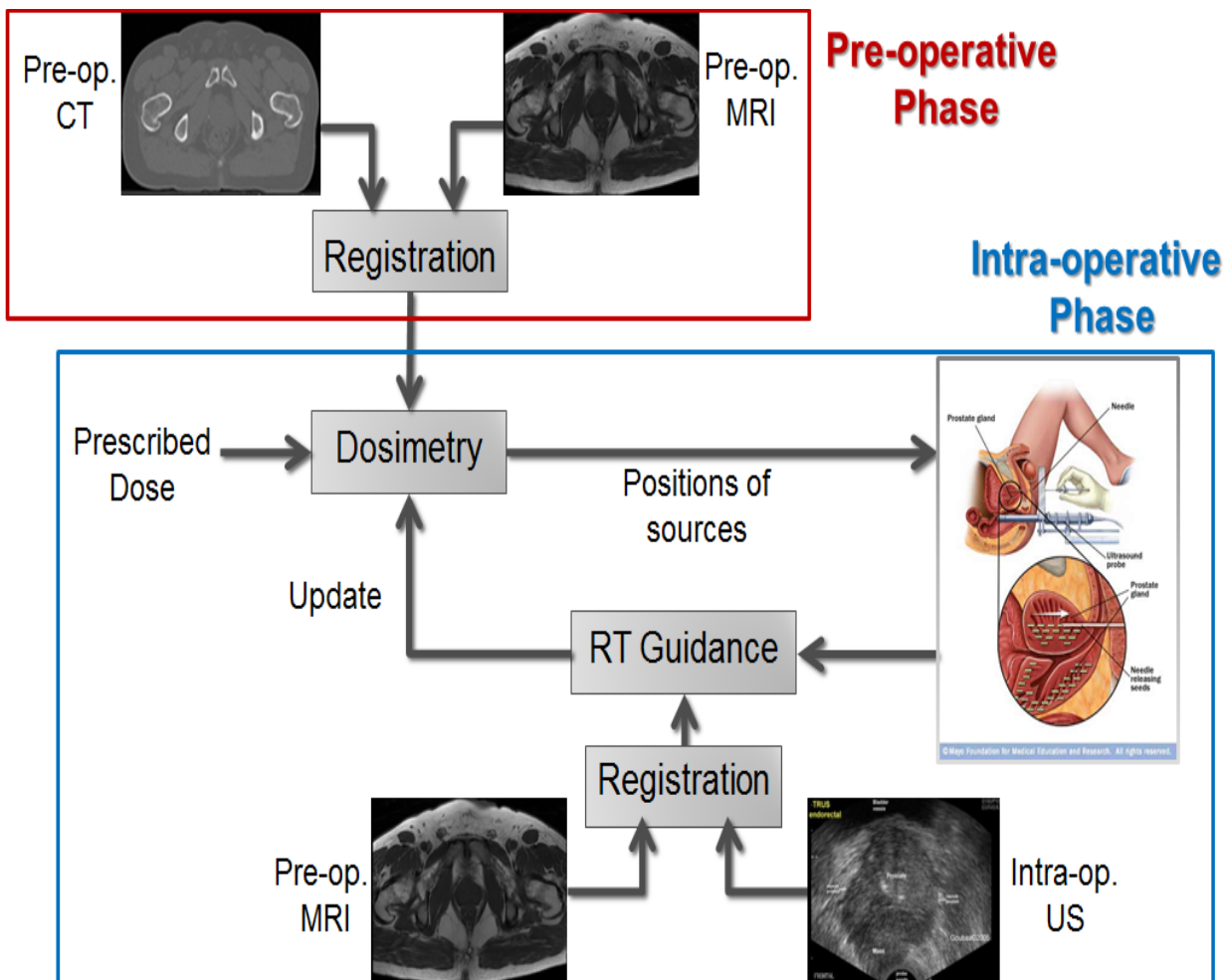


Figure 1.12. The workflow of the proposed approach.

Concerning the pre-operative phase, MR and CT images cannot be acquired simultaneously, and in most cases are acquired within a few days or weeks interval. In addition, the form of the imaging couch where the patient lies for the acquisition of each modality may be different. Therefore, there would be some differences not only in prostate location but also size as a result of temporal evolution deformations, different bladder and rectum fillings as well as patient motion [32]. As such, a non-rigid registration is necessary in order to compensate for prostate deformations. Similarly, for the intra-operative phase, the MR is acquired before the intervention while the US image is acquired in real-time during the intervention. Moreover, the prostate will suffer from extra substantial deformations caused by the insertion of the needles as well as the pressure of the TRUS probe on the rectum wall, which is in direct contact with the prostate, as illustrated in figure 1.13. As such, a non-rigid registration is also necessary for the intra-operative registration.

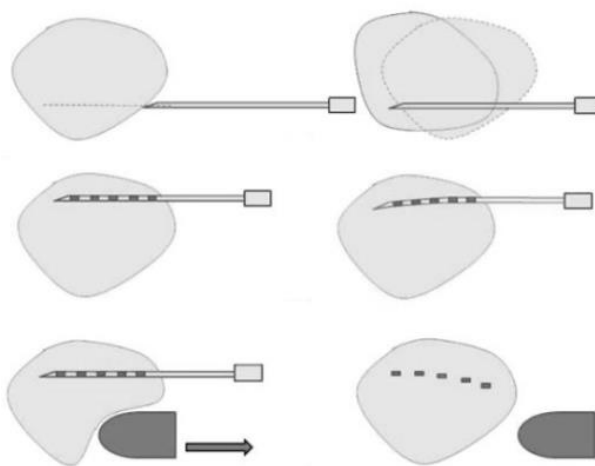


Figure 1.13. Prostate deformations caused by needle insertion and TRUS probe pressure, image from [33].

The development of such a registration is a challenging problem given the very different nature of these three modalities (CT, MRI and US). The overall accuracy of this registration has a great impact upon treatment planning and delivery. In fact, the proposed registration methodology should detect prostate deformations in order to provide the exact position of the tumor; allowing the delivery of a higher dose to the tumor while reducing the exposure of the surrounding healthy tissues to radiation. Therefore, an efficient and accurate registration is required.

1.4. Conclusion:

The objective of this work is the development of a new approach that contributes to a more accurate prostate brachytherapy treatment planning and delivery. A variety of image modalities are being used in image-guided prostate brachytherapy; such as MRI, CT and US. In the pre-operative phase, and in order to improve the accuracy of the treatment planning, a fully automatic registration between MR and CT images will be proposed. This registration allows a precise planning of the radioactive sources and helps improving the visualization of the dose distribution as well. Similarly, in the intra-operative phase, a fully automatic US/MRI registration will be proposed in order to help the surgeon correctly place the radioactive sources in their pre-planned positions by providing a better visualization during the intervention. The second chapter is dedicated to the MRI/CT registration while the US/MRI registration is presented in the third chapter. The fourth chapter will be focused on the evaluation of these two registration methods. Finally, we will conclude this work by discussing the results of these two registrations. A few perspectives and future work are presented as well.

References:

- [1] – <http://www.invs.sante.fr/> Institut de Veille Sanitaire.
- [2] – Rapport d’expertise sur la curiethérapie, plan cancer 2009-2013. Société Française de Radiothérapie Oncologique (SFRO).
- [3] Andriole GL et al. (2009). “Mortality results from a randomized prostate-cancer screening trial”. *The new England Journal of Medicine*. **360(13)**: 1310-9.
- [4] De Koning HJ et al. (2002). “Large-scale randomized prostate cancer screening trials: program performances in the European Randomized Screening for Prostate Cancer trial and the Prostate, Lung, Colorectal and Ovary cancer trial”. *International Journal of Cancer*. **97(2)**: 237-44.
- [5] – <http://www.prostate-cancer.com/> Prostate Cancer Treatment Guide.
- [6] – <http://www.cancer.org/> Prostate cancer risk factors.
- [7] Mottet N et al. (2015). “Guidelines on prostate cancer”. *European Association of Urology*.
- [8] Schroder FH, Carter HB, Wolters T, van den Bergh RC, Gosselaar C, Bangma CH, and Roobol MJ (2008). “Early detection of prostate cancer in 2007: part 1: PSA and PSA kinetics”. *European Urology*. **53(3)**: 468-77.
- [9] American Cancer Society (2016). “Prostate Cancer Prevention and Early Detection”.
- [10] Taira AV, Merrick GS, Galbreath RW, Andreini H, Taubenslag W, Curtis R, Butler WM, Adamovich E, and Wallner KE (2010). “Performance of transperineal template-guided mapping biopsy in detecting prostate cancer in the initial and repeat biopsy setting”. *Prostate Cancer and Prostatic Diseases*. **13(1)**: 71-7.
- [11] Turkbey B et al. (2011). “Multiparametric 3T prostate magnetic resonance imaging to detect cancer: Histopathological correlation using prostatectomy specimens processed in customized magnetic resonance imaging molds”. *Journal of Urology*. **186(5)**: 1818-24.
- [12] Bill-Alexon A et al. (2011). “Radical Prostatectomy versus watchful waiting in early prostate cancer”. *The New England Journal of Medicine*.
- [13] Chen RC, Clark JA, and Talcott JA (2009). “Individualizing quality-of-life outcomes reporting: how localized prostate cancer treatments affect patients with different levels of baseline urinary, bowel, and sexual function”. *Journal of Clinical Oncology*. **27(24)**: 3916-22.
- [14] Tran S, Boissier R, Perrin J, Karsenty G, and Lechevallier E (2015). “Review of the different treatments and management for prostate cancer and fertility”. *Urology*. **86(5)**: 936-41.
- [15] Ferrer M et al. (2008). “Health-related quality of life 2 years after treatment with radical prostatectomy, prostate brachytherapy, or external beam radiotherapy in patients with clinically localized prostate cancer”. *International Journal of Radiation Oncology Biology Physics*. **72(2)**: 421-32.

- [16] Rebillard X, Soulié M, Chartier-Kastler E, Davin JL, Mignard JP, Moreau JL, and Coulange C (2008). “High-intensity focused ultrasound in prostate cancer; a systematic literature review of the French Association of Urology”. *BJU International*. **101(10)**: 1205-13.
- [17] Warmuth M, Johansson T, and Mad P (2010). “Systematic review of the efficacy and safety of high-intensity focused ultrasound for the primary and salvage treatment of prostate cancer”. *European Urology*. **58(6)**: 803-5.
- [18] Shah TT, Ahmed H, Kanthabalan, Lau B, Ghei M, Maraj B, and Arya M (2014). “Focal cryotherapy of localized prostate cancer: a systematic review of the literature”. *Expert Review of Anticancer Therapy*. **14(11)**: 1337-47.
- [19] Marshall S and Taneja S (2015). “Focal therapy for prostate cancer: The current status”. *Prostate International*. **3**: 35-41.
- [20] Wenger H, Yousuf A, Oto A, and Eggener S (2014). “Laser Ablation as Focal Therapy for Prostate Cancer”. *Current Opinion in Urology*. **24(3)**: 236-40.
- [21] Rijnders A (2009). “Radiotherapy and Brachytherapy. Photon Sources for Brachytherapy”. *NATO Science for Peace and Security Series B: Physics and Biophysics*. 185-93.
- [22] Ling CC (1992). “Permanent implants using Au-198, Pd-103 and I-125: radiobiological consideration based on the linear quadratic model”. *International Journal of Radiation Oncology Biology Physics*. **23(1)**: 81-7.
- [23] Frank SJ, Pisters LL, Davis J, Lee AK, Bassett R, and Kuban DA (2007). “An assessment of quality of life following radical prostatectomy, high dose external beam radiation therapy and brachytherapy iodine implantation as monotherapies for localized prostate cancer”. *Journal of Urology*. **177(6)**: 2151-6.
- [24] Carrier JF, Beaulieu L, Therriault-Proulx F, and Roy R (2006). “Impact of interseed attenuation and tissue composition for permanent prostate implants”. *Medical Physics*. **33(3)**: 595-604.
- [25] Rivard MJ, Venselaar JL, and Beaulieu L (2009). “The evolution of brachytherapy treatment planning”. *Medical Physics*. **36(6)**: 2136-53.
- [26] Kelloff GJ, Choyke P, and Coffey DS (2009). “Challenges in clinical prostate cancer: role of imaging”. *American Journal of Roentgenology*. **192(6)**: 1455-70.
- [27] Gupta T and Narayan A (2012). “Image-guided radiation therapy: Physician’s perspectives”. *Journal of Medical Physics*. **37(4)**: 174-82.
- [28] Lemaréchal Y, Bert J, Falconnet C, Després P, Valeri A, Schick U, Pradier O, Garcia MP, Bousson N, and Visvikis D (2015). “GGEMS-Brachy: GPU GEant4-based Monte Carlo simulation for brachytherapy applications”. *Physics in Medicine and Biology*. **60(13)**: 4987-5006.
- [29] Sannazzari GL, Ragona R, Ruo Redda MG, Giglioli FR, Isolato G, and Guarneri A (2002). “CT-MRI image fusion for delineation of volumes in three-dimensional conformal radiation therapy in the treatment of localized prostate cancer”. *The British Journal of Radiology*. **75(895)**: 603-7.

- [30] Huch Boni RA, Boner JA, Debatin JF, Trinkler F, Knonagel H, Von Hochstetter A, Helfenstein U, and Krestin GP (1995). "Optimization of Prostate Carcinoma Staging: Comparison of Imaging and Clinical Methods". *Clinical Radiology*. **50(9)**: 593-600.
- [31] Khoo VS, Padhani AR, Tanner SF, Finnigan DJ, Leach MO, and Dearnaley DP (1999). "Comparison of MRI with CT for the radiotherapy planning of prostate cancer: a feasibility study". *The British Journal of Radiology*. **72(858)**: 590-7.
- [32] Herk MV, Bruce A, Kroes AP, Shouman T, Touw A, and Lebesque JV (1995). "Quantification of organ motion during conformal radiotherapy of the prostate by three dimensional image registration". *International Journal of Oncology Biology Physics*. **33(5)**: 1311-20.
- [33] Hungr N, Baumann M, Long JA, and Troccaz J (2012). "A 3D Ultrasound Robotic Prostate Brachytherapy System with Prostate Motion Tracking". *IEEE Transactions on Robotics*. **28(6)**: 1382-97.

Pre-operative MRI/CT Registration

In this chapter, a registration methodology between pre-operative MR and CT images for prostate brachytherapy is presented. This registration aims to improve the accuracy of the treatment planning. The proposed approach is automatic in order to save manual labor and therefore facilitate its integration in a clinical workflow. The registration should compensate for prostate deformations due to the temporal evolution, different fillings of the bladder and rectum and patient motion between the two acquisitions. An overview on image registration is at first presented, where the main components of registration are explained. Then, a state of the art of techniques dedicated to prostate brachytherapy planning is presented. Subsequently, the proposed approach is explained in details.

2.1. Principles of image registration:

A variety of imaging modalities are being used in prostate brachytherapy; such as CT, MRI and US. Images obtained from different modalities need to be combined and/or compared to one another in order to make use of the information coming from each one of them. These images can be acquired using different modalities, from different subjects or at different times, leading to misalignment between them. Image registration is the process of determining the spatial transformation that maps points from one image (called floating image) to points from another (called fixed image), as illustrated in figure 2.1.

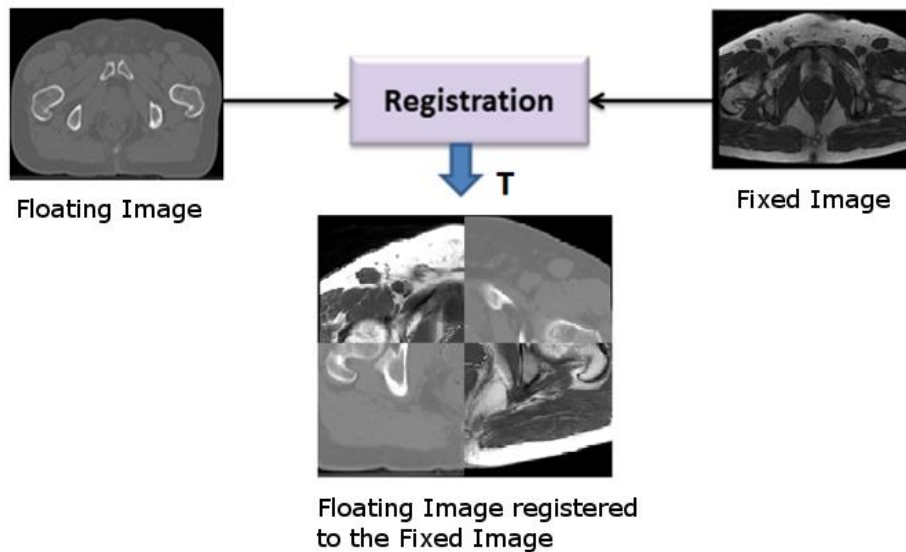


Figure 2.1. Image registration.

It is a crucial step in any medical application in order to combine or gather information from the combination of multiple data sources. A recent survey of medical image registration can be found in [1].

2.1.1. Classification of registration methods:

Registration methods can be classified in many ways. A scheme that provides a categorization has been suggested in [1, 3]. This categorization is illustrated in figure 2.2.

Dimensionality:

Image dimensionality refers to the number of spatial dimensions of the images involved. In most medical applications, images are *three-dimensional* (CT, MRI), but sometimes *two-dimensional* (radiographs) or even *four-dimensional* (time-resolved volumes).

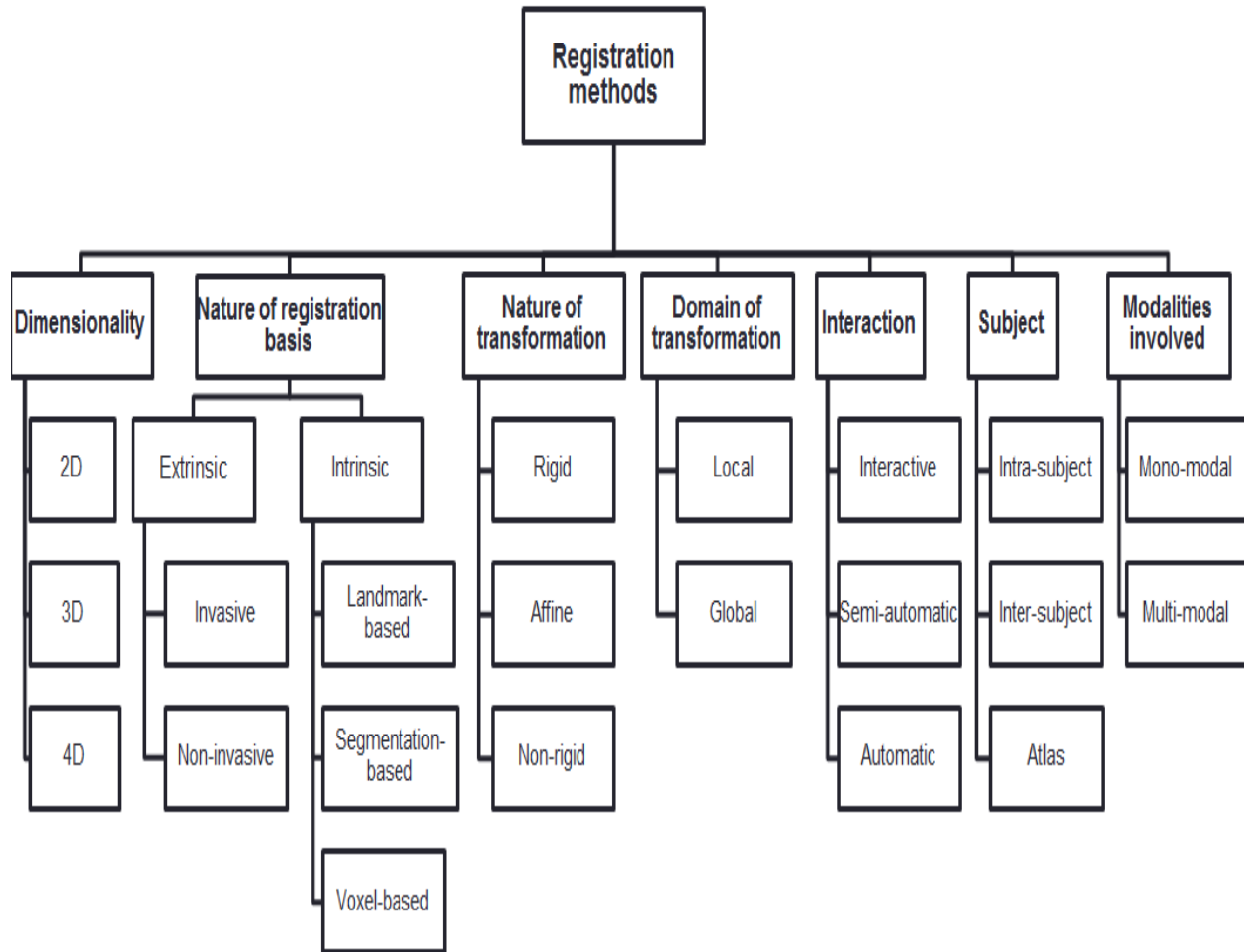


Figure 2.2. Classification of registration methods, image from [1].

Registration basis:

Registration methods can be divided into two main groups considering the nature of registration basis; *extrinsic* and *intrinsic* registration methods.

Extrinsic methods are based on foreign objects introduced into the image space such as fiducial markers (inside or on the skin of the patient) and stereotactic frame fixed on the patient's skull for example. These objects are usually attached to the patient in a way that makes them well visualized and detectable in both imaging modalities being registered. Since extrinsic methods do not include any patient related image information, they are usually restricted to rigid transformations only.

Intrinsic methods rely on information acquired from the patient image only. Registration can be based on a set of anatomical or geometrical landmarks (called landmark- or *point-based* registration). It can also be based on the segmented binary structures (called segmentation- or *surface-based* registration) which can be based on a rigid (surfaces or lines) or deformable (surfaces or curves) model. In other cases, registration can be based on measurements computed directly from pixels intensities (voxel- or *intensity-based* registration).

The main disadvantage in point- and surface-based methods is that user interaction is usually required for either the identification of landmarks or the delineation of the structure of interest. This step can be time consuming and subject to intra- and inter-observer variability inaccuracies depending on the experience of the user. On the other hand, intensity-based registration methods can be performed directly from image grey values without the need for landmark identification or segmentation. Consequently, these methods are relatively easy to automate. The major drawback of intensity-based registration methods is their computational cost, especially when applying this approach to large images. A solution to this problem might be to constrain the registration to solely regions of interest (ROIs) and not the whole image. However, when applying intensity-based registration methods on different modalities, a simple similarity measure, such as the sum of squared intensity differences, is no longer sufficient and a more complex criterion needs to be considered, such as the mutual information. This is mainly due to the difference in nature between the modalities, which tend to represent structures in different ways and with different intensities.

Transformation:

The geometrical transformation that aligns the two images is called *rigid* when only translations and rotations are allowed, resulting in 6 parameters or degrees of freedom (DoF) in 3D. Rigid registration can be extended to *affine*, i.e. rigid + shearing + scale (12 DoF in 3D) in order to map parallel lines from one image into another. Finally, in the presence of deformations, the transformation maps lines onto curves and it is called elastic or *non-rigid*, also known as deformable. Non-rigid registration is mostly used to detect soft tissues deformations introduced between two images. Another use is when the two images are from two different patients. Deformable transformations include finite element methods [4], B-Splines [5], thin-plate Splines

[6] and optical flow approaches (Demon algorithm) [7]. A good review of non-rigid registration methods can be found in [8].

Domain of the transformation:

A transformation is called *global* when it is applied to the entire image, and *local* if it is constrained to only regions of interest in the image.

Interaction:

Considering the user interaction, the registration method can be *automatic*, *semi-automatic* or *interactive* (or manual). In semi-automatic methods, the user interaction is needed to either initialize (manual segmentation or identification of landmarks) or steer (reject or accept the results of the registration) the method. Interactive registration methods, on the other hand, are performed manually by the user himself.

Subject:

If all images are from the same patient, then the registration is called *intra-subject*. On the other hand, if the registration is between two images from two different patients, then it is called *inter-subject*. Another case is when one image is from a patient and the other one is constructed from a database or an atlas, here the registration is called *atlas* registration.

Modalities involved:

Modalities refer to the means by which the images are acquired. Registration methods can be categorized into two main classes with respect to modalities involved in the procedure. If the images to be registered are from the same modality, it is called *monomodal* registration. *Multimodal* registration is when images are from two different modalities. Two other classes can be considered; *modality to model* and *patient to modality* when only one image is involved and the other input is either a model or the patient himself.

2.1.2. Components of registration:

Registration can be considered as an optimization problem that aims to find, iteratively, the transformation that minimizes a certain cost function or a similarity measure. Figure 2.3 shows the main components of image registration.

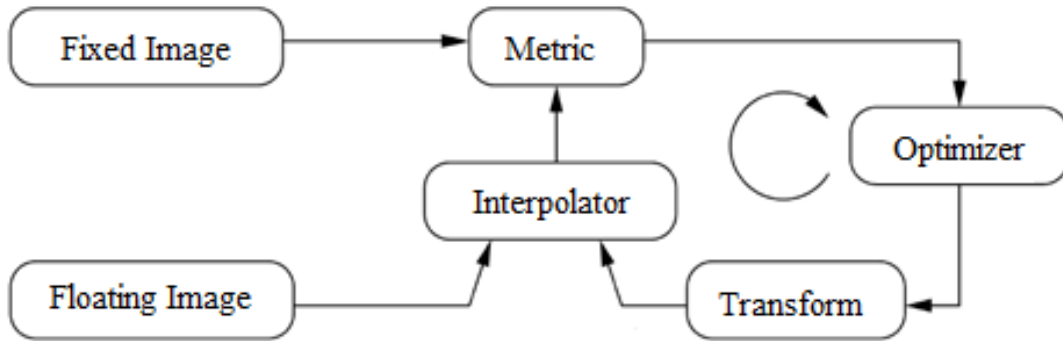


Figure 2.3. Components of registration, image from [2].

This optimization problem can be written as:

$$\hat{\phi} = \arg \min_{\phi} C(T(\phi); F(x), M(x)) \quad (1)$$

where $F(x)$ is the fixed image, $M(x)$ is the floating image, T is the spatial transformation that aligns the two images, ϕ represents the parameters vector of the transformation T , $\hat{\phi}$ is the optimal parameters set, and C is the cost function given by:

$$C = s(F(x), T(M(x))) \quad (2)$$

With s being the similarity measure used.

Similarity measure:

The similarity measure is the measurement that indicates how well the transformed floating image matches the fixed image. Since an intensity-based registration method will be considered in this work, we will focus here on the similarity measures involved in this kind of registration [9]. All these measures are extracted directly from image intensities. The choice of the appropriate measure depends on the images to be registered.

Image subtraction:

In the case of a monomodal registration, and in order to register two identical images, except for white Gaussian noise, the Sum of Squares of intensity Differences (SSD) can be considered as a similarity measure. SSD will be zero if the images are perfectly registered and will increase proportionally to the misalignment error. SSD can be given by:

$$SSD = \frac{1}{N} \sum_i (F(x_i) - T(M(x_i)))^2 \quad (3)$$

Correlation Coefficient:

When the two images are not identical but their intensities have a linear relationship (same modality with different contrast for example), the Correlation Coefficient (CC) can be considered.

$$CC = \frac{\sum_i (F(x_i) - \bar{F}(x))(T(M(x_i)) - T(\bar{M}(x)))}{\sqrt{\sum_i [F(x_i) - \bar{F}(x)]^2} \sqrt{\sum_i [T(M(x_i)) - T(\bar{M}(x))]^2}} \quad (4)$$

Mutual Information:

Other similarity measures, such as statistical classifiers, are used when intensities in both images have no direct relationship (images from two different modalities). For example, the joint histogram can be considered as a similarity measure. When normalizing the joint histogram, the joint Probability Density Function (PDF) is obtained. Another measure based on information theory is the joint entropy which is calculated from the PDF. The main problem with the entropy is that the PDF is defined only in regions where the two images overlap. Therefore, another measure was proposed, the Mutual Information (MI). MI normalizes the joint entropy with respect to the marginal entropies of the two images, and is given by:

$$MI(F, T(M)) = \sum_x \sum_y P_{fm}(x, y) \log \left(\frac{P_{fm}(x, y)}{P_f(x)P_m(y)} \right) \quad (5)$$

Optimizer:

The transformation that aligns the two images is determined iteratively using an optimizer which will determine the optimal parameters of this transformation in order to minimize (or maximize) a certain similarity measure. Several ways of optimizing the transformation may be applied. In each iteration, the optimizer calculates the similarity measure for a set of transformation parameters. In the next iteration, the optimizer tries to find a better value for transformation parameters in order to minimize the similarity measure. The step of the optimizer and the stopping criterion are usually predefined.

Two studies by [10] and [11] compared several optimization methods in terms of computation time, accuracy, precision and robustness. The most common methods include conjugate gradient [12], Powell's method [13], Amoeba (Nelder-Mead downhill simplex) [14] and Levenberg-Marquardt optimization [15].

Generally, optimizers make use of the cost function as well as its derivative. In the absence of derivatives, optimizers such as Amoeba or Powell optimizer are considered.

Interpolator:

When the transformation is determined by the optimizer, it will be applied on the floating image. An interpolator is therefore needed in order to evaluate the intensity of the floating image at non-grid positions. Different interpolators can be used, the Nearest Neighbor, Tri-linear, B-Spline, Cubic interpolators, etc. The choice must be made depending on the required precision which is influenced by interpolation-related errors and artifacts introduced in the iterative process [16].

2.2. State of the art of MRI/CT registration:

A number of MRI/CT registration techniques dedicated to prostate brachytherapy have been described in the literature. Some of them [17-19] used pelvic bones and/or implanted fiducial markers as landmarks to perform the registration. Not only that the registration was limited to rigid transformations, but it also required manual identification of anatomic landmarks or implanted markers. Out of these three methods, the one proposed by [19] had the best performance with a maximum registration error of 2.2 mm.

A comparison between two rigid registration methods; namely a landmark-based approach (where manual identification of fiducial gold markers inserted in the prostate was required) and a surface-based method using the Iterative Closest Point (ICP) algorithm was performed by [20]. The precision of the ICP method was found significantly better than the landmark-based one, with registration errors of > 2 mm in 14% of the cases, including errors of > 5 mm in some of the cases. However, manual delineation of the prostate on both modalities was required for such approach. [21] proposed a non-rigid registration between endorectal coil-based MRI/MRSI (Magnetic Resonance Spectroscopic Imaging) and CT images of the prostate. A first step consisted in manually contouring the prostate in both modalities. Then, another manual interaction consisted in placing control points in order to apply Thin-Plate Spline (TPS). Four to eight points were placed in each pair of slices along the contours of the prostate. [22] exploited the presence of seeds and needle tracks to perform the registration for post-implant dosimetry in prostate brachytherapy. Their method consisted in identifying seed trains in CT, while needle tracks and seed voids were identified in MRI. The first initial registration was followed by a mutual information-based registration. Beside the fact that the registration was limited to rigid transformations only, it was also limited by time requirements and inter-observer uncertainty associated with both the implantation and the identification of needles and seeds. The Root Mean Square (RMS) value following their registration method was of 2.1 ± 0.7 mm.

[23] non-rigidly registered planning CT and diagnostic MR prostate images for targeted prostate radiotherapy applications. The difference in the field of view (FoV) between these two images (diagnostic MRI has a small FoV centered on the prostate) makes the registration task difficult. Therefore, they made use of planning MRI, which has the same FoV as the CT, to facilitate the registration process. A first step consisted in correcting the MRI bias field inhomogeneity using an automatic low-pass filter, and then the diagnostic MR image was manually segmented. Afterwards, a supervised pixel-wise classifier was used to identify suspicious regions on the diagnostic MRI which would be subsequently registered to the planning MRI. Finally, manually identified landmarks were used to align the planning MRI with the CT using TPS. The tumor location was therefore mapped from the diagnostic MRI onto the planning CT where a targeted dose plan may be generated. Not only that their method demanded an additional modality to be acquired, but it also required some steps including manual interactions and preprocessing. An alternative approach that can enable both prostate delineation and dose planning based on the MR

image alone was proposed in [24]. They presented an atlas-based registration method that consisted in generating a pseudo-CT scan from the MR image. A heavy preprocessing step however was required. It included bias field correction, interleaving correction, anisotropy correction, smoothing, zero mean and unit variance normalization. Their atlas-based segmentation method involved an atlas with a matching set of organs labels. The atlas was registered to the image to be segmented and labels defined on the atlas were then propagated to the image.

[25] introduced a new metric, called Modality Independent Neighborhood Descriptor (MIND), for deformable multimodal registration of thoracic images. This descriptor was independent of contrast, noise levels and intensity distribution across the two images. But, at the same time, it was sensitive to the inherent image features (corners, edges, gradients, etc.). MIND was based on the concept of local image self-similarity, i.e. the assumption that a local representation of a structure is shared across modalities. These structures were estimated through the similarity of small image patches within one modality. At first, a dense set of descriptors was extracted from each image independently based on the intensity differences within a local patch around each voxel in the same modality. Then, these descriptors were compared across the two images using the Sum of Squared Differences (SSD). Theoretically, MIND is a simple measure that can be used to register images from different modalities. However, when the authors registered MR and CT images using this measure, it gave rather poor performance (Target Registration Error: TRE = 7.12 ± 5.88 mm). On the other hand, when they applied MIND in monomodal cases (CT/CT registration), the results were significantly better with a TRE value of 2.14 ± 3.71 mm.

More recently, [26] presented a non-rigid registration methodology dedicated to MRI-guided prostate brachytherapy. They used a first B-Spline-based registration followed by Finite Element Modeling (FEM), which was meant to improve the performance of the registration. Once more, their method required a manual delineation of the prostate as well as the surrounding organs. In addition, a bounding box containing the prostate on the CT image was manually defined as well. Moreover, their maximum registration errors were as big as 4.7 mm. A study in [27] compared manual and automatic registration methods for prostate radiotherapy. The manual method relied on the identification of landmarks while the automatic one was a voxel-based registration using the mutual information as a similarity measure. However, a bounding box needed to be manually

defined around the prostate to initialize the automatic registration. In addition, both methods were limited to rigid transformations only and could not therefore detect prostate deformations.

[28] presented a registration method for post-operative evaluation of prostate brachytherapy by localizing the implanted radioactive seeds. Their point-to-volume based registration method consisted in registering a point set of seeds to the MR volume. The prostate was manually delineated on the MRI at first. Afterwards, preprocessing of the MRI was needed in order to enhance the visibility of the seeds. A threshold was performed inside the contours and then morphological erosion was applied allowing the recovery and the construction of the seeds images. The accuracy of their proposed registration method relied on the hypothesis that the seeds were implanted inside the entire prostate, and that rigidly registering these seeds would yield a correct registration of the whole volume.

Therefore, to the best of our knowledge, most methods dedicated to prostate brachytherapy are limited to rigid transformations only, suffer from the use of implanted markers or require a manual step including prostate segmentation or identification of anatomical landmarks. Such step is both time consuming and subject to intra- and inter-observer variability inaccuracies depending on the experience of the user.

In this chapter, we will propose a fully automatic MRI/CT non-rigid registration method for prostate brachytherapy planning. The proposed methodology does not require any manual segmentation, landmark identification or markers to be inserted in the prostate. The registration is done in two steps; with the result of a first affine registration being used to initialize a second non-rigid registration step. In order to improve the robustness and the computational efficiency of the approach as well as prevent unwanted/unnecessary objects present in the image from affecting the process, the registration is constrained solely to volumes of interest (VOIs).

2.3. Proposed MRI/CT registration approach:

The proposed algorithm is a two-step process involving both an affine and a non-rigid registration phase. Each registration is constrained to a different VOI, which is determined automatically by detecting the prostate location. The global workflow of the proposed method is illustrated in figure 2.4.

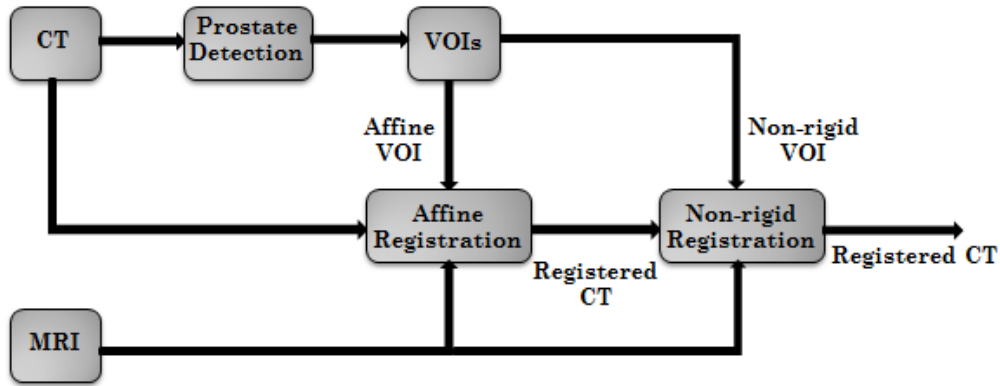


Figure 2.4. Global workflow of the proposed MRI/CT registration method.

As illustrated in figure 2.4, the proposed approach is done in several steps. At first, the prostate location is detected automatically, allowing the determination of VOIs. Then, a first affine registration, constrained to the pelvic VOI, is applied to globally align the CT and the MR images. The transformation, obtained from the first registration, is applied on the CT image, using an interpolator. Finally, the registered CT and the MR images are aligned using a second non-rigid registration step, constrained to the prostate VOI. Once again, the transformation obtained from the second registration is applied on the registered CT, using an interpolator, leading to the final image. The main components of this proposed approach are described in the following paragraphs.

2.3.1. VOIs determination:

Concerning the first affine registration, it is constrained to a volume around the pelvic structures (called pelvic VOI) assuming that the pelvis does not deform between the two acquisition and, therefore, fulfills a rigid-body hypothesis. As for the second non-rigid registration step, it is constrained to a volume around the prostate only (called prostate VOI) in order to account for local deformations in that region. These two VOIs are determined automatically following two steps; at first the prostate location is detected allowing the extraction of a CT slice containing the prostate, and then both VOIs are determined on that slice.

Concerning the first step, it is known that the prostate is situated in the pelvic cavity, behind the lower part of the pubic symphysis. From figure 2.5 we can notice that the pubic symphysis lies at the same level as the two tips (right and left) of the greater trochanter of the femurs.

Consequently, by detecting these two points we can determine the location of the pubic symphysis and, therefore, that of the prostate.

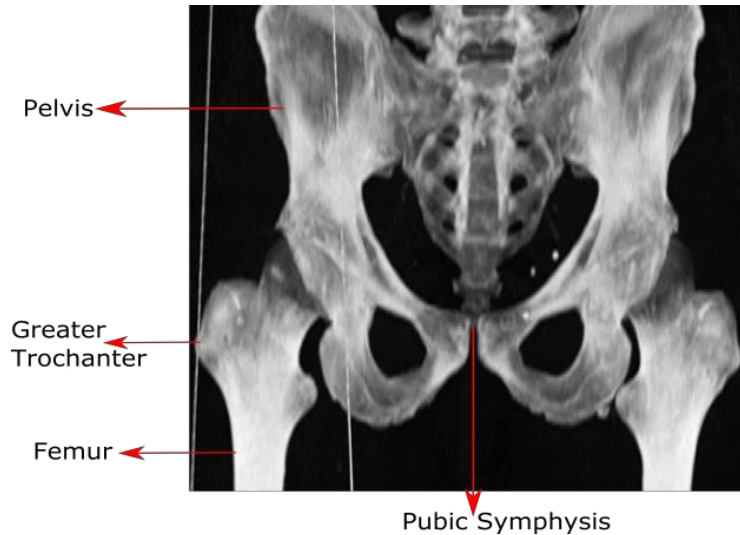


Figure 2.5. Pelvis bones.

To improve the visualization of bones and higher attenuation structures in CT, we use a volume rendering method, the Maximum Intensity Projection (MIP) [29]. For a given visualization plane, parallel rays are cast and the voxel with the maximum intensity encountered along each ray is projected onto the rendered 2D image. The rendered image will have the size of the 2D plane orthogonal to the projection direction, as illustrated in figure 2.6.

MIP is well suited for displaying bones and contrast material-filled structures, while other lower attenuation structures are not well visualized. The rendered 2D MIP image (in our case, according to the coronal axis or the y direction) is illustrated in figure 2.6(b).

Subsequently, an automatic clustering-based thresholding, using Otsu's method [30], is performed on the MIP image. This thresholding method considers that the image contains two classes of pixels following the bi-modal histogram; foreground and background pixels (in our case, bones and soft tissues respectively). Then, it calculates the optimum threshold that separates these two classes in a way that minimizes the intra-class variance. The resulting image after the thresholding operation is shown in figure 2.7(a). In order to remove any remaining artifacts that may be present in the image (like scanning bed structures), the final step involves the application of an opening morphological transformation. Opening is obtained by the erosion of an image followed by dilation. It allows, therefore, removing small objects from the image (removes small

2.3. Proposed MRI/CT registration approach

bright objects on a dark background). The image after applying the opening operation is shown in figure 2.7(b).

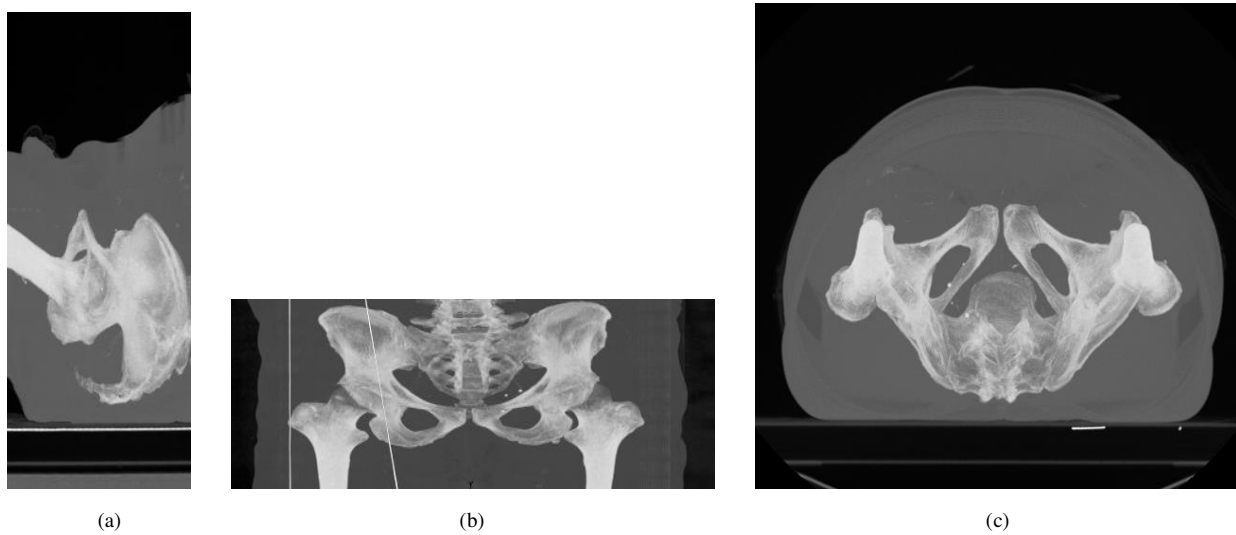
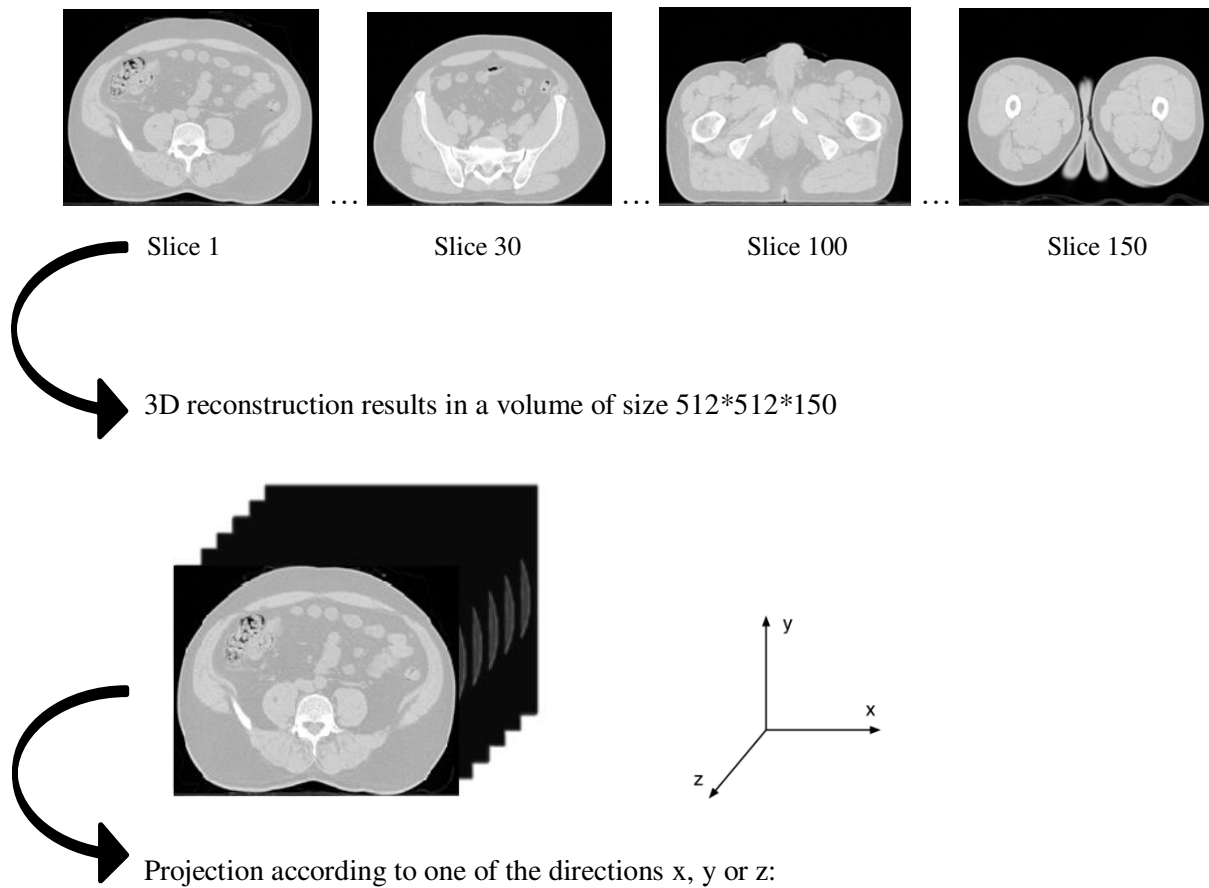


Figure 2.6. MIP projection according to (a) x direction, (b) y direction and (c) z direction. The size of (a) is 150×512 , (b) 512×150 and (c) 512×512 .



(a) (b)
Figure 2.7. MIP, (a) after thresholding, (b) after opening operation.

This final binary image is subsequently used for the detection of the tip of the greater trochanter, considering that it represents the furthest point from the central vertical axis of the image. The axial slice corresponding to the line connecting the two tips is extracted from the CT volume, as illustrated in figure 2.8.



(a) (b)
Figure 2.8. (a) MIP containing a line connecting the two tips, (b) extracted CT slice.

Since the prostate and different bony structures (femurs, ischium and pubic symphysis) can be visualized in the extracted slice, the registration will be constrained to VOIs determined automatically on this slice as described hereafter.

Starting from the previously extracted CT slice, a thresholding operation is applied in order to identify different bony structures in the image. Since this slice contains more than two classes of pixels (tissues, bones, fat), a simple automatic thresholding using Otsu's method would not work. Given that CT numbers are commonly expressed in a standardized scale called Hounsfield units (HU), CT pixel values in HU are therefore used for thresholding. Density values of some substances in HU are given in table 2.1. The upper density value of bones may change depending

2.3. Proposed MRI/CT registration approach

on the CT system and the number of bits used to encode the information. Generally, 12 bits are used to encode DICOM files allowing a range of $2^{12} = 4096$ CT values.

Table 2.1. Hounsfield units.

Substance	HU
Air	-1000
Water	0
Soft tissue	+100 to +300
Bone	+700 (cancellous bone) to +3000 HU (dense bone)

Thresholding the extracted CT slice, shown in figure 2.9(a) at 2200 HU allowed separating the bony structures as well as deleting the soft tissues. The resulting binary image is shown in figure 2.9(b).

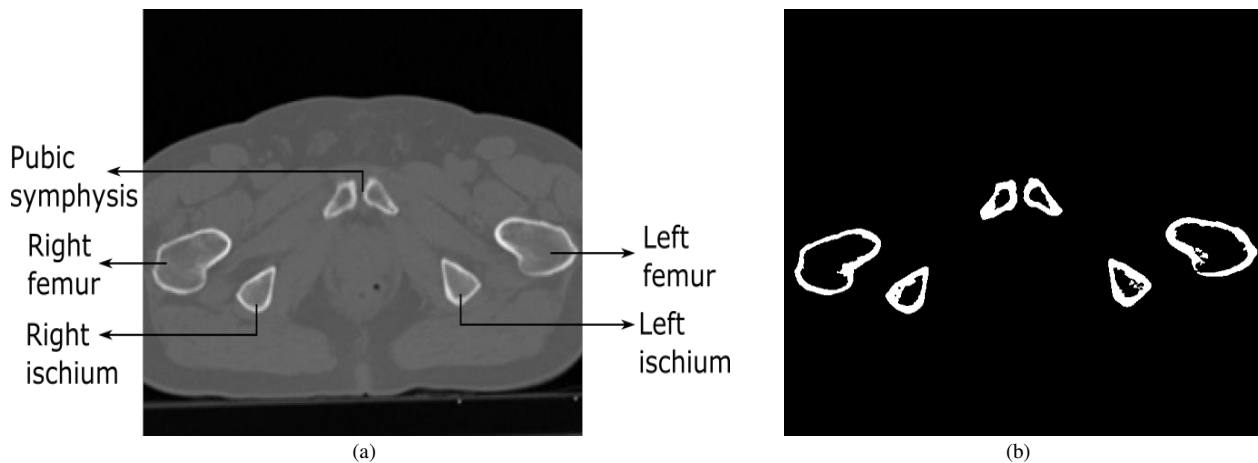


Figure 2.9. Thresholding of the extracted slice, (a) original image, (b) binary image.

ROIs are automatically defined on this binary image as follows, and then the corresponding regions are cropped in all the slices and put together to create the VOIs that would be used for the registration.

A connected-component labeling algorithm [31] is applied on the binary image, shown in figure 2.9(b). This algorithm, which is based on graph theory, is used to retrieve contours for detecting and identifying different connected regions (labels) in the image. Once the different labels of the image are identified, the surface of each label is calculated. Then, the two femurs, identified by having the biggest surfaces, are automatically excluded. A bounding box around the remaining

structure defines the pelvic ROI that would be used for the affine registration, as illustrated in figure 2.10.

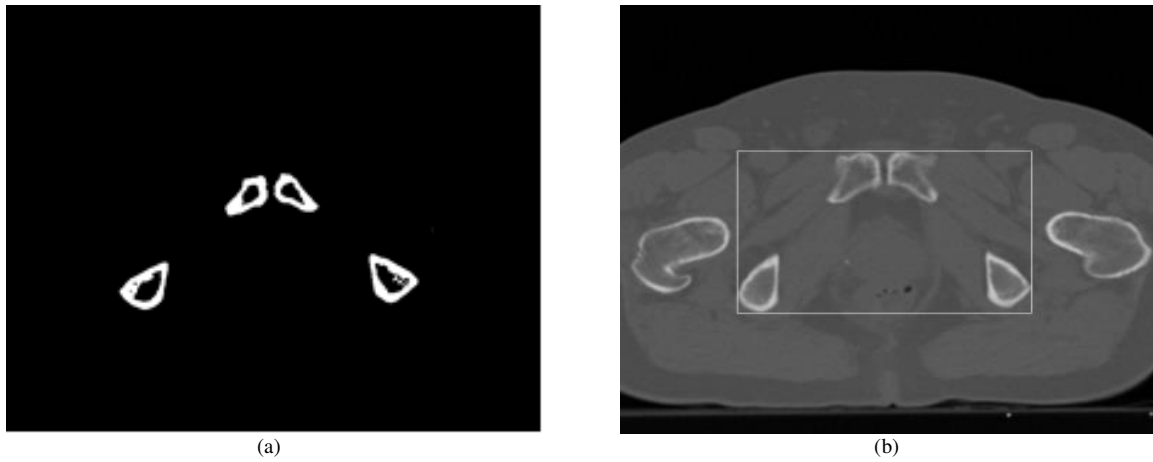


Figure 2.10. Pelvic ROI, (a) in the binary image, (b) original image.

The distance between each label pair and the central vertical axis is then calculated, allowing the identification and exclusion of the ischium by being further from this axis than the pubic symphysis. The boundaries of the pubic symphysis are then detected in order to automatically define a bounding box around the prostate, whose size is limited between the lower parts of the pubic symphysis and the ischium, and has the same width as the pubic symphysis (see figure 2.11(a)). Figure 2.11(b) shows the bounding box that defines the prostate ROI, which would be used for the non-rigid registration.

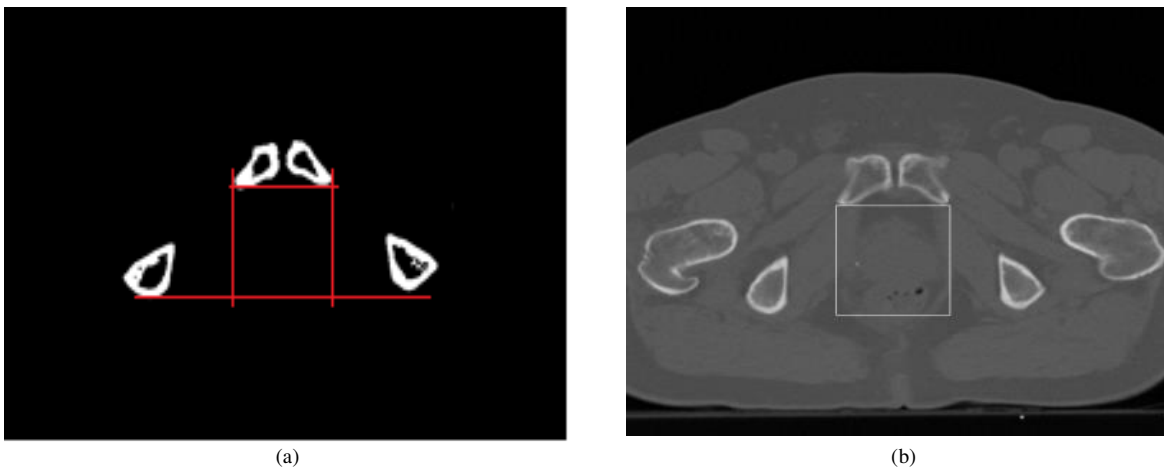


Figure 2.11. Prostate ROI, (a) in the binary image, (b) original image.

These two VOIs, which were determined automatically, would be therefore used to constrain the two-step registration process.

2.3.2. Registration:

Registration is the determination of a geometrical transformation that spatially aligns two datasets. An intensity-based registration is used in this work despite the fact that images are from different modalities and, consequently, their intensities have no simple relationship. Nevertheless, those modalities are informative of the same underlying anatomy, which means that mutual information between them can be explored. A similarity criterion referred to as Mutual Information (MI) is therefore explored for both registration steps. The main components of the proposed MRI/CT registration are described in the following paragraphs.

Similarity measure:

Mutual Information, first implemented by [33], is directly calculated from voxel values rather than geometrical structures such as points or surfaces. Therefore, the calculation is not limited by segmentation or landmark detection and it does not require any manual interaction, which facilitates the automation of the registration process. Moreover, this measure does not make any assumptions regarding the relationship between the image intensities nor impose any constraints on the modalities involved. MI is based on statistics and is derived from probabilistic measures of image intensity values. According to information theory, the degree of the dependency between two images, or the amount of information that one image contains about the other, is given by the MI between the image intensities of corresponding voxels in both images. MI measures the distance between probability densities, and it is based on the shared information between the overlapping regions in the two images to be aligned. Let I_f and I_m be the fixed and the moving (or floating) image respectively, MI is defined in terms of entropy (H) as follows:

$$MI(I_f, I_m) = H(I_f) + H(I_m) - H(I_f, I_m) \quad (6)$$

The entropy is calculated from the PDF $P_x(i)$, which represents the probability of a pixel of the image X to have the intensity value i . The marginal entropies $H(I_f)$, $H(I_m)$ and the joint entropy $H(I_f, I_m)$ are given by the following equations:

$$H(I_f) = -\sum_x P_f(x) \log P_f(x), \quad H(I_m) = -\sum_x P_m(x) \log P_m(x) \quad (7)$$

$$H(I_f, I_m) = -\sum_x P_{fm}(x, y) \log P_{fm}(x, y) \quad (8)$$

Thus, MI would be calculated from the PDF as in the equation:

$$MI(I_f, I_m) = \sum_x \sum_y P_{f_m}(x, y) \log \left(\frac{P_{f_m}(x, y)}{P_f(x)P_m(y)} \right) \quad (9)$$

This measure would be maximized if I_f and I_m were perfectly aligned. On the other hand, if I_f and I_m were independent then $P_{f_m}(x, y) = P_f(x) * P_m(y)$ and the measure would be zero.

Since marginal and joint PDFs cannot be computed directly, they are estimated using Parzen windows [34], also known as Kernel Density Estimation (KDE). KDE is essentially a data interpolation technique where inferences about the probability function are made based on a data sample. At first, the image is uniformly sampled on discrete bins. In our implementation of MI, we followed the work in [35] rather than the one done by [33]. The main difference between these two implementations is that in [35] only one set of samples is used for the whole registration process instead of using new samples every iteration. Therefore, this would result in a much smoother cost function.

The PDF is then estimated at these discrete bins by superimposing kernel functions (Gaussian or B-spline kernel for example) centered on the intensity samples, as shown in the figure 2.12. To estimate the value of the PDF $P(x)$ at a certain position x , a window (kernel) is placed at that position and the number of observations x_i that fall within this kernel (the contribution of each observation to this kernel) is determined. The value of PDF is estimated by summing the contribution of these observations to this kernel. The estimation of PDF is therefore given by:

$$P(x) = \frac{1}{N} \sum_{x_i \in X} K(x - x_i) \quad (10)$$

where X is the samples taken from the image, and K is the kernel function.

Once the PDFs have been estimated, the Mutual Information can be subsequently computed according to (9).

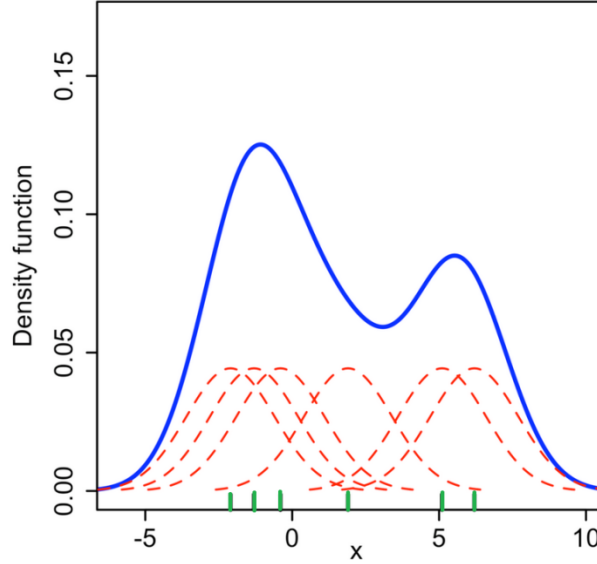


Figure 2.12. Parzen windowing, image is sampled on 6 discrete bins (green), the 6 individual kernel functions centered on those bins are shown in red, the density estimate is shown in blue.

Optimizer:

The transformation that maximizes the MI between the MR and CT images for both registration steps is determined iteratively using a regular step gradient descent optimizer [36]. This optimizer is an improved form of the original gradient descent optimizer that avoids taking too large steps. At each iteration, the optimizer takes a step in the direction of the derivative of the cost function. The initial step length is set by the user. Whenever the optimizer determines that the direction of the derivative changes, meaning that a local maximum has been passed, the step length is reduced by a factor (called relaxation factor) also set by the user. Since the step may be reduced many times in the optimization process, after a certain number of iterations the optimizer will be moving slowly in a restricted area of the transformation parameters space. Therefore, the user can also define a minimum step length that controls the accuracy by defining when the convergence has been achieved. The approach can be formulated as a maximization problem:

$$\hat{\phi} = \arg \max_{\phi} (MI(\phi; I_f, I_m)) \quad (11)$$

Where, ϕ represents the parameters vector of the transformation $T(\phi)$, and $\hat{\phi}$ is the optimal set of parameters of the transformation that aligns $I_m(T(X, \phi))$ with I_f . The optimal set of parameters is determined iteratively using the optimization strategy as follows:

$$\phi_{k+1} = \phi_k + a_k d_k \quad (12)$$

where d_k is the search direction, and a_k is a factor controlling the step size.

Transformation:

Before the registration, the CT was resampled in a way that centralizes both images and makes them have the same dimensions. A first affine registration step is then applied to globally align the two images by namely correcting the scale, while the non-rigid registration step that follows is used to determine the local deformations of the prostate. Consequently, the affine registration helps initializing the non-rigid registration step with a solution that is close to the optimal one, improving both robustness and computation time as well as reducing the probability of local maxima for the non-rigid registration. The initial registration, constrained on the pelvic VOI, is based on an affine model (rigid plus scaling and shearing) with 12 DoF. As for the non-rigid registration, which is restricted to the prostate VOI, a model based on cubic B-Spline functions is used to detect the local deformations between the two images (registered CT and MR images).

B-Spline defines a deformation field according to some uniformly spaced control points located on a coarse grid called B-Spline grid. The number of DoF in N-D dimension is given by:

$$DoF = CP^N \times N \quad (13)$$

where CP is the number of control points per dimension.

For a 3D image, a grid of 8 controls points in each dimension therefore results in a transformation with $8^3 \times 3 = 1536$ DoF.

The deformation field, that spatially aligns the two images, is calculated by interpolating deformation values of the control points, as illustrated in figure 2.13.

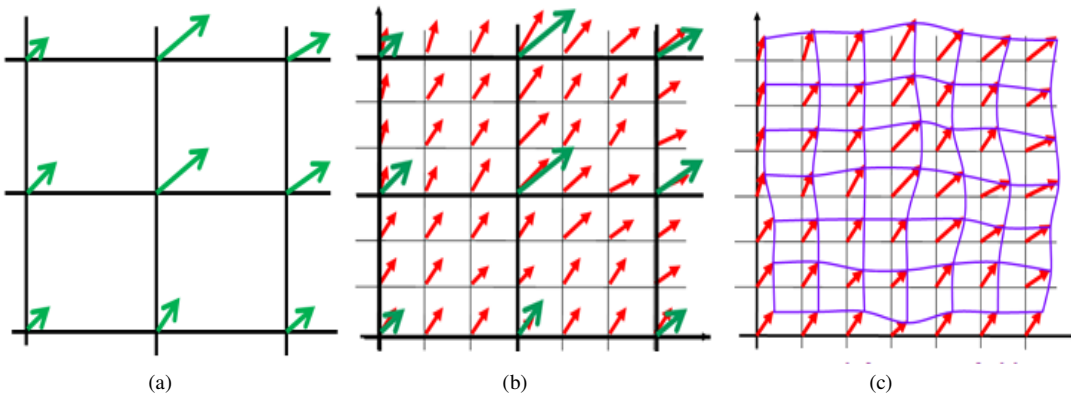


Figure 2.13. 2D B-Spline, (a) B-Spline grid, (b) deformation vectors, (c) deformation field, image from [2].

The choice of B-Splines rather than Thin-plate Splines or elastic-body Splines was because B-Splines have the advantage of being globally-smooth but, at the same time, locally-controlled (changing one control point affects the transformation at the local neighborhood of that point only). We followed the implementation of the B-Spline model that was proposed in [32] who considered the transformation model as a formulation of a free-form deformation based on tensor product of B-Splines of degree d (order $d+1$). Usually, $d = 3$ for cubic B-Splines. Let $\phi_{i,j,k}$ be the $n_x \times n_y \times n_z$ grid of control points with uniform spacing. At any position $X=(x, y, z)$, the free-form deformation is computed from the positions of the surrounding $(d+1) \times (d+1) \times (d+1)$ neighborhood of control points.

$$T(X) = \sum_{l=0}^d \sum_{m=0}^d \sum_{n=0}^d B_l(u) B_m(v) B_n(w) \phi_{i+l, j+m, k+n} \quad (14)$$

where i, j and k are the indices of the control point cell containing X and are given by:

$$i = \left\lfloor \frac{x}{n_x} \right\rfloor - 1, \quad j = \left\lfloor \frac{y}{n_y} \right\rfloor - 1, \quad k = \left\lfloor \frac{z}{n_z} \right\rfloor - 1 \quad (15)$$

And where u, v and w denote the relative positions of X inside that cell and are given by:

$$u = \frac{x}{n_x} - \left\lfloor \frac{x}{n_x} \right\rfloor, \quad v = \frac{y}{n_y} - \left\lfloor \frac{y}{n_y} \right\rfloor, \quad w = \frac{z}{n_z} - \left\lfloor \frac{z}{n_z} \right\rfloor \quad (16)$$

Finally, B_l is the l 'th basis function of the B-Spline of degree d . The most used B-spline functions are given by the following equations:

$$B_0(u) = (1-u)^3 / 6 \quad (17)$$

$$B_1(u) = (3u^3 - 6u^2 + 4) / 6 \quad (18)$$

$$B_2(u) = (-3u^3 + 3u^2 + 3u + 1) / 6 \quad (19)$$

$$B_3(u) = u^3 / 6 \quad (20)$$

The derivative of the deformation field with respect to the B-Spline coefficients is calculated according to:

$$\frac{\partial T(X)}{\partial \phi_{i,j,k}} = B_l(u) B_m(v) B_n(w) \quad (21)$$

where:

$$l = i - \left\lfloor \frac{x}{n_x} \right\rfloor + 1, \quad m = j - \left\lfloor \frac{y}{n_y} \right\rfloor + 1, \quad n = k - \left\lfloor \frac{z}{n_z} \right\rfloor + 1 \quad (22)$$

Interpolation:

Once the transformation is determined, it is applied to the floating image (in our case, the CT). In order to calculate floating image intensities at non-rigid positions, an interpolator is used.

The floating image can be resampled onto the fixed image grid in two different ways; forward and inverse mapping (figure 2.14).

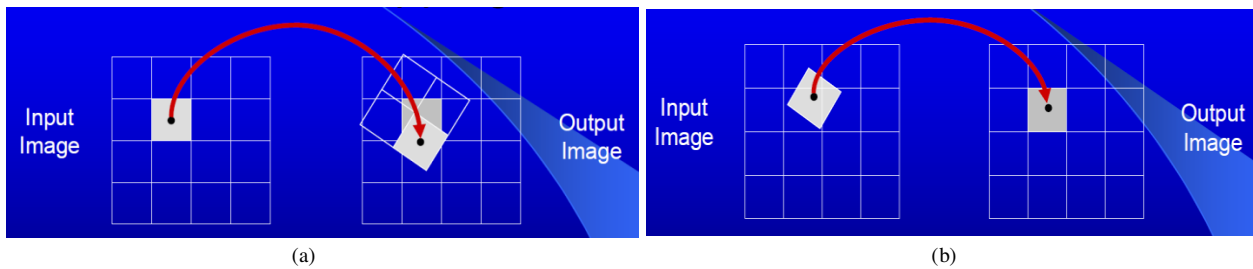


Figure 2.14. Types of resampling, (a) forward and (b) inverse mapping, image from [19].

In forward mapping, voxels of the input (floating) image are directly mapped onto the output (fixed) image using the estimated transformation. Therefore, this discretization can produce holes (output voxel with no correspondences) and/or overlaps (output voxels with more than one correspondence). In inverse mapping, on the other hand, output voxels are mapped back onto the input image. Therefore, output voxel value must be interpolated from a neighborhood in the input image. The inverse mapping was used since it has the advantage of avoiding holes and overlaps in the output image, because all voxels are scanned sequentially.

Although higher-order interpolation methods could give more accurate results, the tri-linear interpolator was used for both registration steps because it offers a good compromise between accuracy and computational efficiency.

2.4. Implementation:

The proposed registration method was implemented in C++ on a windows 7 environment using the Insight Segmentation and Registration Toolkit (ITK, www.itk.org/). The DICOM image reader, integrated in the library of Visualization Toolkit (VTK, www.vtk.org/), was used for reading the images. VTK was also used, along with Qt (www.qt.io/), for developing a Graphical User Interface (GUI) for viewing the registration results and for the manual interaction that consisted in the placement of radioactive sources in order to simulate an intraoperative radiotherapy environment. For the ROI determination, Open source Computer Vision (OpenCV, opencv.org/) was used.

A software called BrachyPlan was developed in order to automate the procedure of the registration. This software is focused on the planning phase of the prostate brachytherapy. It aims to accurately plan the positions of the radioactive sources and to clearly visualize the personalized dose distribution (PDD) with respect to the tumor.

As mentioned before, a PDD that considers soft tissues heterogeneity can be done using Monte Carlo simulation based on a pre-operative CT image using the toolkit Graphics Processing Unit (GPU) GEant4-based Monte carlo Simulations (GGEMS, www.ggems.fr) [37, 38]. Since CT is not well adapted for visualizing soft tissues, the MRI is introduced and coupled with the CT.

A GUI allows the user to select the patient's folder containing MR and CT DICOM files. Once the patient is selected, the registration between MR and CT images is done automatically without any user interaction. When the registration is done, only the MR image is visualized; in 3D as well as in axial view (figure 2.15).

Then, the user can start placing the radioactive sources on different slices of the MRI using the mouse. Figure 2.16 shows an MRI slice after placing a few sources on it.

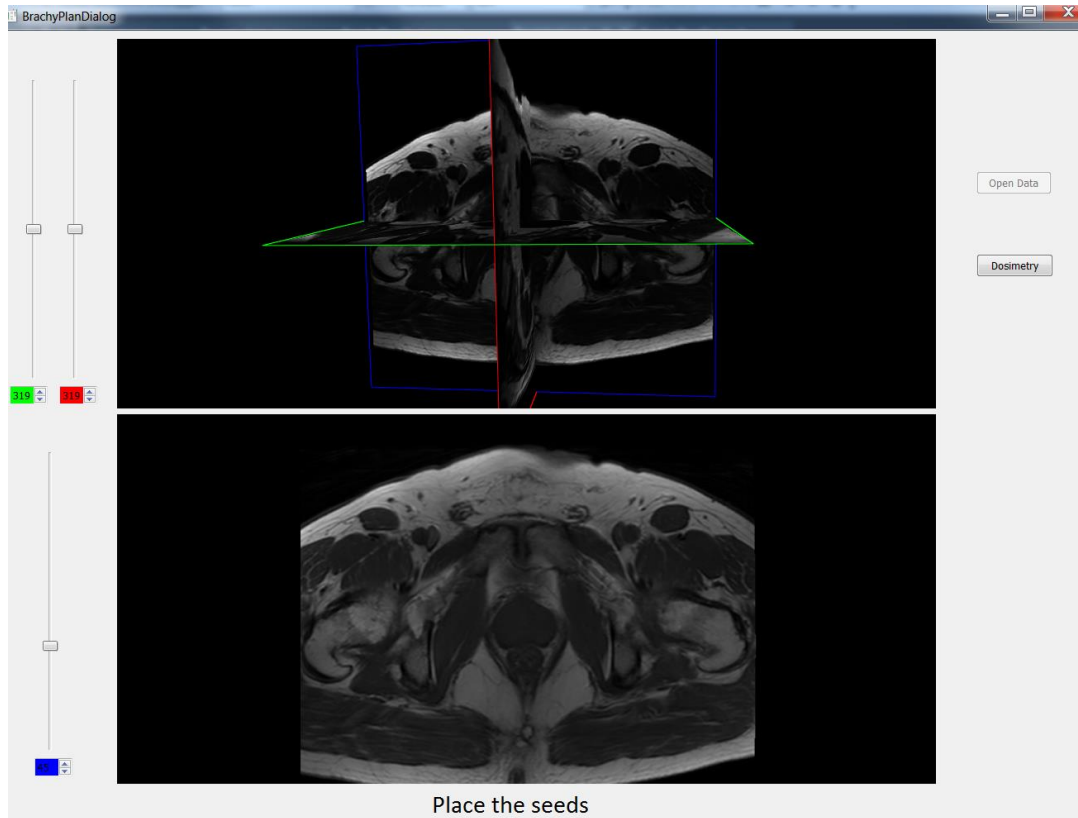


Figure 2.15. GUI showing MRI after MRI/CT registration, top: 3D view and bottom: axial view.

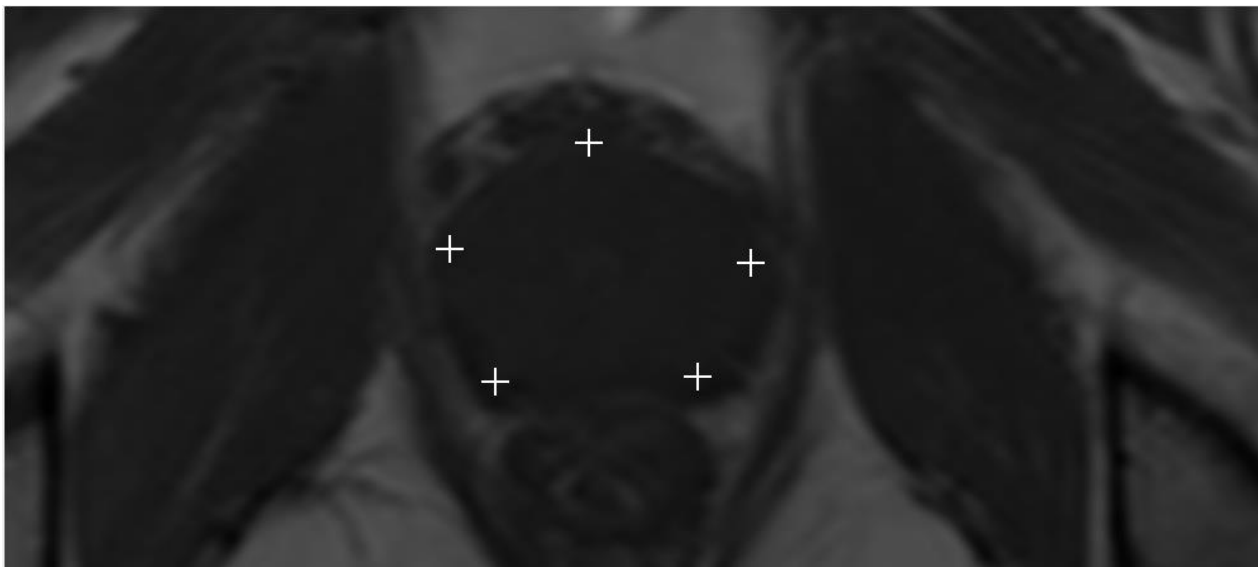


Figure 2.16. Placing sources on the MRI.

Afterwards, when the user finishes placing the radioactive sources, clicking on the “Dosimetry” button, as its name indicates, would initiate the tool responsible for computing the dosimetry. This tool, developed on GPU, takes the positions of the sources as well as a CT image as inputs,

and gives a dose map on its output. Therefore, once the button has been clicked, the positions of the sources will be transferred from the MRI onto the registered CT image, through the transformation obtained from the registration process. Subsequently, the dosimetry calculation can be initiated on the CT image and the generated dose map can be transferred back to the MRI, once again through the registration. Finally, the dose map can be visualized on the MRI, for instance in the form of isodose lines (lines joining the points of equal percentage depth dose) as illustrated in figure 2.17:

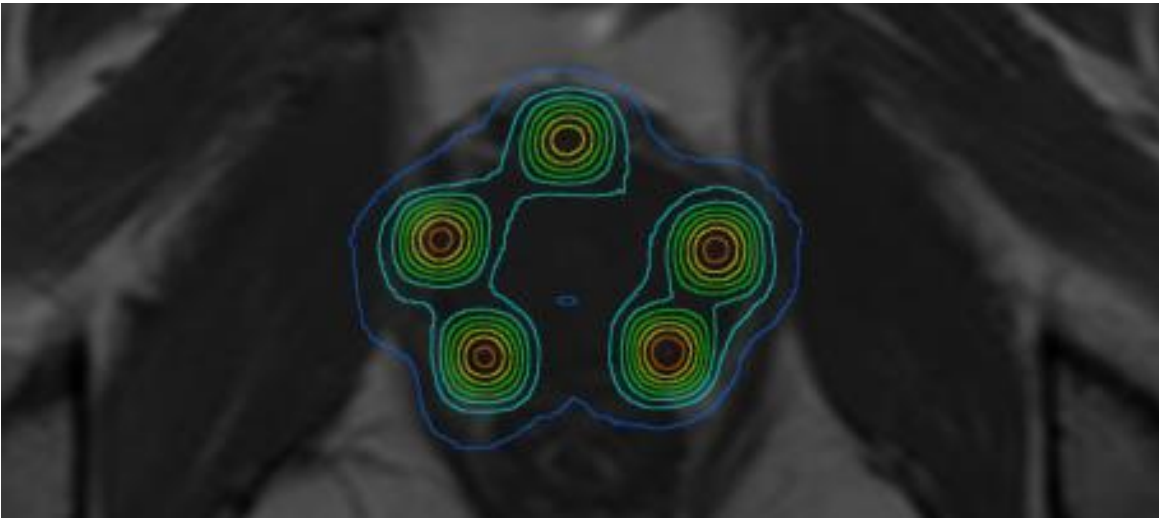


Figure 2.17. Isodose lines on the MRI.

2.5. Conclusion:

In this chapter we presented a non-rigid registration methodology between MR and CT images dedicated to prostate brachytherapy planning. This method is fully automatic where no manual segmentation or identification of landmark is required. The proposed method is based on the maximization of the Mutual Information in combination with a deformation field parameterized by cubic B-Splines. The registration is done in two steps; a first affine registration is used to initialize a second non-rigid registration step. Each registration was constrained to a different VOI in order to improve the robustness and the computational efficiency of the approach. A complete validation study using both qualitative and quantitative evaluation criteria will be presented in chapter 4.

References:

- [1] Mani VRS and Arivazhagan S (2013). "Survey of Medical Image Registration". *Journal of Biomedical Engineering and Technology*. **1(2)**: 8-25.
- [2] Ibanez L, Schroeder W, NG L, and Cates J (2005). "The ITK Software Guide". Kitware, Inc. second edition.
- [3] Maintz JBA and Viergever MA (1996). "An overview of Medical Image Registration Methods". *Symposium of the Belgian hospital physicists association*.
- [4] Reddy JN (2006). "An introduction to the Finite Element Method". 3rd Edition. McGraw-Hill.
- [5] Rueckert D, Sonoda LI, Hayes C, Hill DL, Leach MO, and Hawkes DJ (1999). "Nonrigid Registration Using Free-Form Deformations: Application to Breast MR Images". *IEEE Transactions on Medical Imaging*. **18(8)**: 712-21.
- [6] Davis MH, Khotanzad A, Flamig DP, and Harms SE (1997). "A physics-based coordinate transformation for 3D image matching". *IEEE Transaction on Medical Imaging*. **16(3)**: 317-28.
- [7] Vercauteren T, Pennec X, Perchant A, and Ayache N (2009). "Diffeomorphic demons: efficient non-parametric image registration". *Neuroimage*. **45(1)**: 61-72.
- [8] Crum WR, Hartkens T, and Hill DL (2004). "Non-rigid image registration: theory and practice". *The British Journal of Radiology*. **77(2)**: 140-53.
- [9] Fitzpatrick JM and Sonka M (2000). "Medical Imaging, volume 2. Medical Image Processing and Analysis". *SPIE-The international society for optical engineering, Bellingham, Washington, USA*. **Chapter 8**: Image registration.
- [10] Klein S, Staring M, and Pluim JP (2007). "Evaluation of optimization methods for nonrigid medical image registration using mutual information and B-splines". *IEEE Transactions on Image Processing*. **16(12)**: 2879-90.
- [11] Maes F, Vandermeulen D, and Suetens P (1999). "Comparative evaluation of multiresolution optimization strategies for multimodality image registration by maximization of mutual information". *Medical Image Analysis*. **3(4)**: 373-86.
- [12] Hestenes M and Stiefel E (1952). "Methods of Conjugate Gradients for Solving Linear Systems". *Journal of Research of the National Bureau of Standards*. **49(6)**: 409-36.
- [13] Powell MJD (1962). "An iterative method for finding stationary values of a function of several variables". *The Computer Journal*. **5(47)**: 147-51.
- [14] Nelder JA and Mead R (1965). "A simplex method for function minimization". *The Computer Journal*. **7(4)**: 308-13.
- [15] Marquardt DW (1963). "An algorithm for least-squares estimation of nonlinear parameters". *SIAM Journal on Applied Mathematics*. **11(2)**: 434-41.

- [16] Pluim JP, Maintz JBA, and Viergever MA (2000). “Interpolation artefacts in mutual information-based image registration”. *Computer Vision and Image Understanding*. **77(2)**: 211-32.
- [17] van Dalen JA, Huisman HJ, Welmers A, and Barentsz JO (2003) “Semi-automatic image registration of MRI to CT data of the prostate using gold markers as fiducials”. *Biomedical Image Registration 2nd International Workshop, WBIR*. 311-20.
- [18] Parker CC, Damyanovich A, Haycocks T, Haider M, Bayley A, and Catton CN (2003) “Magnetic resonance imaging in the radiation treatment planning of localized prostate cancer using intra-prostatic fiducial markers for computed tomography co-registration” *Radiotherapy and Oncology*. **66(2)**: 217-24.
- [19] Servois V, Chauveinc L, El Khoury C, Lantoine A, Olivier L, Flam T, Rosenwald JC, Cosset JM, and Neuenschwander S (2003) “Comparaison de deux méthodes de recalage d’images de scanographie et d’IRM en curiethérapie prostatique. Intérêt pour l’évaluation thérapeutique”. *Cancer/Radithérapie*. **7(1)**: 9-16.
- [20] Huisman HJ, Futterer JJ, van Lin EN, Welmers A, Scheenen TW, van Dalen JA, Visser AG, Witjes JA, and Barentsz JO (2005) “Prostate cancer: precision of integrating functional MR imaging with radiation therapy treatment by using fiducial gold markers”. *Radiology*. **236(1)**: 311-17.
- [21] Lian J et al. (2004) “Mapping of the prostate in endorectal coil-based MRI/MRSI and CT: A deformable registration and validation study”. *Medical Physics*. **31(11)**: 3087-94.
- [22] Vidakovic S, Jans HS, Alexander A, and Sloboda RS (2007) “Post-implant computed tomography-magnetic resonance prostate image registration using feature line parallelization and normalized mutual information”. *Journal of Applied Clinical Medical Physics*. **8(1)**: 21-32.
- [23] Chappelow J, Both S, Viswanath S, Hahn S, Feldman M, Rosen M, Tomaszewski J, Vapiwala N, Patel P, and Madabhushi A (2010) “Computer-assisted targeted therapy (CATT) for prostate radiotherapy planning by fusion of CT and MRI”. *SPIE 7625 Medical Imaging 2010: Visualization, image-guided procedures and modeling*.
- [24] Dowling J, Lambert J, Parker J, Greer PB, Fripp J, Denham J, Ourselin S, and Salvado O (2010) “Automatic MRI Atlas-Based External Beam Radiation Therapy Treatment Planning for Prostate Cancer”. *Prostate cancer imaging. Computer-Aided Diagnosis, prognosis and Intervention*. **6367**: 25-33.
- [25] Heinrich MP, Jenkinson M, Bhushan M, Matin T, Gleeson FV, Brady SM, and Schnabel JA (2012) “MIND: Modality Independent Neighborhood Descriptor for Multi-Modal Deformable Registration”. *Medical Image Analysis*. **16(7)**: 1423-35.
- [26] Zhong H, Wen N, Gordon JJ, Elshaikh MA, Movsas B, and Chetty IJ (2015) “An adaptive MR-CT registration method for MRI-guided prostate cancer radiotherapy”. *Physics in Medicine and Biology*. **60(7)**: 2837-51.
- [27] Korsager AS, Carl J, and Riis Ostergaard L (2016) “Comparison of manual and automatic MR-CT registration for radiotherapy of prostate cancer”. *Journal of Applied Medical Physics*. **17(3)**: 294-303.

- [28] Dehghan E, Le Y, Lee J, Song DY, Fichtinger G, Prince JL (2016) “CT and MRI fusion for postimplant prostate brachytherapy evaluation”. *IEEE ISBI*. 625-28.
- [29] Wallis JW, Miller TR, Lerner CA, and Kleerup EC (1989) “Three-dimensional display in nuclear medicine”. *IEEE Transaction on Medical Imaging*. **8(4)**: 297-303.
- [30] Otsu N (1979) “A threshold selection method from gray-level histograms”. *IEEE Transaction on Systems, Man, and Cybernetics*. **9(1)**: 62-6.
- [31] Suzuki S and Abe K (1985) “Topological structural analysis of digitized binary images by border following”. *Computer Vision, Graphics, and Image Processing*. **30(1)**: 32-46.
- [32] Rueckert D, Sonoda LI, Hayes C, Hill DL, Leach MO, and Hawkes DJ (1999) “Nonrigid registration using free-form deformations: application to breast MR images”. *IEEE Transactions on Medical Imaging*. **18(8)**: 712-21.
- [33] Viola P and Wells WM (1997) “Alignment by maximization of mutual information”. *International Journal of Computer Vision*. **24(2)**:137-54.
- [34] Parzen E (1962) “On Estimation of a Probability Density Function and Mode”. *Annals of Mathematical Statistics*. **33(3)**:1065-76.
- [35] Mattes D, Haynor DR, Vesselle H, Lewellyn TK, and Eubank W (2001) “Nonrigid multimodality image registration”. *Proc. SPIE 4322, Medical Imaging 2001: Image Processing* 1609.
- [36] Snyman JA (2005) “Practical Mathematical Optimization. An Introduction to Basic Optimization Theory and Classical and New Gradient-Based Algorithms”. *Springer Applied Optimization* **97**.
- [37] Lemaréchal Y, Bert J, Falconnet C, Després P, Valeri A, Schick U, Pradier O, Garcia MP, Boussion N, and Visvikis D (2015) “GGEMS-Brachy: GPU GEant4-based Monte Carlo simulation for brachytherapy applications”. *Physics in Medicine and Biology*. **60(13)**: 4987-5006.
- [38] Bert J, Perez-Ponce H, El Bitar Z, Jan S, Boursier Y, Vintache D, Bonissent A, Morel C, Brasse D, and Visvikis D (2013) “Geant4-based Monte Carlo simulations on GPU for medical applications”. *Physics in Medicine and Biology*. **58(16)**: 5593-611.

Intra-operative US/MRI Registration

In this chapter, a fully automatic non-rigid US/MRI registration is proposed. This registration aims to improve the visualization during the intervention to help the clinician correctly place the radioactive sources in their pre-planned positions. This registration has a potential benefit for prostate biopsy procedures as well, where a US/MRI registration is also necessary. Similarly to the pre-operative registration presented in chapter 2, the intra-operative registration should compensate for prostate deformations. The MRI is acquired before the intervention while the US is a real-time modality that is acquired during the intervention. Therefore, there would be some deformations in prostate size and form caused by the temporal evolution, different bladder and rectum fillings as well as patient motion. In addition, the insertion of the needles and the pressure of the TRUS probe will induce important deformations to the prostate which is in direct contact with the rectum wall. As such, a non-rigid registration is necessary.

3.1. State of the art of US/MRI registration:

A number of registration techniques dedicated to prostate procedures (biopsy and brachytherapy) have been described in the literature. Most of them are focused on ultrasound-based applications, since the US is the current modality of choice for intra-operative imaging during image-guided prostate interventions due to many factors; its non-ionizing radiation, easy to operate, widely accessible and inexpensive. However, the use of this modality as a guiding system is difficult because of its poor contrast. Therefore, to improve the visualization during the biopsy or the placement of the radioactive sources, a lot of research work has been focused on introducing another modality, such as the MRI. Consequently, registering the intra-operative US with the pre-operative MRI is of great interest for prostate targeted biopsy and brachytherapy applications.

US/MRI registration techniques can be divided into several groups; surface-based, point-based and intensity-based methods.

3.1.1. Surface-based registration methods:

Surface-based methods are the most common registration techniques. They consist in delineating the prostate in both images and then aligning these two prostate surfaces according to a certain cost function. Numerous studies using this approach have been described in the literature, such as [1] who non-rigidly registered TRUS and MR images for prostate brachytherapy applications. This technique however required the prostate to be manually segmented on both modalities at first. 3D point clouds were constructed from prostate contours, and then the Hausdorff distance between them was minimized. A pre-registration, which consisted in superimposing the centers of gravity of these two point clouds, was used as initialization for the registration. Their registration was at first validated on a prostate phantom, and then on 11 clinical patient datasets. The average distance between both point clouds following their non-rigid registration was of 1.11 ± 0.54 mm with minimum and maximum error values of 0.09 mm and 4.05 mm, respectively.

Other studies made use of pre-operative TRUS images in order to register real-time (or intra-operative) TRUS and MR images for targeted prostate biopsy applications [2, 3]. The method presented in [2] consisted in registering the MRI with the real-time intra-operative TRUS by combining the registrations between pre-operative TRUS and real-time TRUS, and between MRI and pre-operative TRUS as follows.

$$T_{MRI \rightarrow intra-TRUS} = T_{MRI \rightarrow pre-TRUS} * T_{pre-TRUS \rightarrow intra-TRUS} \quad (1)$$

where T represents the alignment between two modalities, $T_{MRI \rightarrow pre-TRUS}$ is an initial manual registration that aligns the MRI with the pre-operative TRUS, the operator $*$ represents the concatenation of transformations, and $T_{pre-TRUS \rightarrow intra-TRUS}$ is determined by the electromagnetic tracking system and the ultrasound probe calibration as follows:

$$T_{pre-TRUS \rightarrow intra-TRUS} = T_{pre-TRUS \rightarrow localizer} * T_{localizer \rightarrow intra-TRUS} \quad (2)$$

Where $T_{localizer \rightarrow intra-TRUS}$ is determined by the probe calibration, and $T_{pre-TRUS \rightarrow localizer}$ is computed during the 3D reconstruction of the pre-operative TRUS. The reconstructed pre-operative TRUS is in a fixed position relative to the localizer, and can be therefore used as a reference for motion compensation. However, their method required a manual segmentation of the prostate in both modalities. In [3] the prostate segmentation was done semi-automatically on the MRI as well as on the pre-operative TRUS; the user had to manually identify 4 points along the prostate contour from which the outline of the prostate is estimated using a discrete dynamic contour. Afterwards, an intensity-based non-rigid registration is applied to align the two triangulated prostate surfaces using an adaptive focus deformable model. The MRI volume was then elastically warped, using boundary conditions, and interpolated to match the TRUS volume. Finally, during the biopsy, the pre-operative TRUS volume and the warped MRI volume were both readjusted in a way that corresponds with the real-time 2D TRUS in order to compensate the prostate motion. The average Fiducial Registration Error (FRE) of their proposed method was of 3.06 ± 1.41 mm.

Some studies were focused on biomechanical modeling of the prostate, such as [4] who compared two solutions for non-rigid registration of US and MR prostate images. The first method consisted at first in manually delineating the prostate on both modalities. A first rigid registration was applied on the two prostate surfaces using the ICP method. Then, this rigid registration was used as an initialization for a deformable B-spline registration between binary label maps, obtained from the manual segmentation of the prostate, based on the maximization of the mutual information. As for the second solution, it was based on a biomechanical model of the prostate tissue using FEM. Although the second solution gave superior results ($TRE = 3.2 \pm 1.3$ mm) compared to the first, it required however a manual segmentation of the prostate on both modalities. A study in [5] proposed a registration technique to fuse TRUS and MR images of the prostate. At first, the prostate was manually delineated on the MRI. Then, a probabilistic model of prostate location on TRUS was built, using intensity and texture features. Finally, the probabilistic model was non-rigidly registered to the manually segmented prostate on the MRI using B-spline transformations, resulting in RMS value of 3.39 ± 0.85 mm.

[6] introduced a new TRUS/MRI registration method for prostate interventions in cases where some data might be missing, such as incomplete contours on TRUS. Their method combined the Gaussian Mixtures Model (GMM) with a biomechanical regularization using FEM.

At first, the prostate was manually delineated. Then, the registration between the two surfaces was considered as an Expectation-Maximization (EM) problem. In other words, the complete surface (from MRI) was used to compute a PDF that defines the prostate boundaries, while the incomplete surface (from TRUS) was considered as a set of observations. Finally, the deformation field, that maximizes the likelihood that the observations are propagated from a transformed PDF, was found. The TRE following their registration methodology was of 2.6 mm. An overview of their proposed method is illustrated in figure 3.1.

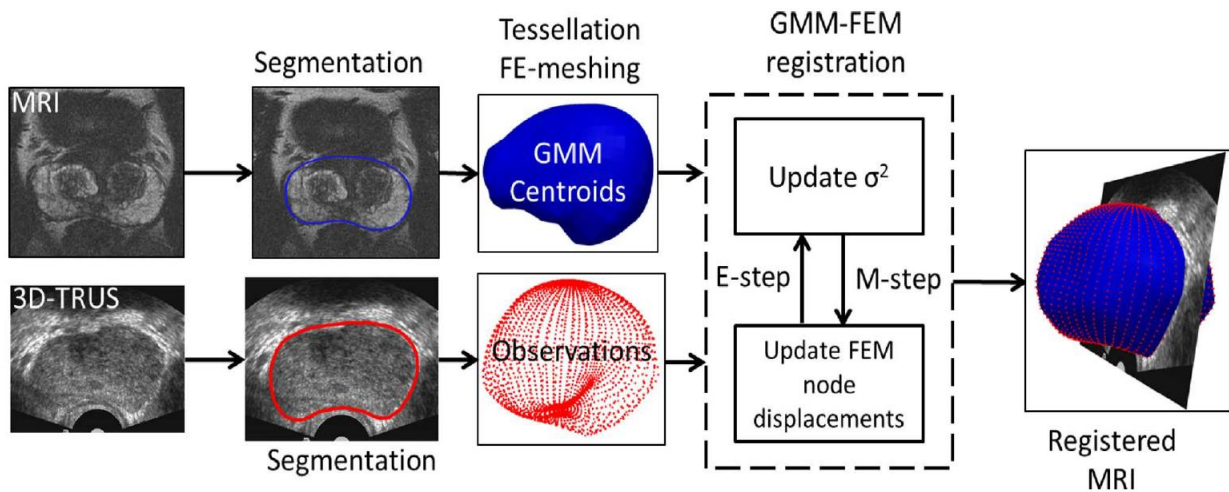


Figure 3.1. Overview of the GMM-FEM method, where σ^2 is the variance of Gaussian components, E is Young's modulus and M is the number of GMM centroids, image from [6].

3.1.2. Point-based registration methods:

Point-based registration methods involve extracting, manually or automatically, landmarks from both images, then aligning the corresponding points between the two images. Some studies like [7] proposed generating optimal correspondences automatically in order to non-rigidly register TRUS and MRI using TPS transformations for targeted prostate biopsy. Generating correspondences was done using the prostate shape geometry, as illustrated in figure 3.2.

Normalized mutual information is used in order to determine the optimal number of correspondences which are extracted from the prostate contours using Principal Component Analysis (PCA). Not only that their method was limited to 2D images only, but the user also had to manually choose an MR slice that corresponds to the US slice.

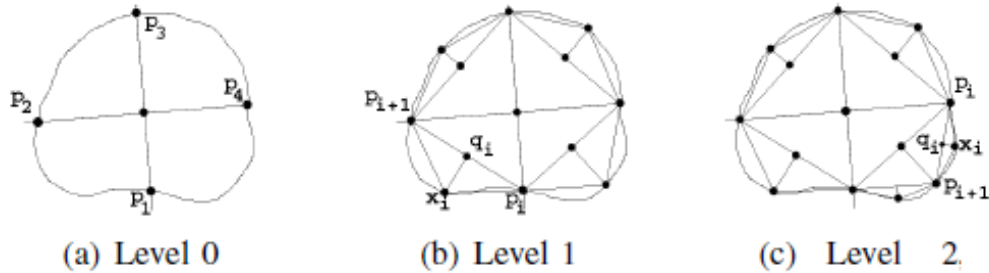


Figure 3.2. Generating optimal correspondences in different resolutions, image from [7].

The same research group presented another method in [8] based on a non-linear regularized framework of point correspondences using TPS. The prostate contour points were at first represented by shape-contexts, and then the Bhattacharyya distance between the shape representations was used to find the optimal correspondences between both images. The main disadvantage of this work is that it was again validated in 2D only, which would limit its application in practice. Moreover, similarly to their previous work, the user had to choose a pair of 2D slices that were assumed to correspond to each other, and then manually delineate the prostate on both slices.

In some studies, the identification of landmark was done manually as in [9] who proposed a non-rigid registration method between US/MRI for prostate laser-based focal therapy. Their method was based on TPS-Robust Point Matching (RPM), which, as its name indicates, required manual identification of landmarks on both modalities. An ICP algorithm was applied at first, and then TPS-RPM was performed in order to detect the local deformations in the image. A preliminary evaluation on three patient datasets gave rather encouraging results with a mean residual error of 1.18 ± 0.32 mm.

Others like [10] proposed a new method to segment the prostate on TRUS images by deforming a patient-specific mesh of the prostate, built from the MRI, to TRUS image. A first step however consisted in segmenting the MRI, by warping a mean shape of the prostate on a manually segmented point cloud, in order to construct a patient-specific mesh that would be used as a template for segmenting the TRUS image. Anatomical mapping between the patient specific mesh and the mean mesh allowed the constructing of an image appearance model for the prostate in the TRUS image. This appearance model, along with shape and volume priors extracted from the MR surface, was used to guide the non-rigid registration between MR and TRUS images.

The determination of the transformation that aligns both images was driven by the detection of feature points. Finally, a biomechanical model was used to interpolate the surface deformations to the whole volume, resulting in dense MR/TRUS correspondences, as illustrated in figure 3.3. Satisfying results were obtained following their proposed registration method with a mean error value of 2 mm.

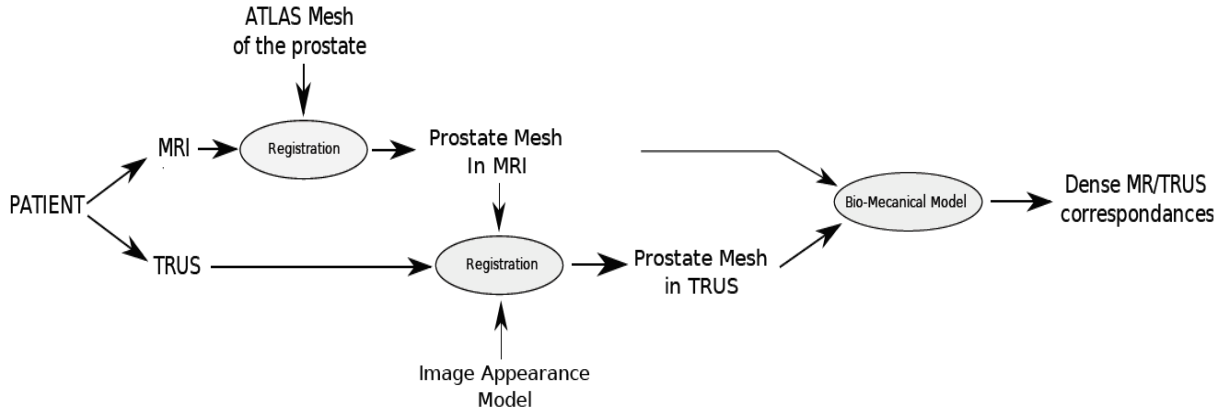


Figure 3.3. Overview of the method including MRI segmentation, TRUS segmentation and MRI/TRUS fusion, image from [10].

[11] used a Statistical Deformation Modeling (SDM) from a training clinical set of semi-automatically segmented TRUS/MR images. An RPM framework was adapted in order to perform a PCA that non-rigidly aligns the two modalities. A study by [12] was focused on non-rigid registration between TRUS and MR images for focal prostate brachytherapy. Firstly, the prostate was manually segmented on the MRI. The resulting 3D point cloud and the MR volume were then interpolated to match TRUS resolution. Subsequently, the resulting contours were projected onto TRUS to serve as an initial estimation. Manual interaction was again needed; the user had to click on the center of the prostate on the first TRUS slice, then the projected contours were also edited manually in order to match the prostate shape on the TRUS image. Afterwards, a rigid registration based on ICP was applied and followed by a non-rigid registration using the 3D shape-context descriptor in order to capture local shape around each point of prostate contours. The shape-context descriptor, proposed by [13], is a spherical neighborhood centered on a given point p . The support region is divided into bins by equally spaced boundaries in the azimuth $(\varphi_0 \dots \varphi_f)$ and elevation $(\theta_0 \dots \theta_k)$ dimensions and logarithmically spaced boundaries along the radial dimension $(R_0 \dots R_L)$, as shown in figure 3.4. Finally, the point pairs matched across modalities were warped using B-splines, resulting in an average registration error of 2.56 mm.

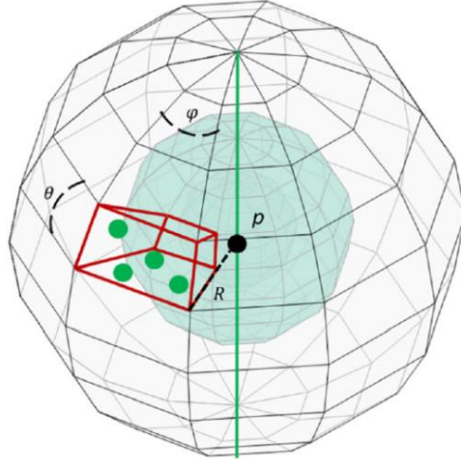


Figure 3.4. The 3D shape-context spherical neighborhood centered on p . In red, a sample bin containing 4 points is highlighted, image from [12].

3.1.3. Intensity-based registration methods:

Intensity-based methods are based on measurements computed directly from pixel intensity without the need for landmark identification or segmentation. A model-based registration method which combined Finite Element Analysis (FEA) with Statistical Shape Modeling (SSM), in order to generate a deformable model of the prostate motion, was presented in [14]. Building this statistical biomechanical model however was computationally intensive and required manually segmented MRI training data provided by biomechanical simulations of the motion of a patient-specific FEM, derived from MRI. The SMM was then registered to TRUS using an intensity-based feature representing an estimate of normal vector at the surface of the prostate. Evaluating their method resulted in an average RMS TRE of 2.66 mm.

A study in [15] rigidly registered 2D US and 3D MR images in order to build a surgical navigation module for prostate brachytherapy. The boundary features were extracted from the US image at first using morphological gradient filter. An electromagnetic localizer was used as a tracking system to provide the orientation and position of the US probe. Then, the US images were transferred into the tracking coordinate system using 3D US spatial calibration. Concerning the registration method itself, it was a two-step process. A first manual US/MRI registration was performed and followed by a mutual information-based registration. Once the transformation is estimated, the patient was aligned with the MR images using the tracking system. Finally, and during the intervention, 2D US images were acquired and then registered to the MRI. The TRE value following their method was of 2.52 ± 0.46 mm.

Others like [16] used the metric MIND, introduced by [17], to non-rigidly register TRUS/MRI for prostate guided biopsy. They proposed a duality-based convex optimization method that could detect the deformation and align the two MIND descriptors. However, their method required a manual initialization where 3 corresponding landmarks needed to be manually placed in the two images in order to generate a rigid transformation as an initial alignment. Their final registration gave an average RMS TRE of 1.93 ± 0.73 mm.

[18] pioneered a new approach for registering US and MR images. However, their method was dedicated to image-guided neurosurgery applications only. The motivation behind their work was to overcome the very different nature of the US and MRI modalities. In fact, the US images are usually called “gradient images”, considering that these images are basically concerned with the interfaces between different structures. The US echo amplitude is proportional to the difference between acoustical impedances caused by successive tissue layers. Therefore, ideally, the US intensity should be at its highest at the interfaces between different tissues and zero within the same tissue. However, this is not really the case since US reflections may take place within the same tissue as well due to small inhomogeneities. Therefore, there are important interference patterns between the ingoing and outgoing pulsed waves, resulting in speckle. Consequently, homogeneous regions appear in the US with nonzero mean intensity. Since these reflections are almost invisible in the MRI, they need to be taken into account when registering the MRI with the US. Hence, the authors suggested correlating the US intensity not only with the MRI intensity, but also with its gradient magnitude. However, a rough manual initialization of the transformation was required, and the registration was limited to rigid transformations only.

[19] extended the work of [18] to include non-rigid transformations. They called their similarity measure Linear Correlation of Linear Combination (LC^2) where they correlate the US intensity with a linear combination of signals extracted from the MRI; intensity and gradient. The LC^2 was computed on 2D US slices rather than a 3D compounded volume. Their method was evaluated on 14 publicly available datasets for brain images, and then the performance was compared to other publications using the same datasets. The first rigid registration gave almost the same FRE as some of the publications. The deformable registration that follows the rigid registration step improved the FRE in a few, but not all, of the cases since the images did not contain important deformations. However, the mean FRE value for all patients was bigger for the non-rigid

registration; where it was of 2.52 ± 0.87 mm after the rigid registration and 2.64 ± 0.9 mm after the non-rigid registration step. One year later, the same group extended their previous work to include 3D volumes instead of 2D US slices [20]. This approach gave slightly better results than the 2D approach they proposed earlier with a mean FRE value of 2.49 ± 0.84 mm.

Therefore, to the best of our knowledge, most US/MRI registration methods dedicated to prostate biopsy or brachytherapy procedures required a manual step including prostate segmentation or identification of landmarks. This step is time consuming and subject to inaccuracies depending on the experience of the user. Some methods in the literature were focused on intensity-based registration techniques. However, these methods also required some manual interaction to initialize the registration process or were limited to rigid transformations only.

3.2. Proposed US/MRI registration approach:

We propose a fully automatic intensity-based non-rigid registration method between US and MR images for prostate brachytherapy. The proposed approach has the potential of being also used in prostate biopsy procedures, where the fusion of US with MRI is necessary as well. Our methodology does not require any manual initialization, segmentation or identification of landmarks. The global workflow of the proposed intra-operative registration methodology is illustrated in figure 3.5.

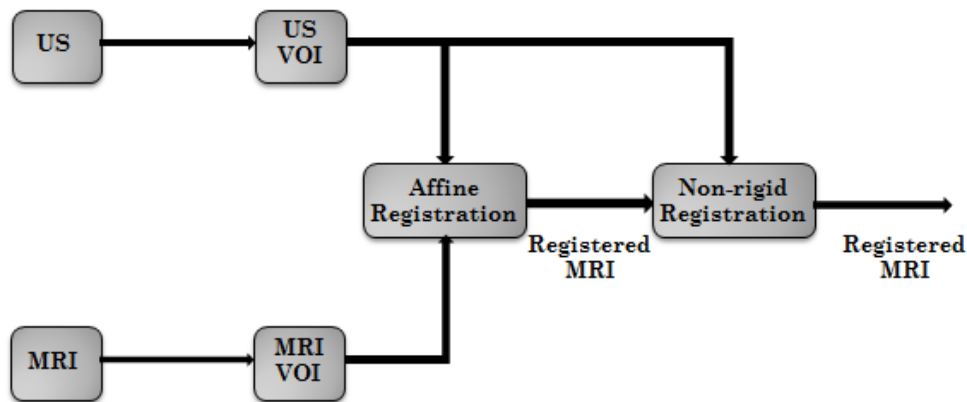


Figure 3.5. Global workflow of the proposed US/MRI registration method.

As illustrated in figure 3.5, the registration is done in two steps; a first affine registration followed by a second non-rigid registration phase. For both registration steps, LC^2 is used as a

similarity measure. LC^2 was only explored in neurosurgery applications, but in this work we will adapt it to being used in prostate brachytherapy procedures where important deformations may occur. In order to improve the robustness of the proposed method as well as avoid local minima, a multi-resolution approach is implemented. Moreover, both registration steps are constrained solely to VOIs, which were determined automatically around the prostate, in order to improve the computational efficiency of the method.

3.2.1. Optional preprocessing:

In prostate brachytherapy, the insertion of the radioactive sources is done via needles that enter through the perineum of the patient using a grid fixed on the TRUS. This grid is visualized on the TRUS image as illustrated in figure 3.6. This is the case for most of the systems used for US acquisitions. However, for some US systems, raw images can be acquired where the grid is not visualized on the TRUS image, and therefore there would be no need for this preprocessing step. The preprocessing step consisted in removing the grid from the US image since it might affect the registration process, considering that an intensity-based approach is used in this work. In order to remove the grid without affecting the rest of the image, mainly to preserve the edges, a median filter was applied on the TRUS volume only in positions of the grid. Since the spacing of the grid is known (5 mm), this preprocessing step can be done automatically by simply detecting the first point of the grid (A: 5.5 in the top left corner). Other textual elements might be automatically removed from the image as well, knowing their positions in the TRUS image. The result of this preprocessing step is illustrated in figure 3.7.



Figure 3.6. TRUS image containing the grid.

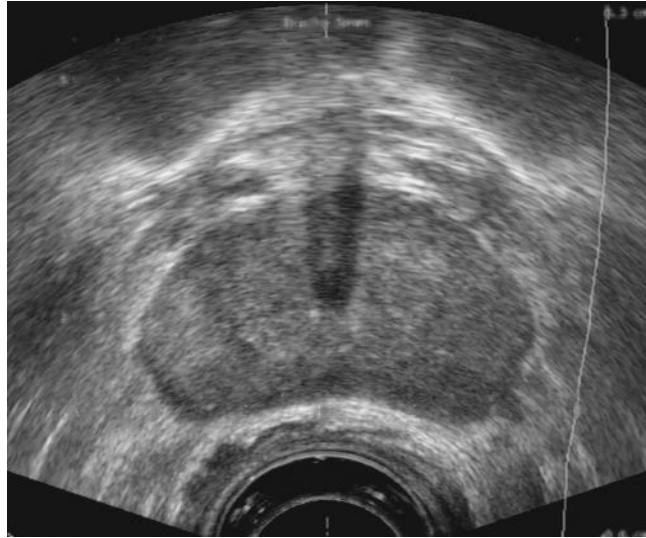


Figure 3.7. TRUS image after the preprocessing.

Once the grid is removed from the image, the VOIs can be determined automatically as described in the following paragraph.

3.2.2. VOIs determination:

A VOI around the prostate is defined automatically on both modalities. Concerning the MR image, the same prostate VOI that was used for the non-rigid registration step in the pre-operative phase is used for the intra-operative registration as well. Since the transformation that aligns the CT and MR images was determined in the pre-operative phase, the prostate VOI on the CT is projected onto the MRI, who is in alignment with the CT, as illustrated in figure 3.8.

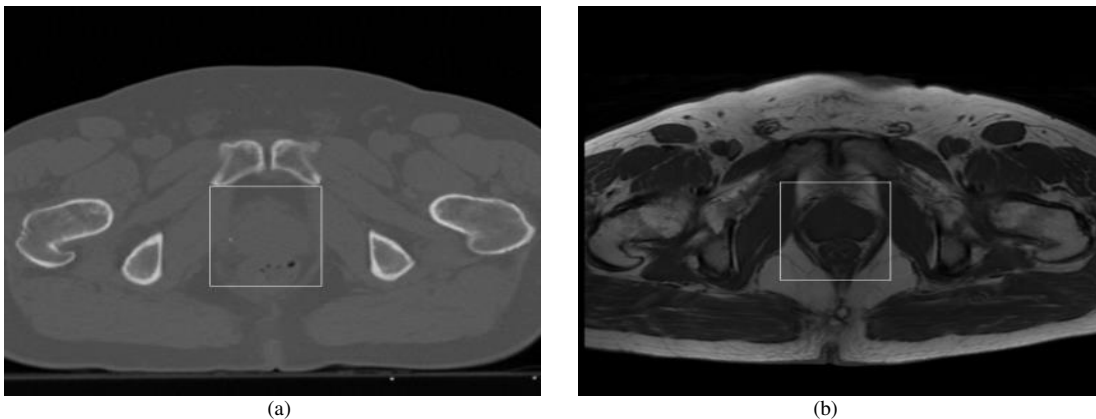


Figure 3.8. Prostate VOI, (a) on the CT, and (b) on the MRI.

Concerning the VOI used for the US image, its determination is done in several steps. At first the middle slice of the US volume is extracted. Since the US acquisition is done from the base to the

apex of the prostate, the whole volume of the prostate is usually visualized on the middle slice. Once the US slice is extracted, prostate contours are automatically highlighted on this 2D image, and then a bounding box is drawn around these contours, defining the prostate ROI. Finally, the ROIs from all the slices are put together to form the VOI that would be used for the registration.

Concerning the extraction of prostate boundaries from the 2D US image, it is done automatically using the Radial Bas-Relief (RBR) method [21]. RBR is a variant of bas-relief method which consists in superimposing the original image onto the negative image, slightly out of register, resulting in an image that looks like a low-relief sculpture, as shown in figure 3.9, hence the name bas-relief.

This technique can be described as follows:

$$b(x, y) = a(x, y) + 255 - a(x + i, y) \quad (3)$$

where $b(x, y)$ is the resulting image, $a(x, y)$ is the original image, and i is the offset along the x axis.

However, the work done by [21] showed that the basic bas-relief method can only highlight the part of the prostate boundary that is perpendicular to the offset direction, as shown in figure 3.9(b). Therefore, and in order to detect all parts of the prostate boundary, the authors proposed making the offset in every direction, radially from the center of the image, hence the name RBR. The difference in defining the offset between both techniques is illustrated in figure 3.10.

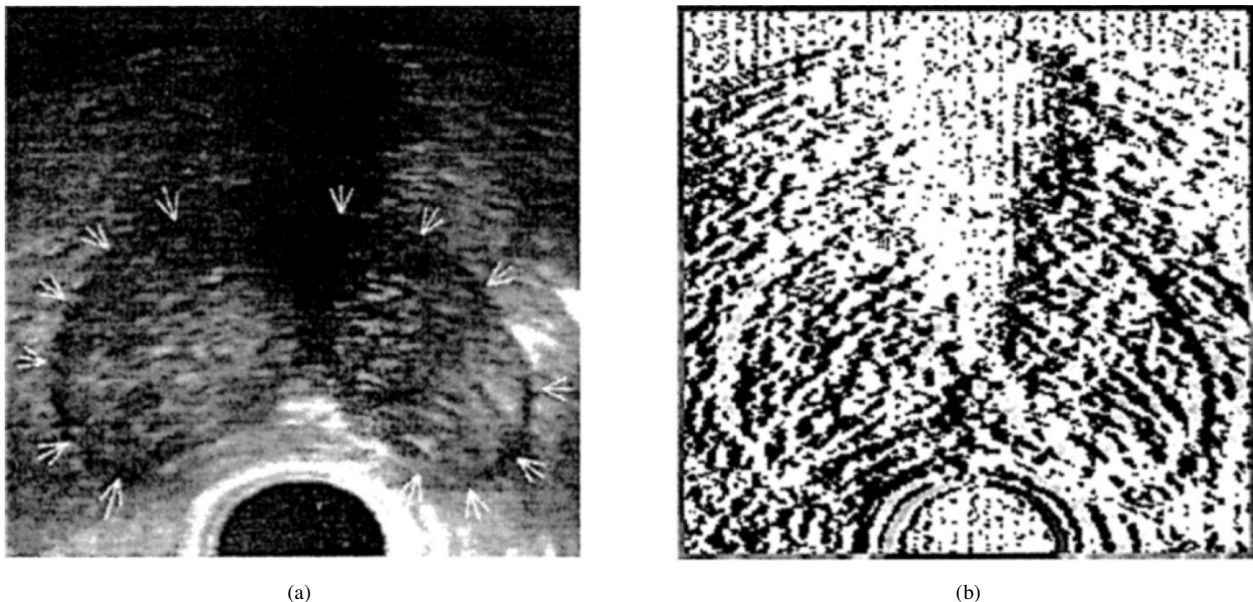


Figure 3.9. Bas-relief, (a) original image, with prostate boundaries marked out by arrows, (b) result of bas-relief, offset = 3 pixels to the right.

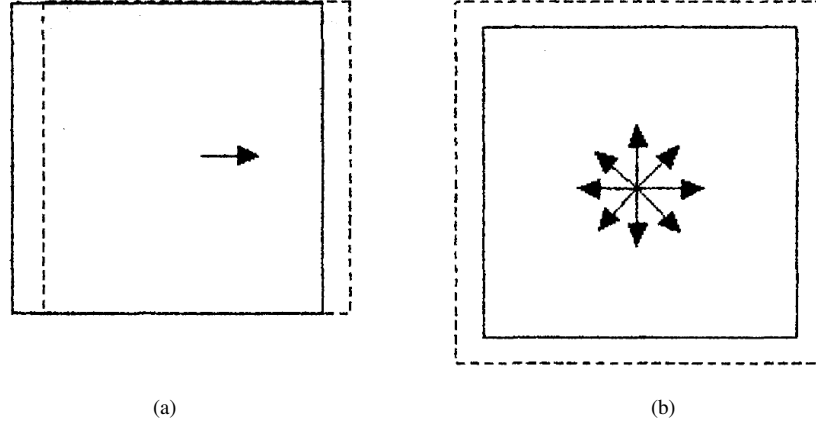


Figure 3.10. Types of offsets. (a) bas-relief method: one directional offset, (b) RBR method: radial (multi-directional) offset.

Prostate contours can be highlighted and eventually extracted using RBR following several steps: intensity normalization, applying RBR (invert, enlarge and add back), binary processing (threshold, dilate and erode), and finally connected-component labeling.

Starting from the middle slice of the US volume, shown in figure 3.7, the image intensity distribution (histogram) is firstly normalized. Since the next step of the method is to invert the original image, simply moving the histogram downwards to make it start from zero can give the best contrast between the original and the inverted image. The normalization can be done by only subtracting the minimum intensity value:

$$b(x, y) = a(x, y) - \min(a(x, y)) \quad (4)$$

where $\min(a(x, y))$ is the minimum pixel intensity in the original image a .

Subsequently, the normalized image is inverted, resulting in an image whose intensity and contrast are negative, as illustrated in figure 3.11(a). Then, instead of applying the offset in one direction, the image is enlarged with a scale ($k = 1.06$) in order to get an omni-radial-direction offset. The enlarge scale k is determined in a way that gives an offset of around 10-15 pixels on the image border, which was found to give the best results, according to [21]. For a given image size of 512*435 pixels, 106% enlargement is equivalent to an offset of 15 and 13 pixels on the x and y axis, respectively. Finally, this enlarged negative image is added to the normalized one, registered at the center, giving the result of the RBR method, illustrated in figure 3.11(b). This can be achieved by applying the following equation:

$$c(x, y) = b(x, y) + 255 - b(kx, ky) \quad (5)$$

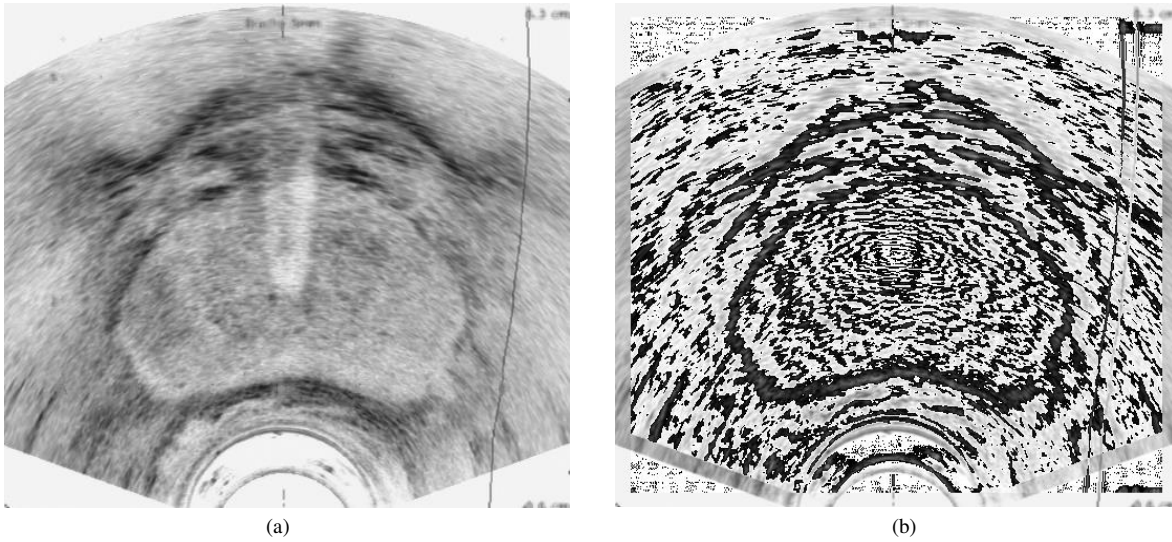


Figure 3.11. (a) The inverted image, (b) the result of RBR.

Further processing is then applied on the result of RBR in order to smooth the image. The image is at first thresholded, using Otsu's automatic thresholding method, and then some morphological transformations (dilation and erosion) are applied in order to smooth the prostate boundaries. Figure 3.12 shows the binary image before (3.12(a)) and after (3.12(b)) the smoothing.

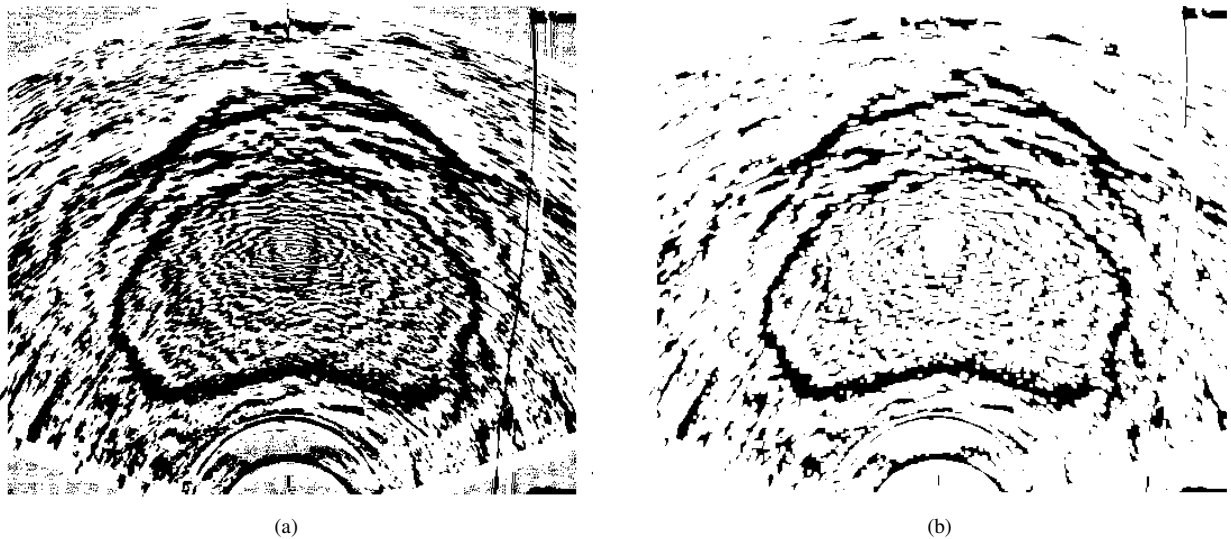


Figure 3.12. RBR image, (a) after thresholding, (b) after boundaries smoothing.

The final step in extracting prostate boundaries involved inverting the smoothed image, shown in 3.12(b), in order to invert boundaries to foreground (white on a black background), as illustrated in figure 3.13(a). Then, a connected-component labeling algorithm is applied to retrieve contours and identify different labels in the image. Subsequently, the surface of each label is calculated, allowing the detection of prostate boundaries, identified by having the biggest surface.

The prostate boundaries are shown in figure 3.13(b).

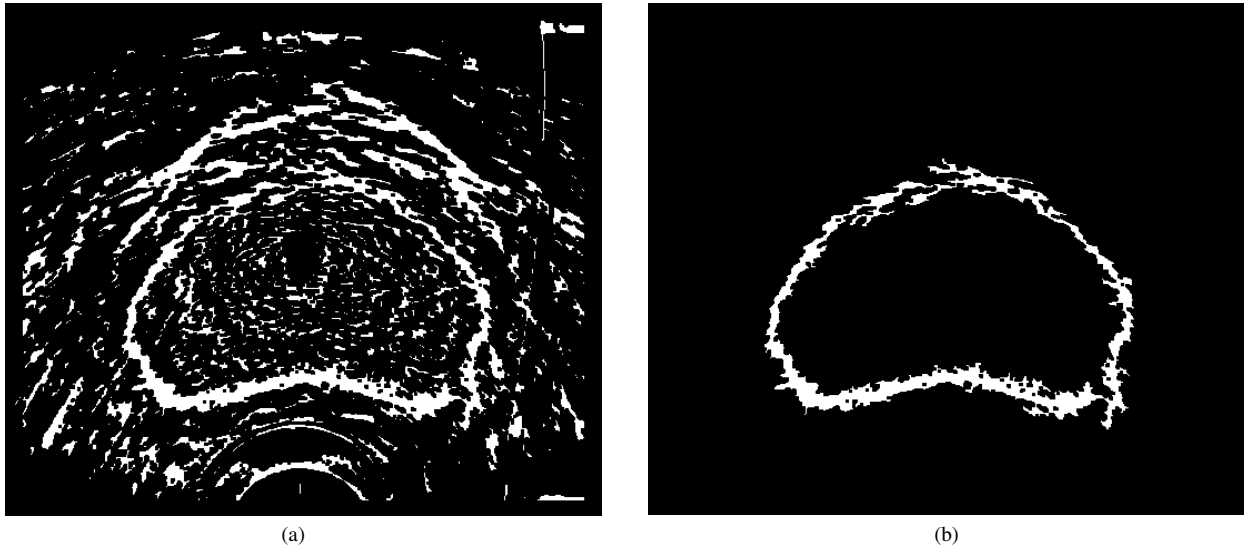


Figure 3.13. (a) Inverted image, (b) prostate boundaries.

A bounding box is then determined around the prostate boundaries, as shown in figure 3.14, defining the prostate VOI on the US volume.

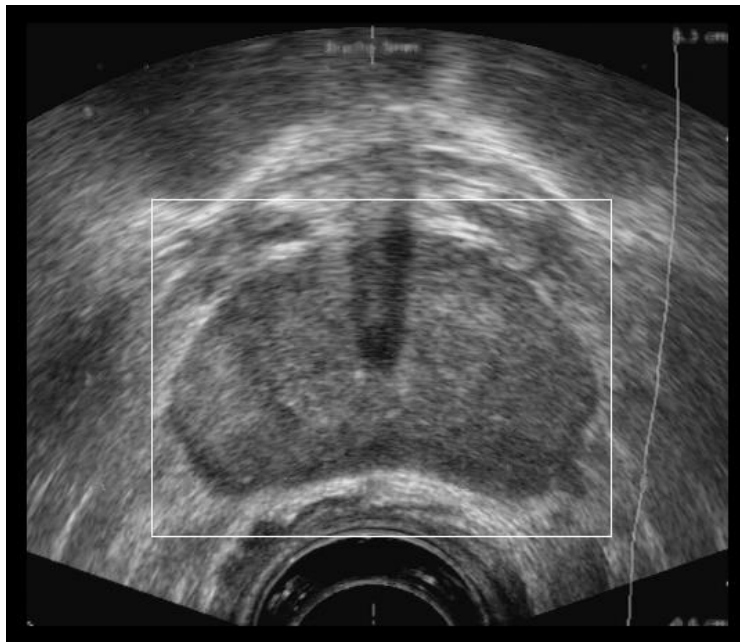


Figure 3.14. Prostate VOI on the US.

These VOIs, which were determined automatically, would be therefore used to constrain the two-step registration process.

3.2.3. Registration:

An intensity-based registration is used for the intra-operative registration between MR and TRUS images. The main components of the proposed registration method are described in the following paragraphs.

Similarity measure:

The similarity measure used for both of the intra-operative registration steps is the LC^2 , proposed by [19]. LC^2 consists in correlating the US intensity not only with the MRI intensity, but also with its gradient magnitude. Figure 3.15 shows US and MR images, where some regions depict a high correspondence between the US intensity and the MR intensity, while some other regions show a high correspondence between the US intensity and the MR gradient.

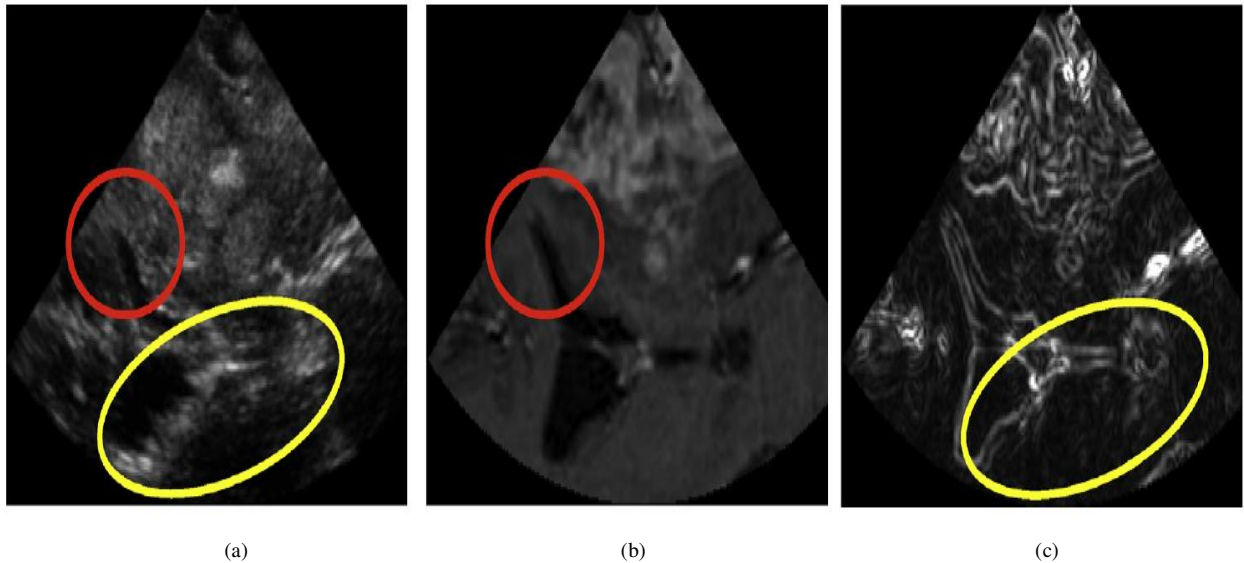


Figure 3.15. LC^2 . (a) US, (b) MRI and (c) MRI gradient. In red, regions where the US intensity is correlated with the MRI intensity, and in yellow, regions where the US intensity is correlated with the MRI gradient, image from [21].

LC^2 can be considered as a variant of Correlation Ratio (CR); the transformation parameters can be therefore estimated in a way that minimizes the following cost function:

$$CR(T, f) = \sum_{x_i} \left\| I(x_i) - f(J(T(x_i))) \right\|^2 \quad (6)$$

where x_i is a pixel in the image, I is the fixed image, J is the floating image, T is the transformation that aligns the two images, and f is a mapping function which estimates the

intensities of the fixed image from the floating image. In the case of LC^2 , the mapping function is defined to be a linear combination of signals extracted from the MRI; the intensity and the gradient. For a pixel intensity in the US image, the relative contributions of MRI intensity values and gradient magnitudes are unknown. Therefore, both the transformed MRI intensities and gradients were integrated in a correlation framework with US intensities, through the mapping function $f(x_i)$ which can be estimated as follows:

$$f(x_i) = \alpha p_i + \beta g_i + \gamma \quad (7)$$

where $p_i = p(T(x_i))$ is the MRI intensity of the pixel x_i , $g_i = g(T(x_i)) = |\nabla p_i|$ is the MRI gradient magnitude, and $y_i = \{\alpha, \beta, \gamma\}$ are the unknown parameters which determine the contribution of MRI intensity and gradient.

The local CR is computed for each pixel x_i in the US image considering a neighborhood $\Omega(x_i)$ of m pixels centered on that pixel. One problem that arises when calculating such a measure is that the two images do not overlap in some of the US regions which do not contain any structural information (shadow regions). Therefore the cost function is modified to penalize such regions by introducing the variance of the US image, as done in [18]. This measure can be therefore written as follows:

$$CR(T, f) = \frac{\sum_{x_i \in \Omega} \|U(x_i) - My_i\|^2}{|\Omega| \sum_{x_i \in \Omega} \text{var}(U(x_i))} \quad (8)$$

where $U(x_i)$ is the US intensity of the pixel x_i , and M is a matrix that can be given by:

$$M = \begin{pmatrix} p_1 & g_1 & 1 \\ \vdots & \vdots & \vdots \\ p_m & g_m & 1 \end{pmatrix} \quad (9)$$

Therefore, the parameters y_i can be estimated for each pixel x_i by minimizing the difference between the US intensity and the mapping function; $\|U(x_i) - My_i\|^2$.

This can be solved using the least squares with the pseudo inverse of the matrix M as follows:

$$\begin{pmatrix} \alpha \\ \beta \\ \gamma \end{pmatrix} = (M^T M)^{-1} M^T \begin{pmatrix} u_1 \\ \vdots \\ u_m \end{pmatrix} \quad (10)$$

Once the parameters are estimated, they are then inserted in the equation (8) to determine the local CR . The minimization of (8) may be performed by travelling through the minima of $CR(T, f)$ or through the maxima of the criterion given by the equation:

$$LC^2_{local} = 1 - \frac{\sum_{x_i \in \Omega} \|U(x_i) - My_i\|^2}{|\Omega| \sum_{x_i \in \Omega} \text{var}(U(x_i))} \quad (11)$$

where the local LC^2 reaches its maximum when $CR(T, f)$ is minimal.

Afterwards, the global LC^2 is computed using the weighted average of the local measures calculated for each pixel in the image. The weights are the local standard deviation of the US image in the neighborhood centered on the given pixel.

$$LC^2_{global} = \frac{\sum_i LC^2_{local}(x_i) * \sigma_i}{\sum_i \sigma_i} \quad (12)$$

Optimizer:

Considering the equation (8), an analytic derivation of LC^2 is difficult to compute because of the least squares fitting that is calculated for each pixel in the US image. Therefore, an optimizer that does not require derivatives of the cost function is considered to determine the transformation parameters which align the two images. Several optimizers were tested, such as one-plus-one evolutionary, Powell and Amoeba (Nelder-Mead downhill simplex). Although Amoeba optimizer might be slow, it was proven to be the most robust and easy to implement algorithm for unconstrained nonlinear optimization. Moreover, this optimizer has the advantage of avoiding local maxima because, at each iteration, the simplex is initialized with the best solution obtained in the previous iteration [22]. For this work, Amoeba gave the best results, for both registration steps, whereas other optimizers got stuck on local maxima.

Amoeba can be used for the maximization (or minimization) of a mathematical cost function of n variables using a simplex (polytope of $n+1$ vertices in n dimensions). At first, the cost function is evaluated at each of the $(n+1)$ vertices of the simplex, and then the worst vertex (the one with the lowest value when searching for a maximum) is replaced by another point. This replacement is done using three operations; reflection (reflecting a corner of the simplex about the opposite edge), contraction (shrinking the entire simplex) and expansion (stretching the entire simplex). The worst point is usually replaced with a point reflected through the centroid of the remaining n points. If the new point is better than the best current one, then the simplex is stretched along this line. On the other hand, if the new point is worse than the current one, then the simplex is shrunk towards a better point and so on. Figure 3.16 illustrates the different possible outcomes of this optimization method.

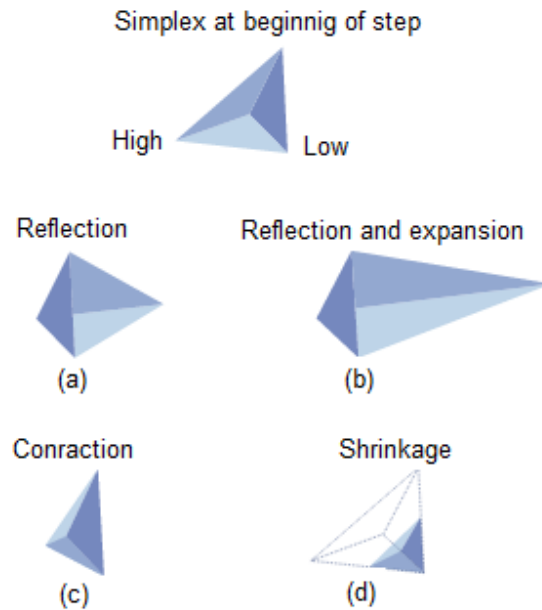


Figure 3.16. Simplex method, figure from MIT OpenCourseWare.

The initial size of the simplex, which has an impact on the convergence, can be defined by the user. The optimization process is terminated when the maximum number of iterations, set by the user, is reached. Another option to define convergence can be considered by setting tolerances on either the function values (difference between the current and the best value) or on the optimizers' parameters (difference between the current and the best parameters).

Transformation:

Similarly to the pre-operative registration, the intra-operative registration is done in two steps. A first affine registration step is applied to globally align the two images and then used as initialization for the second B-spline-based non-rigid registration step. A pre-registration step however consisted in superimposing the VOIs from the two images.

Since prostate deformations are more important during the intervention (due to probe pressure and needles insertion), a multi-resolution approach is implemented where registration is performed from low to high resolution. The advantage of this approach is avoiding local maxima as well as speeding up the registration process. At low resolutions, both images are resampled at $1/2$, $1/4$, $1/8$... number of voxels along each dimension, depending on the number of levels. Three levels were considered for this work, as shown in figure 3.17, since this offers a good compromise between accuracy and computational efficiency. Subsequently, the transformation is estimated at first on the coarsest level and then used as initialization for the next level and so on.

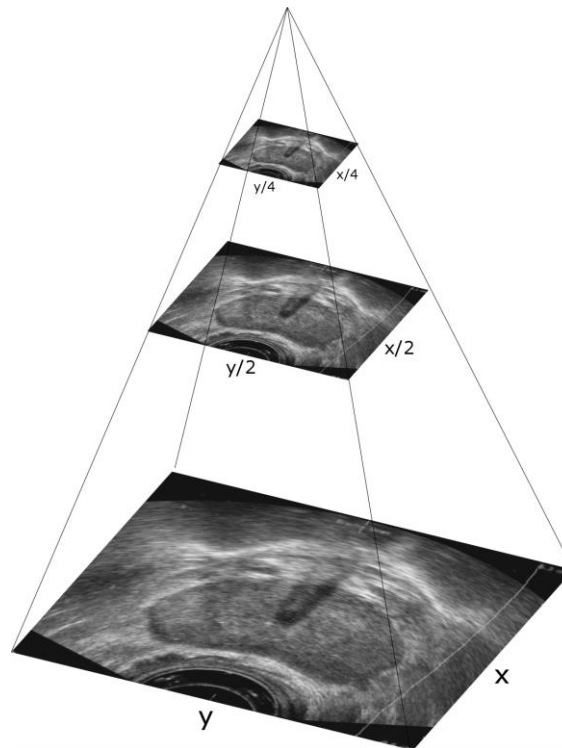


Figure 3.17. Multi-resolution approach on 3 levels.

The number of control points used for B-spline was changed from one level to another as well. For the coarsest level, six control points were used, which is equivalent to a number of degrees of

freedom equal to $6^3 \times 3 = 648$ DoF. As for the second level, seven control points were used, resulting in 1029 DoF. Finally, and for the finest level, nine control points, which is equivalent to 2187 DoF, gave the best results.

Interpolation:

Once the optimal transformation that aligns the two images is determined, it is applied to the floating image (in our case, the MRI). An interpolator is then used in order to calculate floating image intensities at non-rigid positions. As previously explained in chapter 2 section 2.2.2., the inverse mapping is used to resample the floating image onto the fixed image grid. Similarly to the pre-operative registration, a tri-linear interpolator is used since it offers a good compromise between accuracy and computational efficiency.

3.3. Implementation:

Similarly to the pre-operative registration, the intra-operative registration was implemented in C++ using the Insight Segmentation and Registration Toolkit (ITK). Images were read using the DICOM image reader integrated in the Visualization Toolkit (VTK). For the VOIs determination, Open source Computer Vision (OpenCV) was used.

A software called BrachyLive was developed in order to automate the procedure of the registration. This software was focused on the intra-operative phase of prostate procedures (biopsy and brachytherapy). It aims to accurately register US with MR images in order to improve the visualization and navigation during the intervention to correctly insert the radioactive sources in their pre-planned positions as well as perform an accurate targeted biopsy.

Regarding the computational efficiency, the proposed two-step registration method was completed on an average of 2.75 ± 0.25 hours, on an Intel® Core™ i7-3840QM CPU @ 2.80 GHz processor.

Considering that this registration methodology is performed in the intraoperative phase, during the intervention, it needs to be compatible with the time constraints in a clinical workflow. Therefore, a solution on Graphics Processing Unit (GPU) will be developed.

Since the LC^2 metric is calculated on each pixel of the image regardless of the results on other pixels, its calculation can be perfectly parallelized and an approach using GPU has the potential of improving the computational efficiency.

3.3.1. GPUs:

GPUs are employed to accelerate numerical computing by performing multiple parallel executions using a large number of threads. Contrarily to Central Processing Units (CPUs), GPUs do not need a large cache since they can dedicate more transistors to data processing rather than data caching and flow control, which is the case for CPUs. The main differences in parallelism between CPUs and GPUs are listed in the table 3.1.

Table 3.1. Parallelism in CPUs and GPUs.

CPUs (task parallelism)	GPUs (data parallelism)
Multiple tasks map to multiple threads	SIMD (Single Instruction Multiple Data)
Tasks run different instructions	Same instruction on different data
10s of threads run on 10s of cores	10000s of threads run on 1000s of cores
Each thread managed and scheduled explicitly	Threads are managed and scheduled by hardware
Each thread programmed individually	Programming is done for batches of threads

A GPU is organized in several streaming multiprocessors (SMs). Each SM is composed of several stream processors (SPs), also called thread processors, as illustrated in figure 3.18. SMs can therefore handle several threads, organized in blocks, with each thread representing a basic data element to be processed. Each thread has private local memory, while each block has shared memory visible to all threads of that block. Moreover, all threads have access to a global memory, which is bigger than both the private and the shared memory.

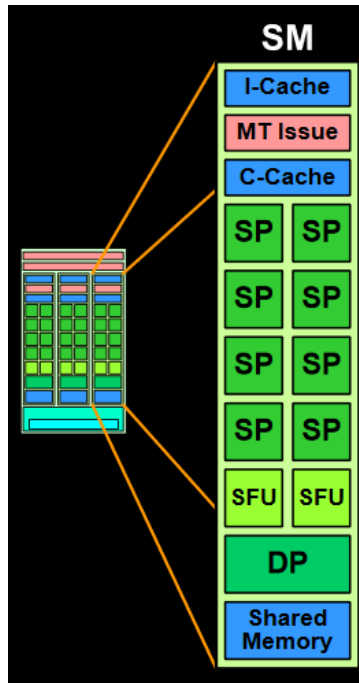


Figure 3.18. Streaming multiprocessor.

As a SIMD device, all threads of a GPU execute the same code, called kernel. Once a kernel is launched, blocks of threads on different SMs are scheduled automatically. Each block is divided into units called warps, representing the smallest executable unit of code.

3.3.2. GPU implementation:

For GPU implementation, the platform Compute Unified Device Architecture (CUDA) can be used. CUDA is a scalable parallel programming model and software environment for parallel computing, with minimal extensions to familiar C/C++ environments. This platform enables dramatic increases in computational efficiency by harnessing the power of GPU.

A CUDA program can be generally viewed as collaboration between CPU and GPU, as illustrated in figure 3.19(a). It is composed of the host code, usually the regular C/C++ code, executed sequentially in the CPU and the device code, mainly the kernel functions, executed on the GPU by many cuda threads simultaneously.

CUDA allows the user to group multiple threads into blocks and further group multiple blocks into grids, where each thread has a different ID, as illustrated in figure 3.19(b).

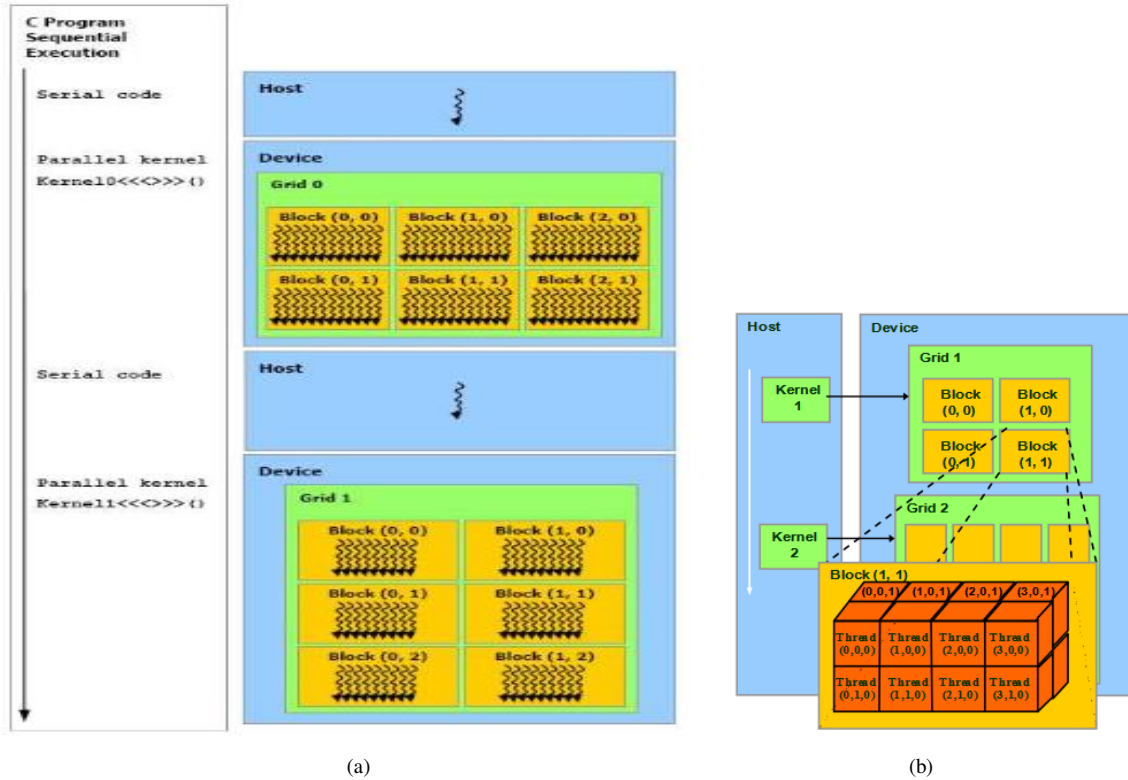


Figure 3.19. (a) Execution of a typical CUDA program, and (b) CUDA thread, block and grid.

A first simulation consisted in registering 2D US and MR images; where only the LC^2 calculation was implemented on GPU and the rest of the registration process was performed on CPU. For a given image of size $\text{dimX} * \text{dimY}$, a block of threads was attributed to each pixel in the image, resulting in a $\text{dimX} * \text{dimY}$ blocks. These blocks of threads represent the neighborhoods centered on each given pixel. Concerning the number of pixels in the neighborhood, a size of $m=361$ pixels was found to give the best results (see section 4.4.2.2.). Therefore, each block contained m threads, where each thread represents a single pixel. For each pixel of the three images (US, MRI, and gradient of the MRI), a neighborhood of m pixels is at first defined around the given pixel. Subsequently, the matrix M is calculated following the equation (9). Then, the parameters y_i can be estimated using the least squares with the pseudo inverse of the matrix M as in the equation (10). These parameters, which are calculated for each pixel in the image, are then inserted in equation (11) to compute the local LC^2 . The computation of local LC^2 is therefore performed on different blocks of threads separately, with the result of each block being completely independent from the other blocks. Finally, and when the local measures are calculated for each pixel in the image, the global LC^2 is computed using the weighted average of the local measures, following the equation (12).

In the case of 2D US and MR images, the calculation of the global LC^2 took 3.23 seconds on CPU, for one iteration of the optimization process. A first non-optimal version on GPU (NVIDIA TITAN X Pascal, containing 3584 cores) completed the same calculation in 80 ms, resulting in a speeding factor of x40. Therefore, by interpolating this factor over the whole registration process, the computational efficiency could be potentially reduced to 3.75 minutes using one GPU. Considering the possibility of using 4 GPUs in a workstation, this calculation time could be therefore reduced to 56 seconds. This first simulation was a non-optimal version of the implementation of LC^2 on GPU; therefore we believe that implementing the whole registration process, and optimizing the code, could improve the computational efficiency by at least a factor of two, resulting in less than 30 seconds which can be compatible with time constraints in a clinical workflow.

3.4. Conclusion:

In this chapter we presented a fully automatic non-rigid registration methodology between US and MR images dedicated to prostate brachytherapy. This method does not require any manual segmentation or identification of landmark. The proposed method is based on a similarity measure called Linear Correlation of Linear Combination (LC^2). LC^2 was used in the literature for neurosurgery applications only. In this work, this measure was adapted for the use in prostate brachytherapy procedures where important deformations may occur. The registration is done in two steps; a first affine registration is used to initialize a second non-rigid registration step. A multi-resolution approach was implemented where registration is performed from low to high resolution. Each registration was constrained to a VOI, defined automatically around the prostate, in order to improve the robustness and the computational efficiency of the approach. The validation of the method, using a prostate phantom at first and then some clinical patient datasets, will be presented in chapter 4.

References:

- [1] Reynier C, Troccaz J, Fournier P, Dusserre A, Gay-Jeune C, Descotes JL, Bolla M, and Giraud JY (2004). "MRI/TRUS data fusion for prostate brachytherapy. Preliminary results". *Medical Physics*. **31(6)**: 1568-75.
- [2] Kruecker J, Xu S, Choyke P, Turkbey B, Pinto P, and Wood B (2008). "Fusion of transrectal ultrasound with pre-acquired MRI for prostate biopsy guidance". *Medicamundi*. **52(1)**: 25-31.
- [3] Narayanan R, Kurhanewicz J, Shinohara K, Crawford ED, Simoneau A, and Suri JS (2009). "MRI-ultrasound registration for targeted prostate biopsy". *Proc. IEEE International Symposium on Biomedical Imaging: From Nano to Macro*. 991-4.
- [4] Moradi M, Janoos F, Fedorov A, Risholm P, Kapur T, Wolfsberger LD, Nguyen PL, Tempany CM, and Wells WM (2012). "Two solutions for registration of Ultrasound to MRI for image-guided prostate interventions". *Proc. IEEE Engineering in Medicine and Biology Society*. 1129-32.
- [5] Sparks R, Bloch BN, Feleppa E, Barratt D, and Madabhushi A (2013). "Fully automatic prostate magnetic resonance imaging and transrectal ultrasound fusion via a probabilistic registration metric". *Proc. SPIE*. **8671**.
- [6] Khallaghi S et al. (2015). "Biomechanically constrained surface registration: application to MR-TRUS fusion for prostate interventions". *IEEE Transactions on Medical Imaging*. **34(11)**: 2404-14.
- [7] Mitra J, Oliver A, Marti R, Llado X, Vilanova JC, and Meriaudeau F (2010). "A thin-plate spline based multimodal prostate registration with optimal correspondences". *Proc. IEEE International Conference on Signal-Image Technology and Internet Based Systems*. 18-22.
- [8] Mitra J, Kato Z, Marti R, Oliver A, Llado X, Sidibé D, Ghose S, Vilanova JC, Comet J, and Meriaudeau F (2012). "A spline-based non-linear diffeomorphism for multimodal prostate registration". *Medical Image Analysis*. **16(6)**: 1259-79.
- [9] Makni N, Toumi I, Puech P, Issa M, Colot O, Mordon S, and Betrouni N (2010). "A non rigid registration and deformation algorithm for ultrasound & MR images to guide prostate cancer therapies". *Proc. IEEE Engineering in Medicine and Biology Society*. 3711-4.
- [10] Martin S, Baumann M, Daanen V, and Troccaz J (2010). "MR prior based automatic segmentation of the prostate in TRUS images for MR/TRUS data fusion". *Proc. IEEE International Symposium on Biomedical Imaging*. 640-3.
- [11] Onfrey JA, Staib LH, Sarkar S, Venkataraman R, and Papademetris X (2015). "Learning nonrigid deformations for constrained point-based registration for image-guided MR-TRUS prostate intervention". *Proc. IEEE International Symposium on Biomedical Imaging*.
- [12] Mayer A, Zholkover A, Portnoy O, Raviv G, Konen E, and Symon Z (2016). "Deformable registration of trans-rectal ultrasound (TRUS) and magnetic resonance imaging (MRI) for focal prostate brachytherapy". *International Journal of Computer Assisted Radiology and Surgery*. **11(6)**: 1015-23.

- [13] Frome A, Huber D, Kolluri R, Bulow T, and Malik J (2004). "Recognizing objects in range data using regional point descriptors". *Computer Vision - ECCV*. **3023**: 224-37.
- [14] Hu Y, Ahmed HU, Allen C, Pendsé D, Sahu M, Emberton M, Hawkes D, and Barratt D (2009). "MR to ultrasound image registration for guiding prostate biopsy and interventions". *Medical Imaging Computing and Computer Assisted Interventions*. **21(1)**: 787-94.
- [15] Zhang S, Jiang S, Yang Z, and Liu R (2015). "2D ultrasound and 3D MR image registration of the prostate for brachytherapy surgical navigation". *Medicine*. **94(40)**.
- [16] Sun Y, Yuan J, Qiu W, Rajchl M, Romagnoli C, and Fenster A (2015). "Three-dimensional nonrigid MR-TRUS registration using dual optimization". *IEEE Transactions on Medical Imaging*. **34(5)**: 1085-95.
- [17] Heinrich MP, Jenkinson M, Bhushan M, Matin T, Gleeson FV, Brady SM, and Schnabel JA (2012). "MIND: Modality independent neighbourhood descriptor for multi-modal deformable registration". *Medical Image Analysis*. **16(7)**: 1423-35.
- [18] Roche A et al. (2001). "Rigid registration of 3D ultrasound with MR images: a new approach combining intensity and gradient information". *IEEE Transactions on Medical Imaging*. **20(10)**: 1038-49.
- [19] Wein W et al. (2013). "Global registration of ultrasound to MRI using the LC2 metric for enabling neurosurgical guidance". *Medical Image Computing and Computer Assisted Interventions*. **8149**: 33-41.
- [20] Fuerst B et al. (2014). "Automatic ultrasound-MRI registration for neurosurgery using the 2D and 3D LC2 metric". *Medical Image Analysis*. **18(8)**: 1312-9.
- [21] Liu YJ et al. (1997). "Computerized prostate boundary estimation of ultrasound images using radial bas-relief method". *Medical & Biological Engineering & Computing*. **35(5)**: 445-54.
- [22] Nelder JA and Mead R (1965). "A simplex method for function minimization". *The Computer Journal*. **7(4)**: 308-13.

Evaluation and Results

In this chapter, the two proposed registration methodologies are validated using both quantitative and qualitative evaluation criteria. Concerning the pre-operative MRI/CT registration, clinical patient datasets are used for validation. As for the intra-operative US/MRI registration, the method is firstly validated on a prostate phantom to evaluate its feasibility and, subsequently, it is validated using clinical patient datasets. At first, the evaluation metrics are presented, and then the results are shown for both registration methods.

4.1. Prostate phantom:

Considering that the prostate anatomical representation in phantom images is much simpler than that of clinical patient datasets (heterogeneous tissues), prostate phantom is used for the preliminary evaluation of the feasibility and the accuracy of the proposed US/MRI registration methodology. This phantom has to model the prostate and mimic its motion; therefore a realistic and deformable phantom is needed. Due to the different nature of the US and MRI images (especially the speckle noise present in the US), two different synthetic phantoms were constructed and tested; one for each modality. Hereafter, the selection of tissue mimicking materials (TMMs) and phantom construction procedure are described for both phantoms.

4.1.1. MRI phantom:

At first, a model representing a 3D mold including an approximation of a prostate geometry is created using Blender (www.blender.org), as shown in figure 4.1(a). This mold is composed of two identical halves, one of which is shown in figure 4.1(b), and the prostate lies in the middle.

4.1. Prostate phantom

Two holes are made at the top, one to pour the TMM into the mold and another one to let the air out and ensure that no air is trapped in the mold.

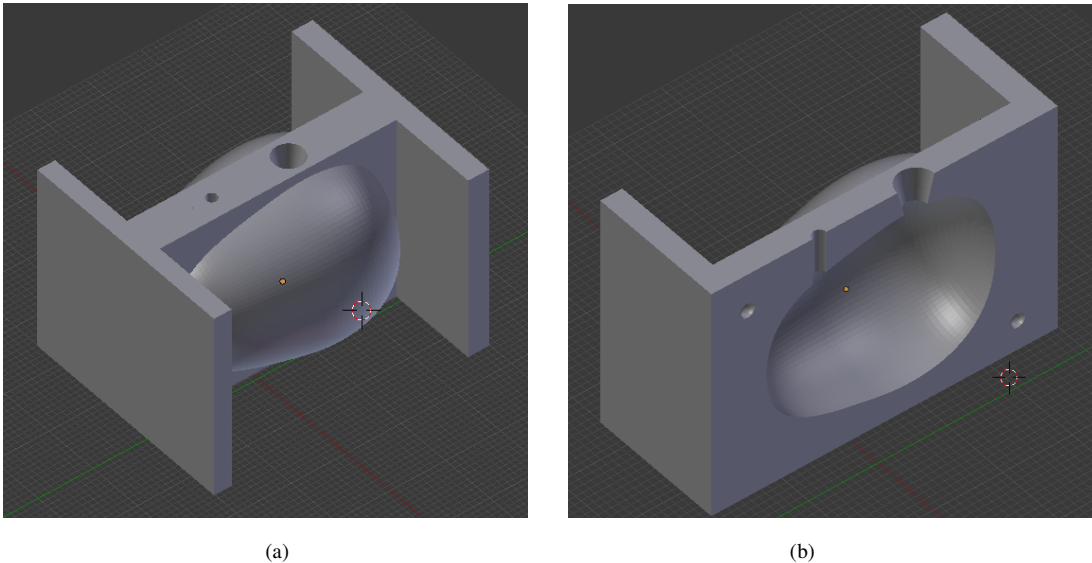


Figure 4.1. Prostate phantom model built using Blender, (a) 3D mold, (b) one half of the mold.

Subsequently, a 3D printer was used to print the mold. As for the selection of the TMM, a mixture of agar and condensed milk is used when constructing the phantom that mimics soft tissues in MRI [1]. This mixture reveals interesting properties since the milk contributes to the elastic character and the agar ensures stiffness and cohesion. Moreover, these TMMs exhibit properties at room temperature which correspond to those of the prostate tissues at body temperature. At first, a mixture of 3% agar mixed with 3% of psyllium was poured into a plastic container, representing the soft tissues surrounding the prostate. The psyllium solution in the mixture is used to provide a better contrast between the prostate and the background. The mixture is stirred to ensure homogeneity and remove any air bubbles from the surface. Afterwards, once the mixture is dry, the prostate is placed on top of the first layer, as illustrated in figure 4.2 where the prostate was colored in blue to distinguish it from the surrounding tissues. For the prostate itself, a mixture of agar and milk was used; where 4% of agar was mixed with 25 ml of condensed milk. This mixture at these percentages was found to give the best results in mimicking soft tissues in MRI, namely, the T1 and T2 relaxation times. Finally, the prostate is covered by filling the plastic container with the agar-psyllium mixture.



Figure 4.2. Prostate MRI phantom model.

An MRI (T1-weighted) acquisition was performed using the platform Neurinfo, situated in the university hospital (CHU) of Rennes (www.neurinfo.org). An axial MR slice of the phantom is shown in figure 4.3.

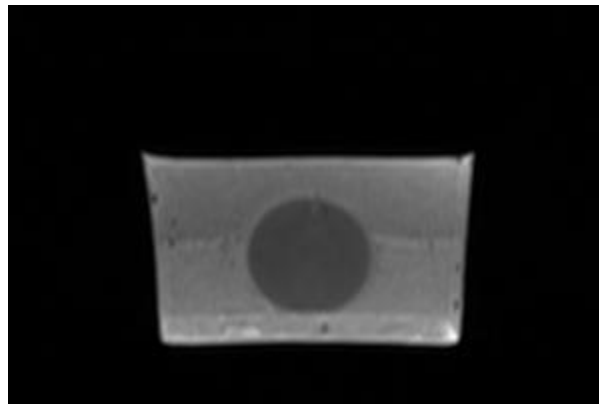


Figure 4.3. MRI (T1) of the prostate phantom.

4.1.2. US phantom:

Considering the different nature between the US and the MR images, namely the speckle noise, a different TMM was used to construct the US phantom. Moreover, the mixture of agar is too fragile for the type of intervention required for the US image, i.e. the insertion of the TRUS probe. A realistic phantom with representative values of acoustic properties, such as propagation

4.1. Prostate phantom

speed and attenuation coefficients, which match those of soft tissues, is required. Therefore, polyvinyl chloride (PVC) was used considering the similarities between PVC and soft tissues [2].

Since the PVC solution is at high temperature, it cannot be poured directly into the previous mold. At first, an approximation of a prostate geometry is created using Blender, and then printed using a 3D printer. This 3D model is then used to fabricate a mold made of plaster, as shown in figure 4.4.

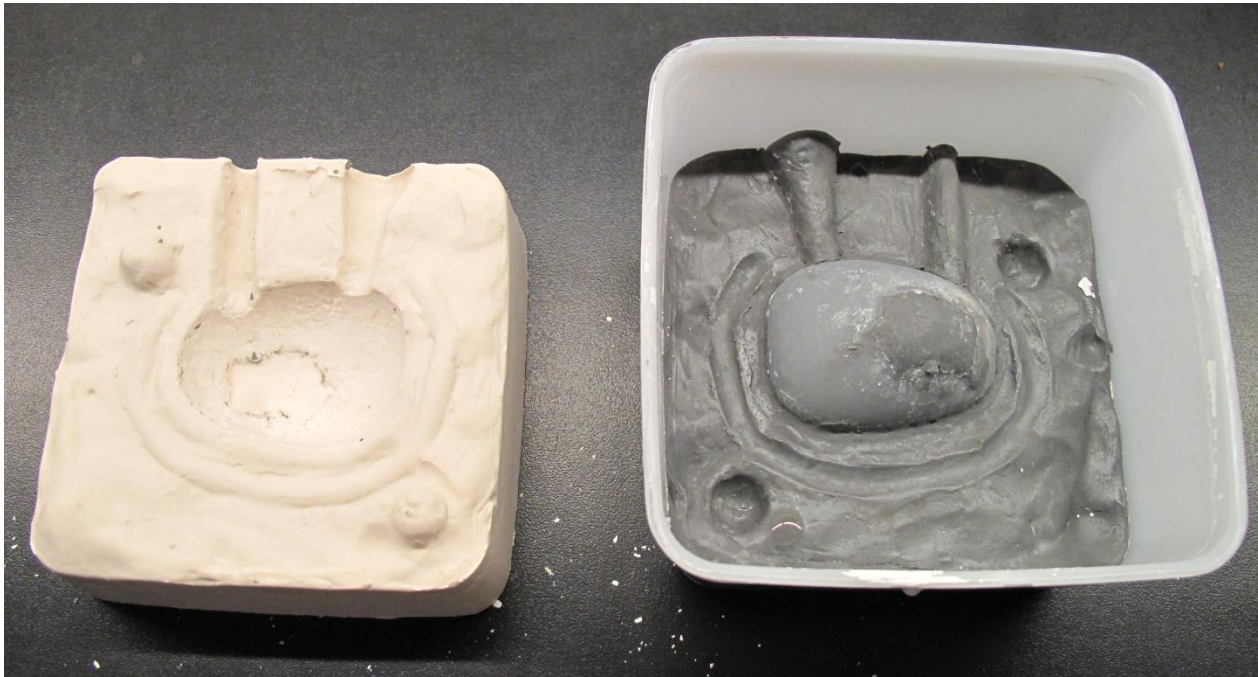


Figure 4.4. The printed prostate phantom model to the right, and the mold made of plaster to the left.

The US phantom was then constructed as follows. A layer of PVC, with a hole representing the rectum and allowing the insertion of the TRUS probe, was poured into a container. The solution was cooled and once it became dry, the prostate was placed on top of the rectum wall. To make the image more realistic, and since the urethra is always visible in US images, a thin tube was inserted through the prostate to represent the urethra. This tube could be filled with water to add some contrast in order to differentiate between the prostate and the urethra. As for the TMM used for the prostate, a mixture of PVC with 1% of psyllium was used. The psyllium was added to the PVC to give some sort of speckle noise, which is typically present in the US images [3]. Figure 4.5 shows the prostate, situated on the layer representing the rectum wall, with a tube representing the urethra.



Figure 4.5. US phantom showing the prostate in yellow, with a tube that goes through it representing the urethra, and the rectum wall in green.

The background representing the surrounding tissues was then added by filling the container with another mixture of PVC with 2% of psyllium. Adding the psyllium to different structures in different percentages provided a better contrast between the prostate and the surrounding tissues. This phantom, after coloring each structure with a different color, is shown in figure 4.6.

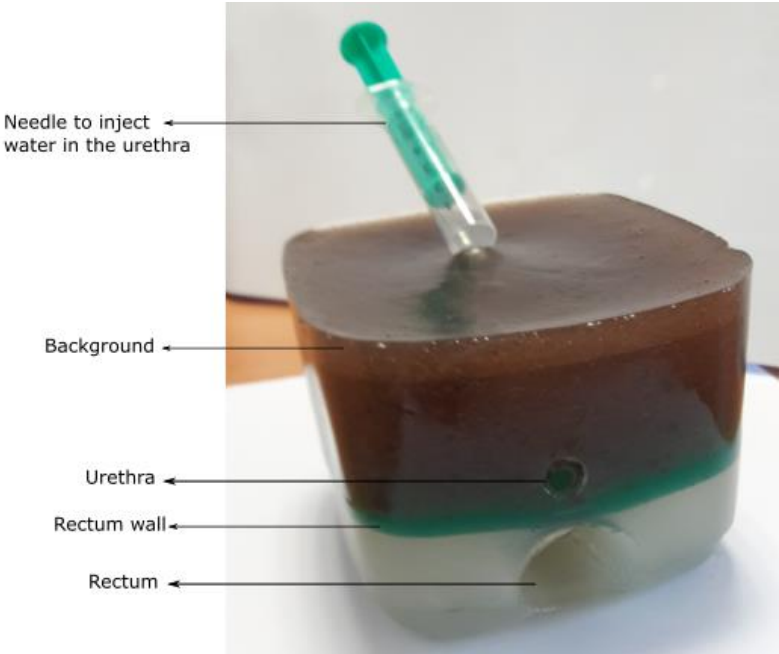


Figure 4.6. US prostate phantom showing two holes representing the rectum and the urethra.

2D US acquisitions were then performed on the Ultrasonix platform available in LaTIM - CHU of Brest using an end-fire TRUS probe. One slice of the US phantom is shown in figure 4.7.



Figure 4.7. US image of the prostate phantom.

As illustrated in the figure 4.7, the US image of the phantom was realistic; containing speckle noise with a good contrast between the prostate and the surrounding tissues. Moreover, the urethra, which is usually visible on the US image, was also visualized in the phantom image.

4.2. Clinical patient datasets:

Both registration methodologies were validated using anonymized datasets of patients undergoing brachytherapy. Patients agreed to the study providing a written consent according to the university hospitals of Brest and Poitiers.

4.2.1. Pre-operative MRI/CT registration:

The MRI/CT registration method was validated using 8 datasets of patients undergoing brachytherapy. For each patient, MR (T1-weighted) and CT pelvic images were pre-operatively acquired with some time interval (MRI and CT were acquired for the diagnosis and the treatment planning, respectively). These images were acquired in different facilities, CHU of Brest and CHU of Poitiers, and using different systems. Detailed dimensions of these image datasets are given in table 4.1.

Table 4.1. Dimensions of MRI/CT datasets of the patients.

	CT	MRI
Patient 1	512*512*150 voxels of 0.78*0.78*2 mm ³	640*640*44 voxels of 0.47*0.47*5.95 mm ³
Patient 2	512*512*171 voxels of 0.89*0.89*2 mm ³	672*672*40 voxels of 0.52*0.52*6 mm ³
Patient 3	512*512*76 voxels of 0.88*0.88*5 mm ³	320*240*100 voxels of 1.31*1.31*3.05 mm ³
Patient 4	512*512*50 voxels of 0.98*0.98*3 mm ³	320*240*50 voxels of 1.25 *1.25*3 mm ³
Patient 5	512*512*120 voxels of 0.82*0.82*2 mm ³	704*704*40 voxels of 0.5*0.5*2 mm ³
Patient 6	512*512*50 voxels of 0.98*0.98*1.5 mm ³	320*320*24 voxels of 0.69*0.69*3 mm ³
Patient 7	512*512*75 voxels of 0.98*0.98*1 mm ³	320*320*24 voxels of 0.69*0.69*3 mm ³
Patient 8	512*512*50 voxels of 0.98*0.98*1.5 mm ³	320*320*24 voxels of 0.69*0.69*3 mm ³

4.2.2. Intra-operative US/MRI registration:

After evaluating the feasibility of the proposed US/MRI registration method using a prostate phantom, the method was validated using three clinical datasets of patients undergoing brachytherapy. For each patient, MR (T1-weighted) images were pre-operatively acquired while the US images were acquired in real-time during the intervention. Concerning the MR images, they are usually acquired in external clinics while the US acquisition was done in the CHU of Brest. Due to the difficulties of recovering the MR images which correspond to the US images of the same patient, only three patient datasets were considered for the validation of the intra-operative registration method. Detailed dimensions of these image datasets are given in table 4.2.

Table 4.2. Dimensions of US/MRI datasets of the patients.

	US	MRI
Patient 1	512*435*18 voxels of 0.152*0.156*1 mm ³	640*640*44 voxels of 0.47*0.47*5.95 mm ³
Patient 2	512*435*12 voxels of 0.152*0.156*1 mm ³	704*704*40 voxels of 0.5*0.5*2 mm ³
Patient 3	512*435*12 voxels of 0.152*0.156*1 mm ³	432*432*86 voxels of 0.81*0.81*3.6 mm ³

4.3. Evaluation metrics:

4.3.1. Visual assessment:

Considering that a ground truth for the registration evaluation was not available, a first assessment was done using a segmentation approach. For all datasets, an expert radiologist contoured the prostate on both modalities after the first affine registration step as well as after the complete registration process (after the non-rigid registration step) using 3D Slicer (www.slicer.org). Since the registration evaluation was based on this manual segmentation, and considering the inaccuracies in delineating the base and the apex of the prostate, the expert was asked to contour the prostate only on slices where the prostate boundaries on both modalities can be clearly detected without any difficulties. A visual assessment of the prostate boundaries' overlap was then considered to evaluate both the affine and the non-rigid registration steps.

4.3.2. Quantitative criteria:

To quantitatively evaluate the prostate boundaries' overlap, prostate contours were used to determine the bounding box that encloses the segmented slices of the prostate in both images after the first affine registration and after the non-rigid registration step. A bounding box for a point set (expert's prostate contours) is defined as the box with the smallest measure within which all the points lie. The bounding box characteristics (size, centroid and orientation relative to the coronal axis) in both images were subsequently compared.

In order to determine the degree of prostate boundaries' overlap, the Hausdorff distance (d_H) measure was used [4]. d_H measures the degree of mismatch between two point sets (expert's prostate contours in both images) by measuring the maximum distance of one point set to the closest point in the second set. Let A and B be the two point sets, the Hausdorff distance d_H is then given by:

$$d_H(A, B) = \max \{d_h(A, B), d_h(B, A)\} \quad (1)$$

where:

$$d_h(A, B) = \max_{a \in A} \left\{ \min_{b \in B} \{d(a, b)\} \right\} \quad (2)$$

and $d(a, b)$ is the Euclidian distance between the points a and b .

In the rest of this work, we will refer to Hausdorff distances between 2D images (slices) by $2D_{d_H}$, whereas $3D_{d_H}$ represents the Hausdorff distance between 3D image volumes.

Finally, the Dice Similarity Coefficient (DSC) was also used to compute the degree of prostate boundaries' overlap between the two images. DSC can be used to measure how similar two images are, in terms of the number of common pixels. It ranges between 0 (no overlap) and 1 (complete overlap). For two given images A and B , DSC is calculated as follows:

$$DSC = \frac{2|A \cap B|}{|A| + |B|} \quad (3)$$

where the operator $| \cdot |$ represents the size of a set, and \cap represents the intersection of two sets.

4.3.3. Reproducibility and robustness:

The evaluation criteria proposed in section 4.3.2. are used on the registered images after the manual segmentation step. Therefore, errors may originate from either the registration method itself or from the manual segmentation step.

In order to evaluate the segmentation errors, two expert radiologists were asked to contour the whole volume of the prostate twice for all patient datasets. Each expert was blinded to the segmentations performed by the other expert as well as to his first segmentation when repeating the task for the second time. Firstly, for all patient datasets, $3D_{d_H}$ was calculated between prostate contours in both images for each of the two segmentations performed by both experts. Subsequently, the reproducibility of the segmentation was studied by comparing the mismatches from the two segmentations performed by each expert separately (intra-observer variability) and to each other (inter-observer variability).

Concerning the registration errors, the robustness of the proposed approach was studied. The robustness study consisted in evaluating the performance of the method in the presence of perturbations, such as for example changes in initialization. Therefore, the initialization of the method was modified (by translating and/or rotating the floating image before the registration, deformations of up to ± 50 mm and $\pm 30^\circ$ were considered) and the registration results were

tracked in order to determine the magnitude of perturbations that can be tolerated in terms of the overall registration accuracy.

4.4. Results:

4.4.1. Pre-operative MRI/CT registration:

4.4.1.1. Setting the parameters of the optimizer:

As previously mentioned in section 2.3.2., the transformation that aligns the MR and CT images was determined iteratively using regular step gradient descent optimizer. The parameters of the optimizer (step size, relaxation factor, and number of iterations) were adjusted in order to get the best results. Concerning the step size, too large steps should be avoided to prevent the optimizer from falling into a local maximum. Too small steps, on the other hand, might slow down the registration process. Figure 4.8 shows metric (mutual information) values, at each iteration of the optimizer, during the first affine registration using different step size values. A step size = 1 was found to give the best results, where larger values of the mutual information indicate a better alignment between the two images.

Regarding the relaxation factor (ranges from 0 to 1), different factor values were tested, when fixing the step size to a value =1, and mutual information values were tracked during the first affine registration step. Large factor values lead to insufficient decrease of the step size giving the cost function a very oscillating form and resulting in divergence from the global maximum. Smaller factor values, however, will rapidly shrink the step size while it is still too far from the global maximum resulting in a slow convergence. Factor value = 0.8 gave the best results, in terms of convergence, where the optimizer reached the global maximum after 200 iterations while it took around 300 iterations to reach the same mutual information value using a factor = 0.5, as illustrated in the figure 4.9.

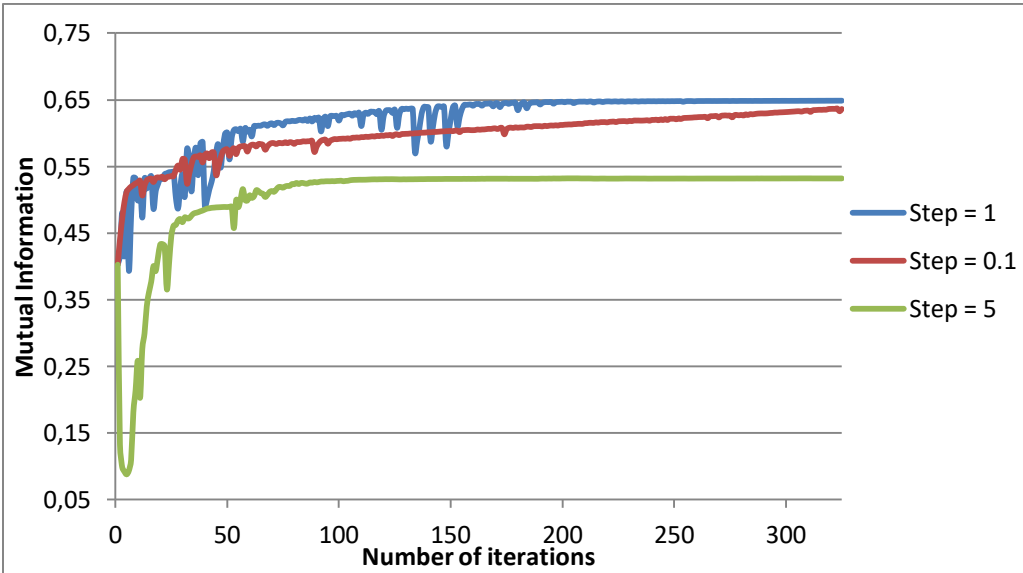


Figure 4.8. Mutual information values at each iteration of the optimizer, during the affine registration, using different step values.

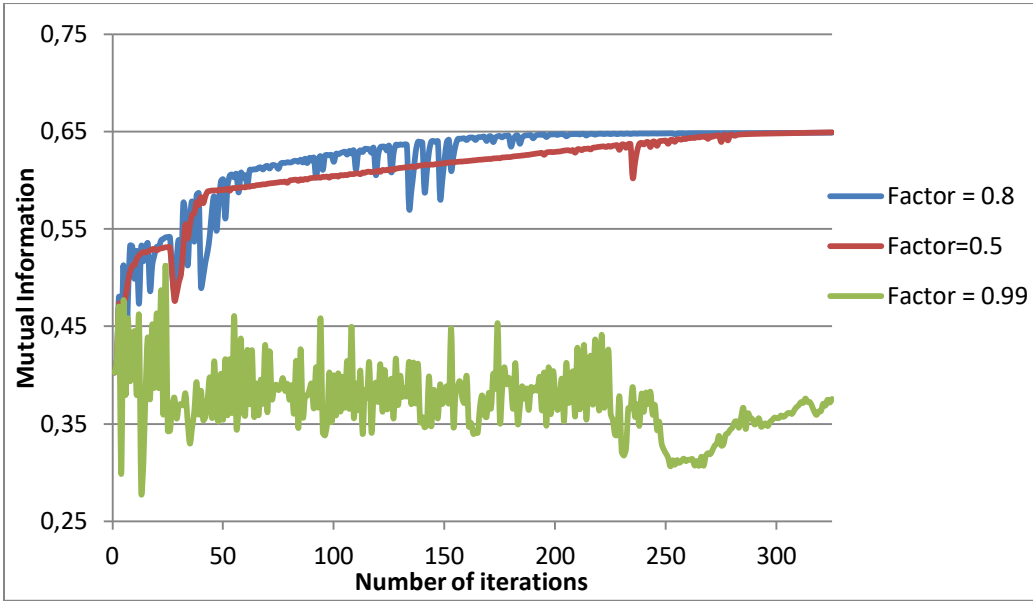


Figure 4.9. Mutual information values at each iteration of the optimizer, during the affine registration, using different factor values.

Finally, after fine tuning the step size and the relaxation factor, the evolution of the registration process was tracked in order to determine the optimal number of iterations necessary to achieve convergence. Figure 4.10 shows mutual information values, at each iteration of the optimizer, during the first affine registration step. As illustrated in figure 4.10, several local maxima were passed by the optimizer, but the convergence was however achieved. There was no need to continue the optimization process after 200 iterations since a global maximum was reached.

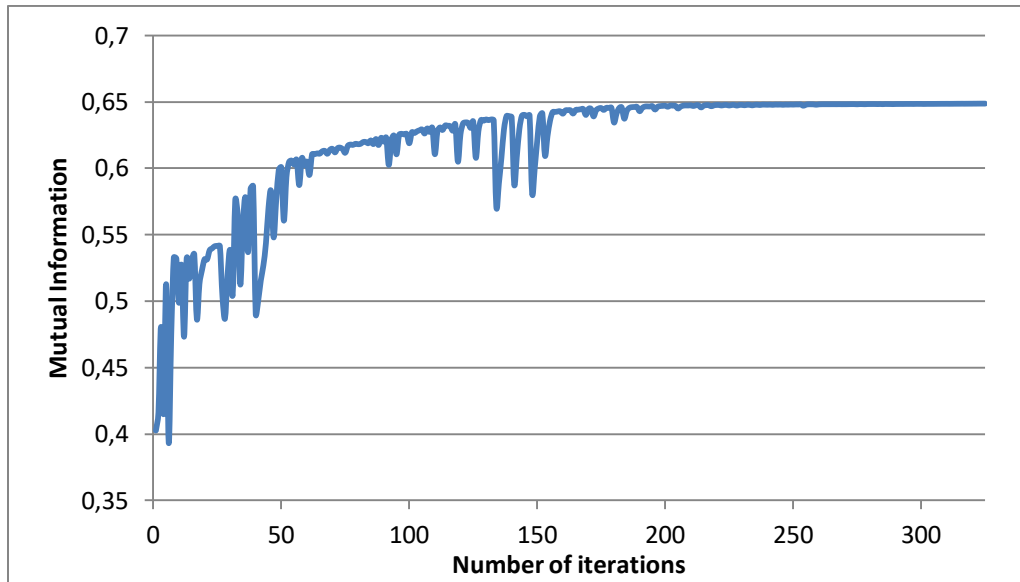


Figure 4.10. Mutual information values at each iteration of the optimizer during the affine registration step.

Mutual information values, at each iteration of the optimization process, during the second non-rigid registration step are illustrated in figure 4.11. It can be seen that the first affine registration helped initializing the second non-rigid registration step from a solution that is close to the optimal one; reducing the probability of falling into local maxima. Larger mutual information values were obtained during the non-rigid registration; indication a better alignment. The convergence was achieved after 350 iterations, where a global maximum was reached and mutual information values were stable afterwards.

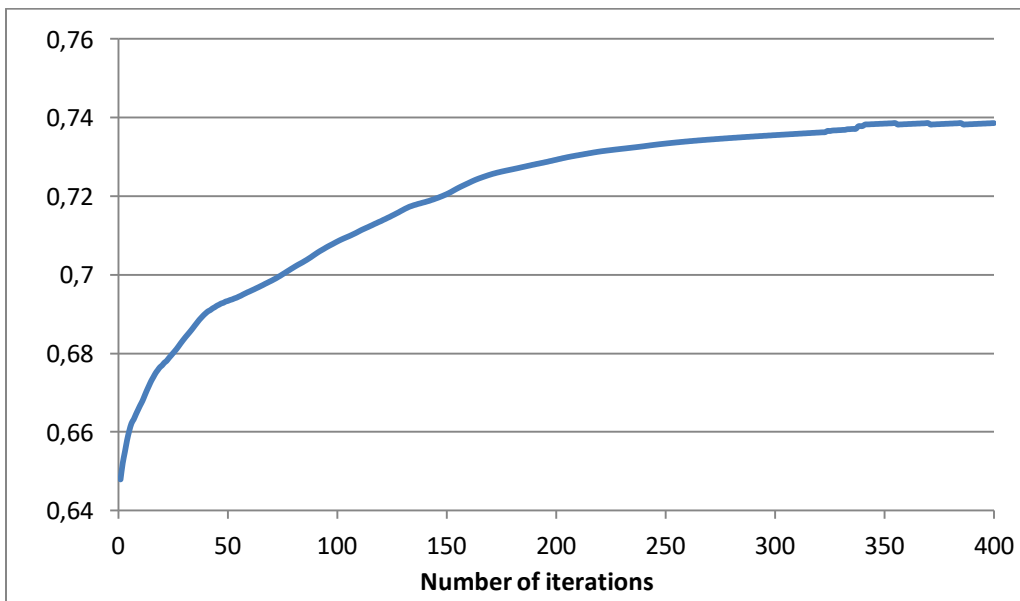


Figure 4.11. Mutual information values at each iteration of the optimizer during the non-rigid registration step.

Considering the overall computational efficiency, the proposed MRI/CT registration method was completed on an average of 2.0 ± 0.25 minutes, on an Intel® Core™ i7-3840QM CPU @ 2.80 GHz processor.

4.4.1.2. Evaluation metrics:

- Visual assessment:

Figure 4.12 shows a checkerboard between MR and CT images of one of the patient datasets after the affine registration only (4.12(a)) and after the non-rigid registration (4.12(b)). A checkerboard between images of another patient dataset with the largest prostate deformations between the two modalities, due to different rectum fillings, is illustrated in figure 4.13.

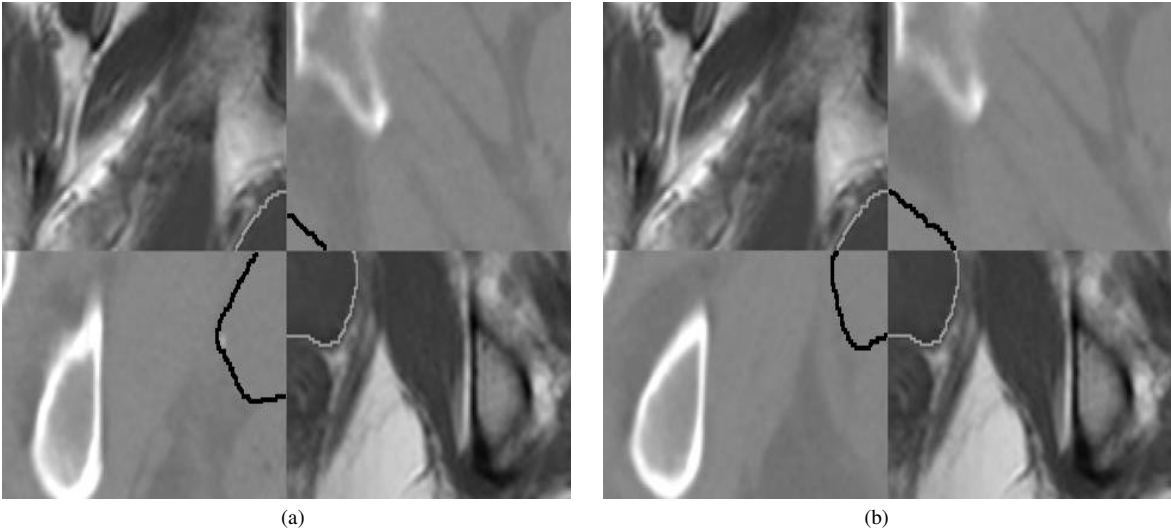


Figure 4.12. Checkerboard showing prostate contours on MR and CT images, (a) after affine registration, (b) after non-rigid registration.

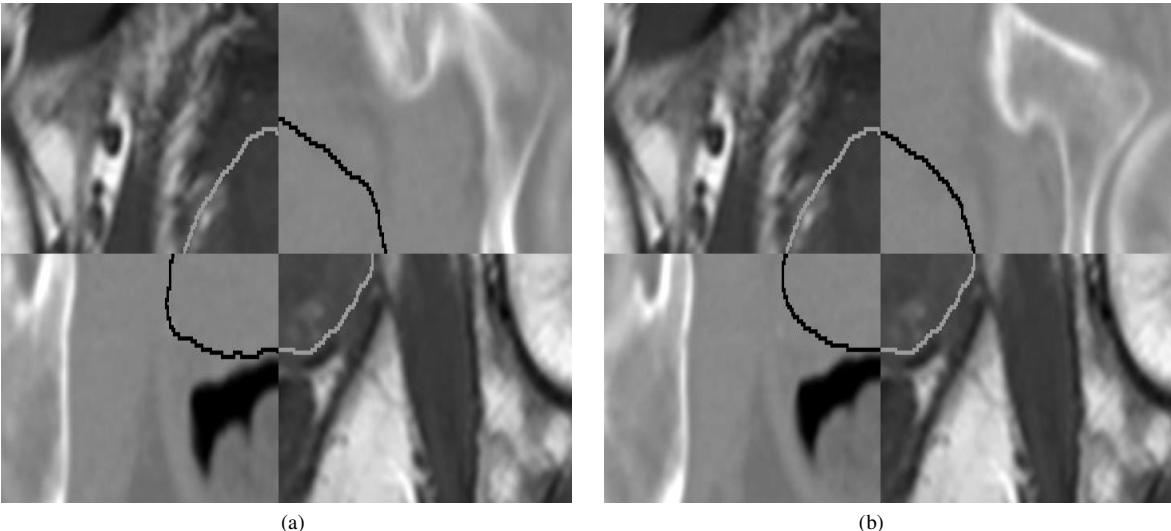


Figure 4.13. Checkerboard showing prostate contours on MR and CT images, (a) after affine registration, (b) after non-rigid registration.

4.4. Results

In all cases, the results were visually acceptable and no significant residual misalignment could be observed. The prostate contours following the non-rigid registration were continuous between MR and CT images for all datasets. Moreover, the rectum and the pelvic bones were also continuous after the non-rigid registration. This visual assessment indicates that the proposed non-rigid registration approach was able to align the images from the two modalities in a prostate imaging context.

Prostate boundaries' overlap was also checked in the sagittal view in order to verify the alignment in 3D. This view would help clinicians in detecting the boundaries of the prostate (base and apex), which is essential when irradiating prostate tumors. Figure 4.14 shows a checkerboard between MR and CT images of one of the patient datasets after affine registration only (4.14 (a)) and after non-rigid registration step (4.14(b)).

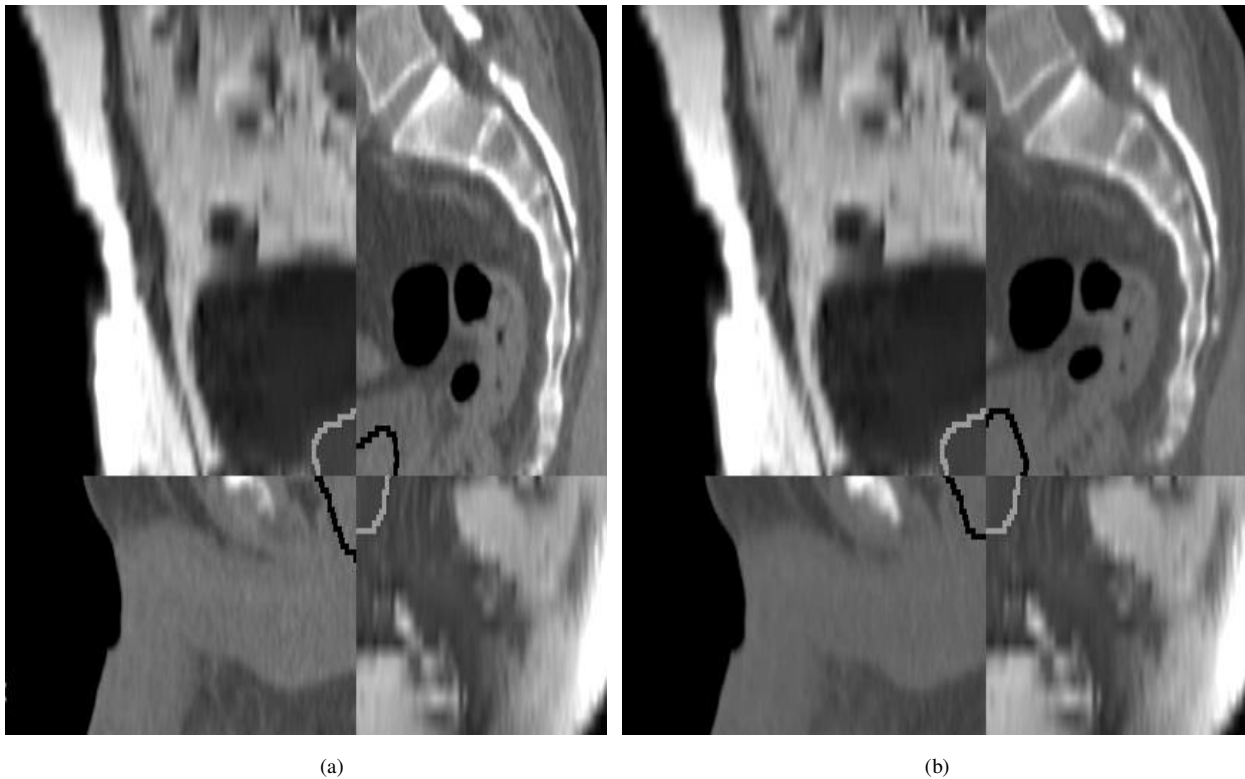


Figure 4.14. Checkerboard showing prostate contours on MR and CT images in sagittal view, (a) after affine registration and (b) after non-rigid registration.

Despite the low resolution, and therefore the poor quality, in the sagittal view, no significant misalignment could be observed. Prostate contours were almost continuous between MR and CT images for all patient datasets following the non-rigid registration, indicating the ability of the proposed methodology to align MR and CT images.

- Quantitative criteria:

Bounding box:

Prostate contours following the non-rigid registration step were used to automatically determine a bounding box around the prostate in MR and CT images for all datasets. The characteristics of these bounding boxes for all patient datasets are given in table 4.3.

Table 4.3. Characteristics of bounding boxes enclosing the prostate in MRI and CT.

		Centroid (voxels)	Orientation (degrees)	Size (voxels)
Patient 1	MRI	[316.8, 353.0, 2.6]	5.73	[96.5, 85.9, 6.5]
	CT	[317.0, 353.2, 2.6]	5.61	[96.5, 85.7, 6.5]
Patient 2	MRI	[330.3, 332.2, 3.1]	178.19	[104.4, 69.6, 7.6]
	CT	[330.4, 332.0, 3.1]	177.62	[104.4, 69.7, 7.6]
Patient 3	MRI	[163.3, 140.9, 1.4]	174.18	[37.6, 29.6, 4.1]
	CT	[163.4, 141.0, 1.4]	174.75	[37.6, 29.4, 4.1]
Patient 4	MRI	[170.0, 140.1, 1.6]	178.76	[36.0, 23.0, 4.3]
	CT	[170.1, 140.0, 1.6]	179.34	[36.1, 23.8, 4.3]
Patient 5	MRI	[173.9, 183.1, 2.1]	168.99	[48.5, 47.6, 5.2]
	CT	[174.1, 183.3, 2.2]	169.60	[48.1, 47.2, 5.2]
Patient 6	MRI	[75.7, 81.7, 2.8]	28.07	[36.3, 31.6, 6.3]
	CT	[75.6, 81.6, 2.8]	28.65	[36.4, 31.9, 6.3]
Patient 7	MRI	[84.2, 86.3, 3.2]	28.07	[37.1, 36.3, 7.7]
	CT	[84.4, 86.4, 3.2]	27.50	[37.4, 36.5, 7.7]
Patient 8	MRI	[82.9, 73.2, 2.3]	4.58	[42.4, 32.2, 5.5]
	CT	[83.8, 73.3, 2.3]	4.01	[42.3, 32.1, 5.5]

The comparison between the bounding boxes in MR and CT images gave good results in terms of voxel size with differences of less than a single voxel. As for the orientation, bounding boxes had the same orientation with a difference of less than 1° for all datasets. Initial orientations were around 175° for patients 2, 3, 4 and 5, and it was different for the rest where the patient positioning on the table was less inclined with smaller orientations of around 5° for patients 1 and 8 and of 28° for patients 6 and 7.

Hausdorff distance:

Mismatches between prostate contours in the corresponding slices of the MR and CT images were calculated for all patient datasets after the affine registration only and after the non-rigid registration step, using $2D_{d_H}$. Figure 4.15 illustrates these mismatches after the affine registration step in the form of box plots (box and whisker diagram). The box spans the first quartile to the third quartile (with quartiles being the values dividing a list of numbers into quarters). A horizontal segment inside this box represents the median value. Whiskers on both sides show the locations of the minimum and the maximum values. Mismatches between prostate contours following the non-rigid registration step are illustrated in figure 4.16.

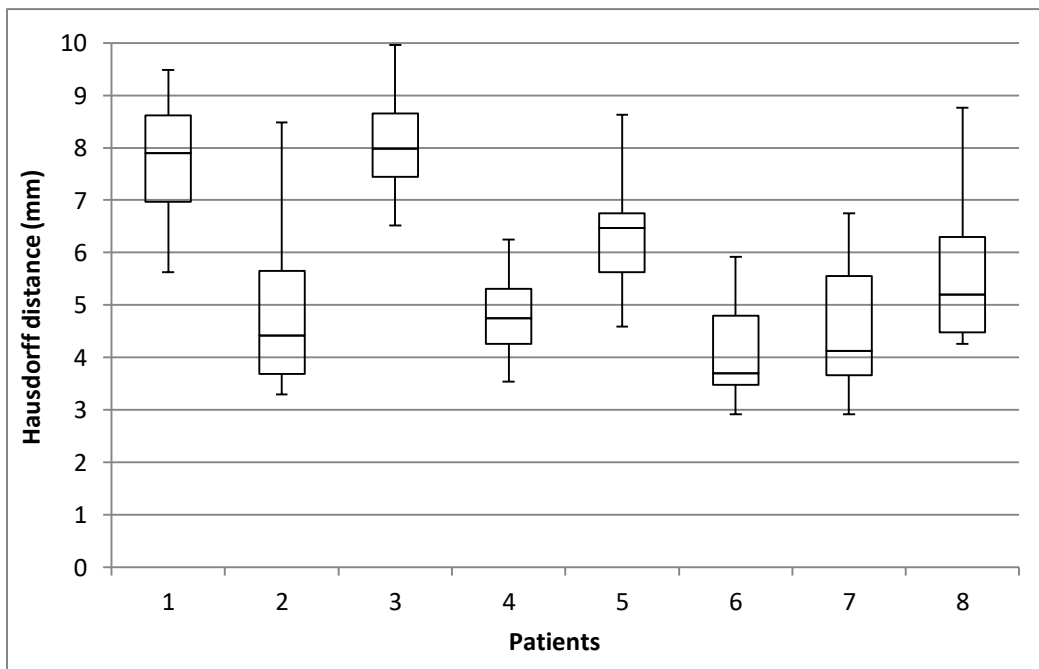


Figure 4.15. Box plots representing the 2D Hausdorff distances between prostate contours in MR and CT images following the affine registration step.

As illustrated in figures 4.15 and 4.16, the value of mismatch between prostate contours in MR and CT images following the affine registration step was 5.80 ± 1.47 mm. The non-rigid registration step however corrected this misalignment, resulting in a mismatch value of 1.15 ± 0.20 mm. As for the maximum mismatch value, it reached 9.965 mm after the affine registration for one of the patient datasets, while it was always less than 2 mm for all eight patient datasets considered following the non-rigid registration step.

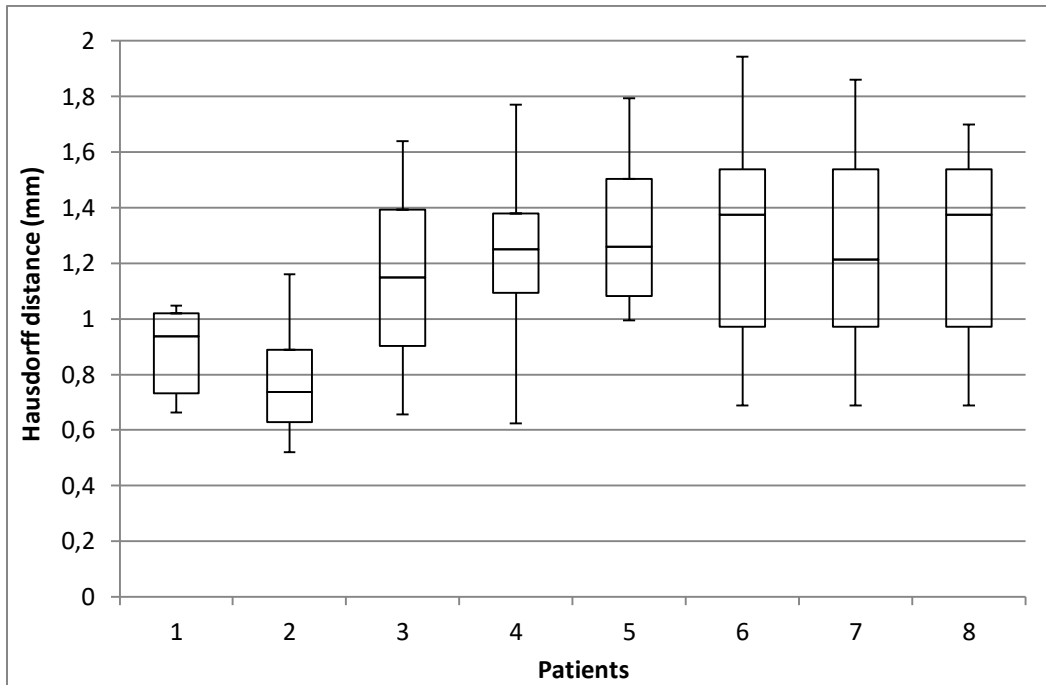


Figure 4.16. Box plots representing the 2D Hausdorff distances between prostate contours in MR and CT images following the non-rigid registration step.

Dice Similarity Coefficient:

The Dice Similarity Coefficient was finally calculated for all datasets in order to assess the overlap between prostate contours in both modalities. Figure 4.17 shows the DSC values for all patients considered after the affine registration only (in blue) and after the non-rigid registration step (in red).

As illustrated in the figure 4.17, DSC value between prostate contours in MR and CT images following the affine registration only was 0.72 ± 0.07 . After the non-rigid registration step however, DSC value was significantly better, with a value of 0.96 ± 0.014 , given that DSC value ranges between 0 (no overlap) and 1 (complete overlap).

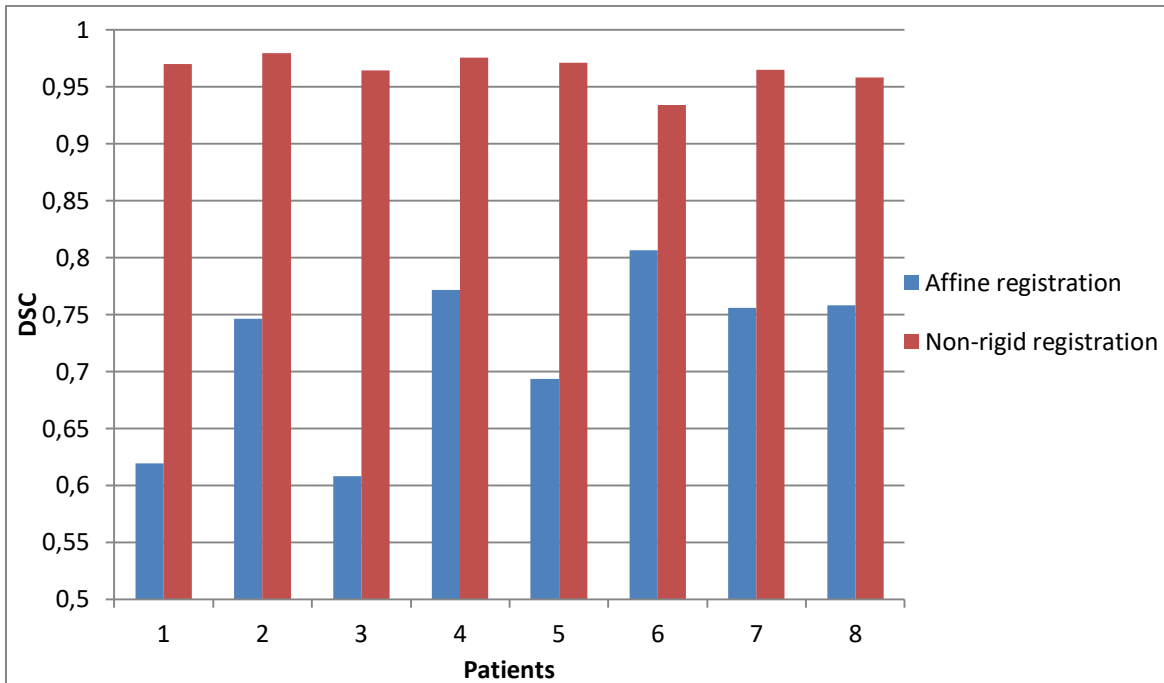
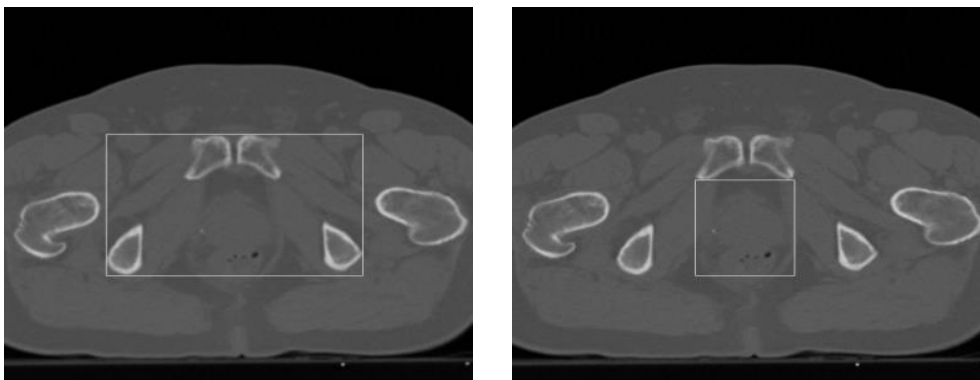
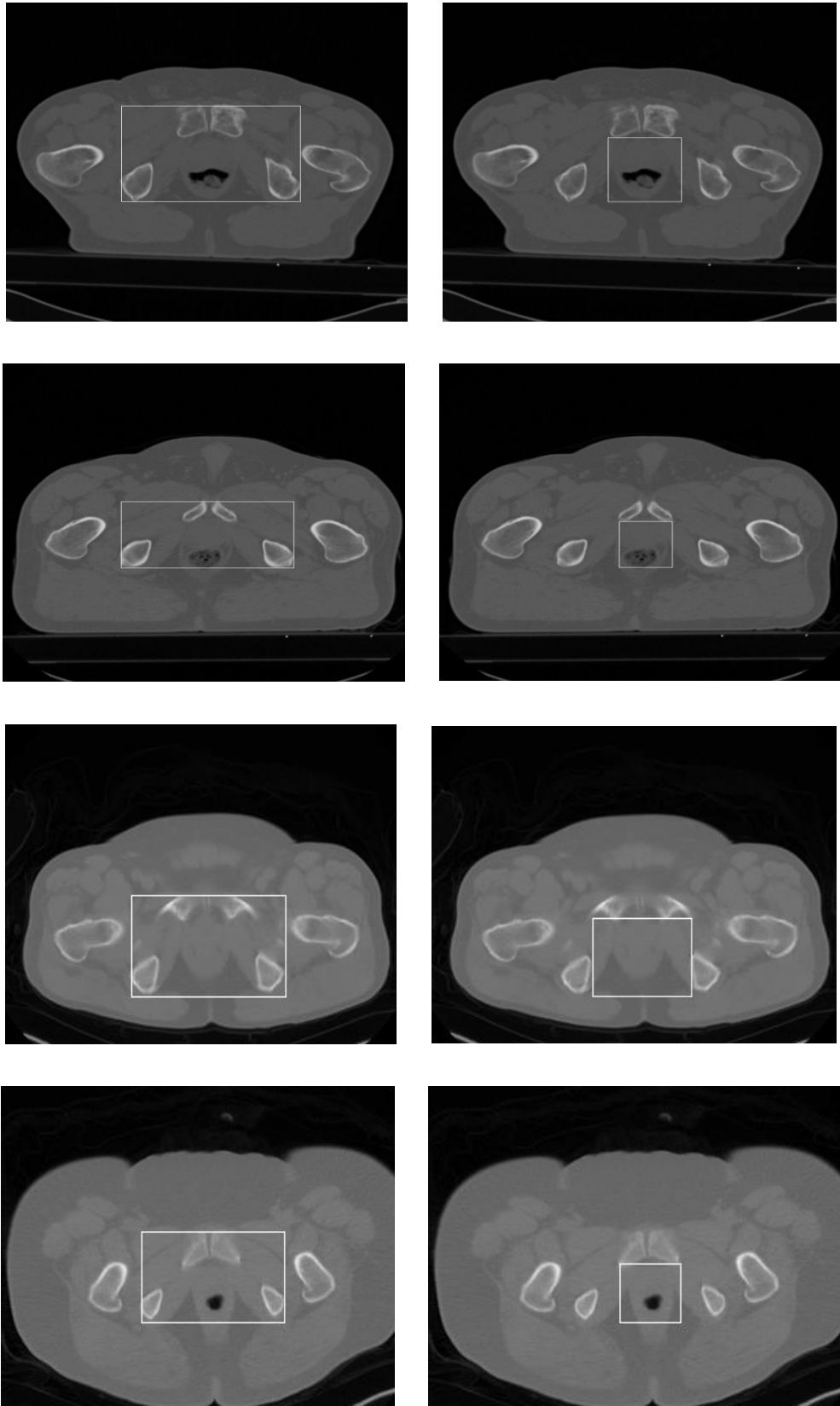


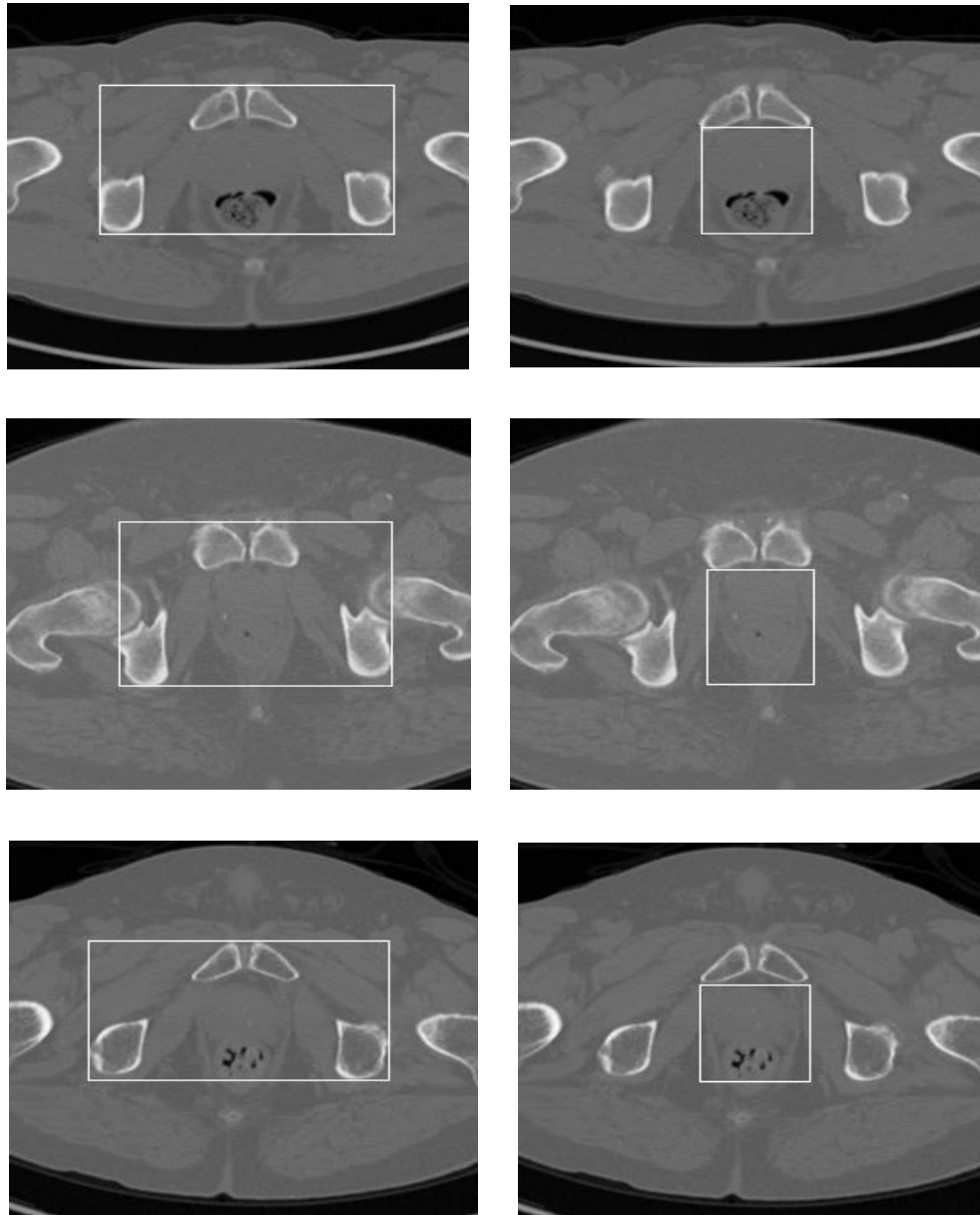
Figure 4.17. DSC values between prostate contours in MR and CT images after the affine registration only (in blue) and after the non-rigid registration step (in red).

- Reproducibility and robustness:

At first, the robustness of the VOI determination on the CT image was evaluated, where the method described in section 2.2.1. was applied on all patient datasets considered in this study. Figure 4.18 illustrates the CT slices extracted after applying the MIP on each of the eight patient datasets. The images containing the pelvic and the prostate VOI are illustrated in the first (4.18(a)) and the second column (4.18(b)), respectively.







(a) (b)
Figure 4.18. VOIs determination on CT, (a) pelvic VOI and (b) prostate VOI.

As illustrated in figure 4.18, the VOI determination on CT gave good results, where the pelvic VOI was always around the pelvic bones while the prostate VOI included the prostate for all patient datasets considered in this study.

Consequently, regarding the reproducibility of the method, mismatches between prostate contours in MR and CT images were calculated for all patient datasets using $3D_{d_H}$. Mismatches in each of the segmentations performed by the two experts are illustrated in figure 4.19 in the form of box plots.

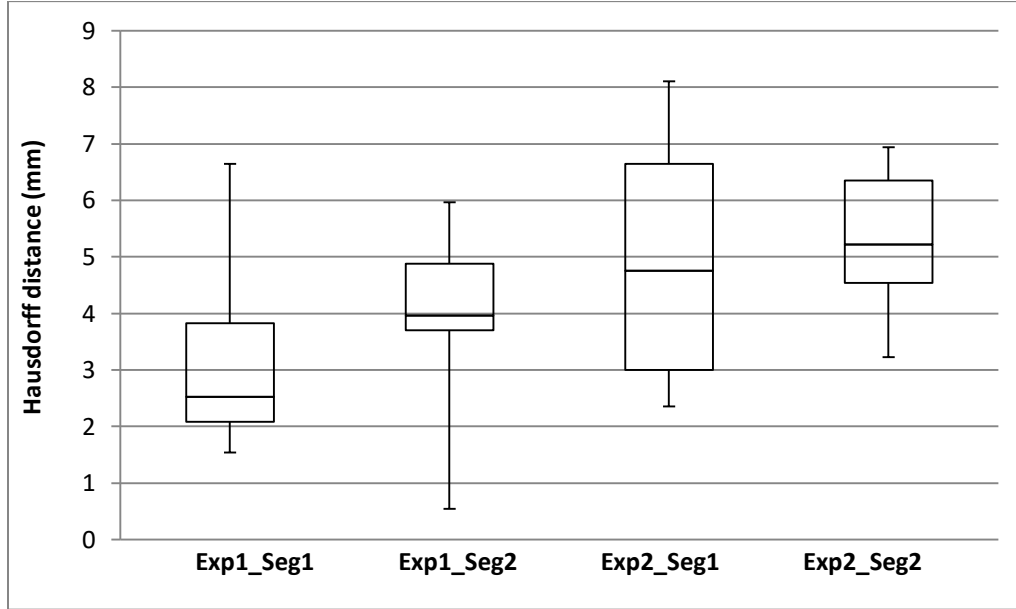


Figure 4.19. Box plots representing the 3D Hausdorff distances between prostate contours in MR and CT images. Exp1 and Exp2 represent the first and the second expert respectively. Seg1 and Seg2 represent the two segmentations.

For each segmentation, the median value of the mismatch between prostate contours in all datasets was calculated. For the first expert, the median mismatch value was 2.53 mm and 3.96 mm for both segmentations. For the second expert these values were bigger, where median mismatch values for the first and the second segmentations were 4.76 mm and 5.22 mm respectively.

Repeating the same task by the two experts revealed intra-observer variability of 1.64 ± 0.79 mm and 2.01 ± 0.68 mm for the first and the second expert respectively. As for the reproducibility of the task, inter-observer variability values of 2.19 ± 1.46 mm and 1.93 ± 1.26 mm were measured considering the two repeated segmentations from the two experts respectively.

In terms of robustness, the resulting mismatch between prostate contours in MR and CT images was always less than 2 mm for all patient datasets, irrespective of the magnitude of deformations.

4.4.2. Intra-operative US/MRI registration:

The proposed US/MRI registration methodology was validated at first using a prostate phantom to evaluate its feasibility. Then, it was validated using three datasets of patients undergoing brachytherapy.

4.4.2.1. Prostate phantom:

Figure 4.20 shows a checkerboard between US and MR images of the prostate phantom after the non-rigid registration.

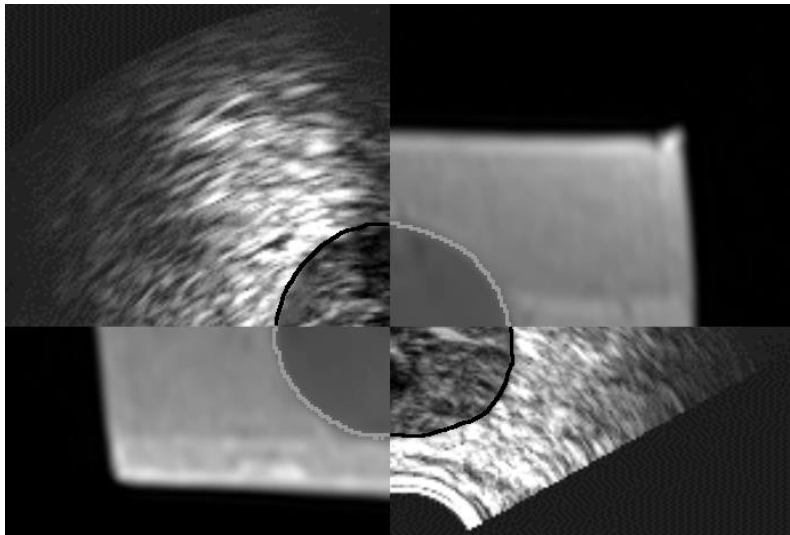


Figure 4.20. Checkerboard showing prostate contours on US and MR phantom images after non-rigid registration.

Result is visually acceptable since no residual misalignment can be observed and the prostate contours are continuous between US and MR images after the non-rigid registration.

In order to determine the degree of prostate boundaries overlap, the mismatch between prostate contours in US and MR phantom images was calculated after the non-rigid registration step, using $2D_{d_H}$, resulting in a registration error of 1.48 mm. Moreover, the DSC was also calculated after the non-rigid registration, resulting in a value of 0.98. These results indicate the feasibility of the proposed methodology to align US and MR images in a prostate imaging context.

4.4.2.2. Clinical patient datasets:

A. Mutual Information:

At first, and in order to justify the use of LC^2 metric in registering US and MR images, the proposed registration methodology was compared with another US/MRI registration method. Similarly to the pre-operative registration, a method based on the maximization of the mutual information in combination with a deformation field parameterized by B-Splines was used. A first affine registration was therefore applied, and followed by a second non-rigid registration step. The parameters of the optimizer were fine-tuned, similarly to the study described in section 4.4.1.1., in order to determine the optimal set of parameters that can bring the two images into alignment. Afterwards, an expert manually segmented the prostate on both images after the non-rigid registration; a checkerboard of prostate contours on US and MR images is illustrated in figure 4.21.

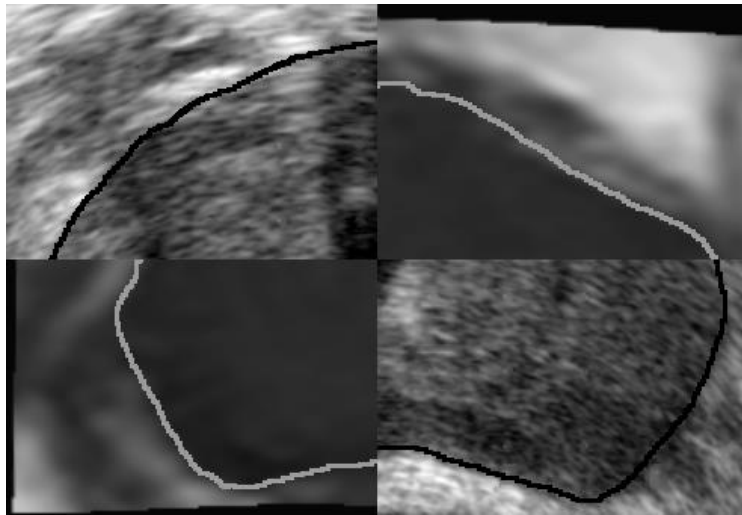


Figure 4.21. Checkerboard showing prostate contours on US and MR images after non-rigid registration using mutual information.

As illustrated in figure 4.21, the prostate contours were not continuous after the non-rigid registration; indicating that the registration method was not able to align these modalities using the mutual information as a similarity measure. Moreover, the Hausdorff distance was calculated between prostate contours in both images resulting in a mismatch value of 6.69 mm.

B. LC^2 :

Since registration methods using simple similarity measures, such as the mutual information, were not able to bring the US and MR images into alignment in a prostate imaging context, a new similarity measure (LC^2), which correlates the US intensity with the MR intensity and gradient, was explored.

The local LC^2 is computed for each pixel x_i in the US image considering a neighborhood Ω of m pixels centered on that pixel, using the equation:

$$LC^2_{local} = 1 - \frac{\sum_{x_i \in \Omega} \|US(x_i) - f(MRI(x_i))\|^2}{|\Omega| \sum_{x_i \in \Omega} \text{var}(US(x_i))} \quad (4)$$

Therefore, the size of this neighborhood has to be adjusted, considering that it has an impact on the precision of the measure. Different neighborhood sizes were tested and LC^2 values were tracked, at each iteration of the optimizer, during the first affine registration step. If the size value is too small, the equation will always hold and the LC^2 will not be decreased with misalignment. On the other hand, if the size is too large, the equation will not hold for the correct alignment, since structures with different weightings for intensity and gradient will share the same neighborhood. A patch = 9 (patch being the number of pixels in each direction resulting in a neighborhood size of $(2 * Patch + 1)^2 = 361$) gave the best results in term of convergence, where larger LC^2 values indicate better alignment, as illustrated in the figure 4.22.

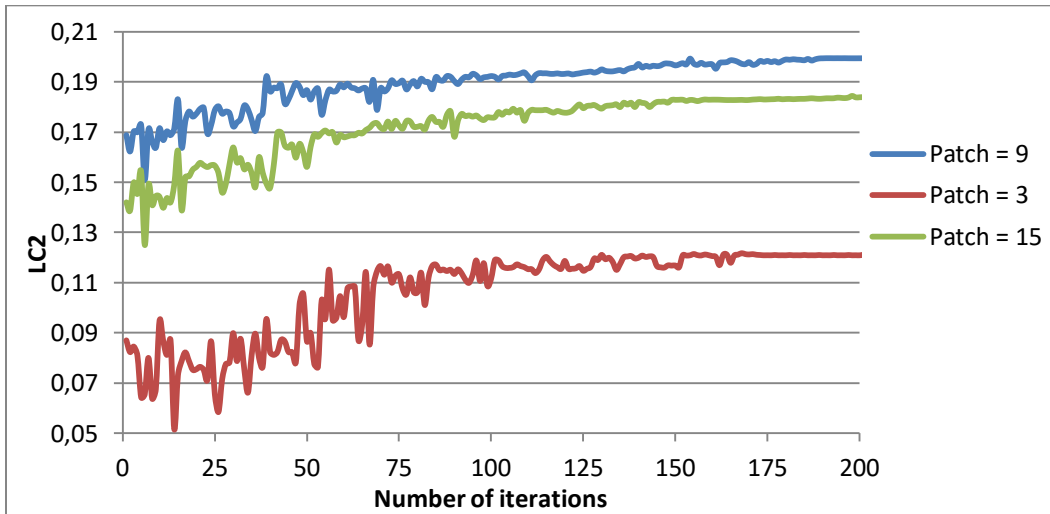


Figure 4.22. LC^2 values at each iteration of the optimizer, during the affine registration, using different patch size values.

Subsequently, the parameters of the optimizer, which determines the transformation aligning the two images, were adjusted similarly to the study conducted in section 4.4.1.1. In the case of Amoeba optimizer, the initial simplex size has an impact on the convergence. Different simplex size values were tested while tracking LC^2 values, with respect to the number of iterations, during the first affine registration step, as illustrated in the figure 4.23.

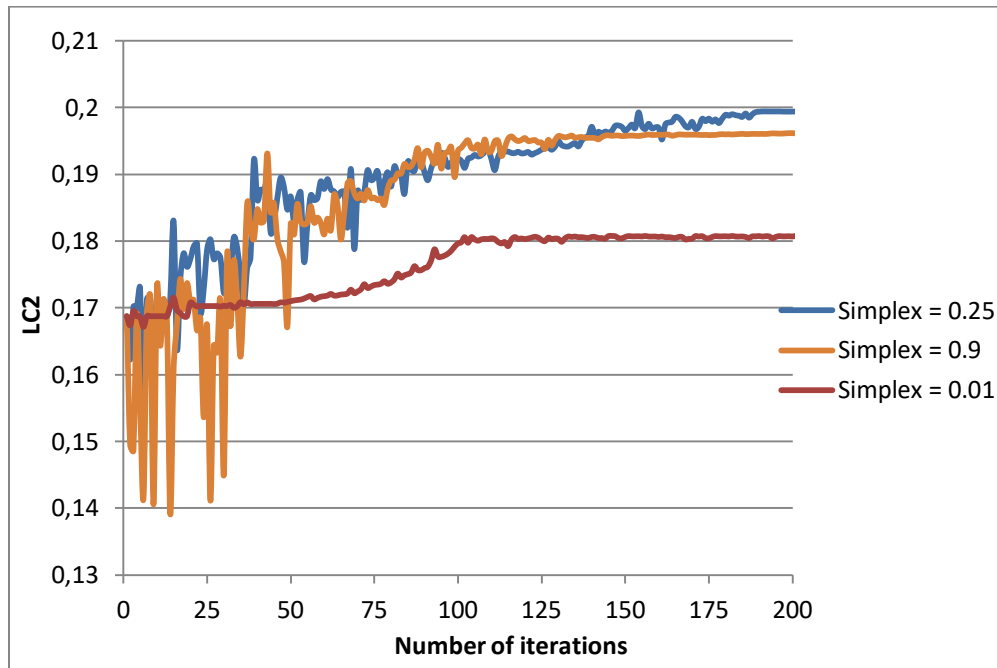


Figure 4.23. LC^2 values at each iteration of the optimizer, during the affine registration, using different simplex size values.

As illustrated in the figure 4.23, larger simplex size values gave the cost function an oscillating form but the convergence was however reached. Smaller values, on the other hand, resulted in a much smoother cost function, but the optimizer did not reach the global maximum. Therefore, a trade-off between precision and smoothness of the cost function has to be made. A simplex value = 0.25 was found to give the best results, where the cost function was not so smooth but the global maximum was however reached.

Regarding the computational efficiency, the proposed two-step registration method was completed on an average of 2.75 ± 0.25 hours, on an Intel® Core™ i7-3840QM CPU @ 2.80 GHz processor. A first non-optimal implementation on GPU (NVIDIA TITAN X Pascal) was however able to speed up the registration process by a factor of 40. Combining 4 GPUs in the same workstation would therefore reduce the computational time to less than 30 seconds (see section 3.3.2.) which is compatible with time constraints in a clinical workflow.

C. Evaluation metrics:

- Visual assessment:

Figure 4.24 shows a checkerboard between US and MR images of one of the patient datasets after the affine registration (4.24(a)) and after the non-rigid registration step (4.24 (b)).

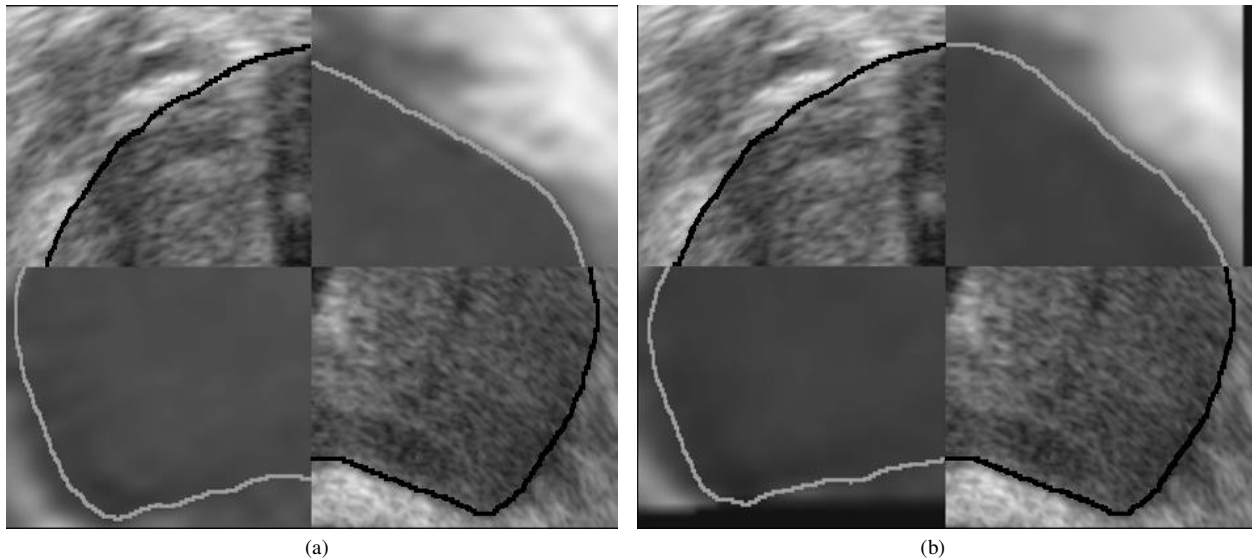


Figure 4.24. Checkerboard showing prostate contours on US and MR images (a) after affine registration, (b) after non-rigid registration.

The results were visually acceptable since no significant residual misalignment could be observed for all datasets. The prostate contours after the non-rigid registration were continuous between US and MR images, indicating that the proposed approach was able to bring these images into alignment in a prostate imaging context.

- Quantitative criteria:

Bounding box:

Prostate contours were used to automatically determine a bounding box around the prostate in US and MR images for all datasets. The characteristics of these bounding boxes are given in table 4.4.

The comparison between the bounding boxes in US and MR images gave good results in terms of voxel size with differences of almost 3 voxels. As for the orientation, bounding boxes had the same orientation with a difference of 3° for one of the patient datasets.

Table 4.4. Characteristics of bounding boxes enclosing the prostate in US and MRI.

		Centroid (voxels)	Orientation (degrees)	Size (voxels)
Patient 1	MRI	[158.9, 120.8, 2.0]	176.53	[313.3, 199.0, 5.1]
	US	[160.4, 121.6, 2.0]	177.62	[311.0, 202.4, 5.1]
Patient 2	MRI	[161.7, 142.9, 2.0]	178.34	[319.3, 247.1, 5.1]
	US	[163.0, 142.3, 2.0]	175.61	[322.4, 245.1, 5.0]
Patient 3	MRI	[193.1, 162.7, 2.0]	170.74	[374.4, 297.8, 5.2]
	US	[193.7, 164.3, 2.0]	170.17	[373.5, 300.8, 5.1]

Hausdorff distance:

Mismatches between prostate contours in the corresponding slices of the US and MR images were calculated for all patient datasets using $2D_{d_H}$. Figure 4.25 and 4.26 illustrate these mismatches in the form of box plots after the affine registration only and after the non-rigid registration step, respectively.

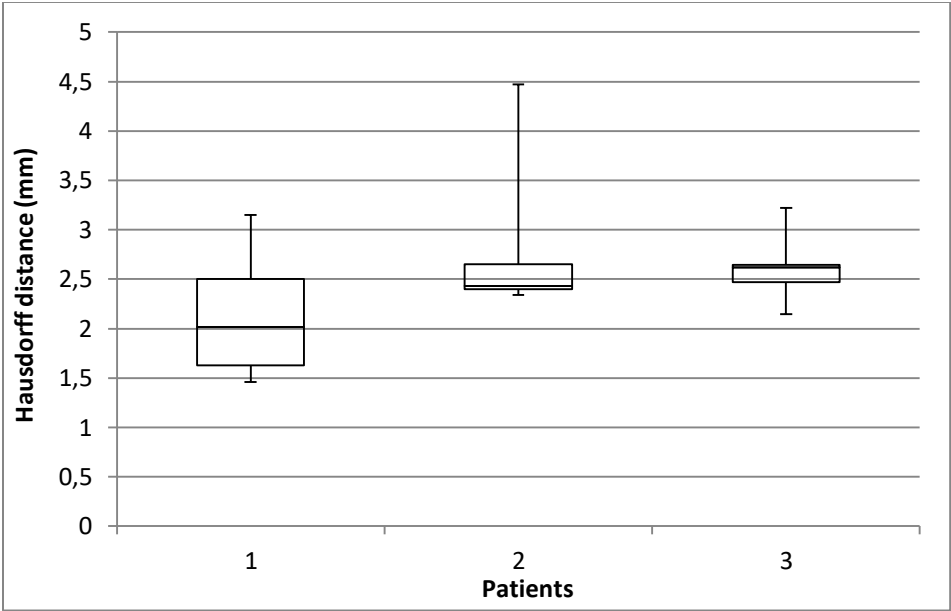


Figure 4.25. Box plots representing the 2D Hausdorff distances between prostate contours in US and MR images following the affine registration step.

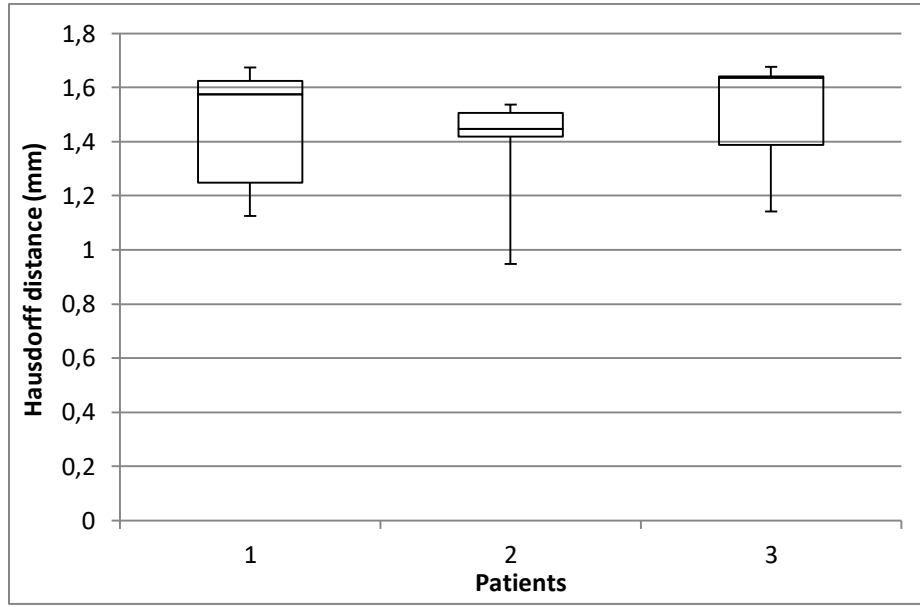


Figure 4.26. Box plots representing the 2D Hausdorff distances between prostate contours in US and MR images following the non-rigid registration step.

As illustrated in figures 4.25 and 4.26, the value of mismatch between prostate contours in US and MR images after the first affine registration step was of 2.54 ± 0.36 mm. The non-rigid registration step that follows however was able to improve the precision of the registration, resulting in a mismatch value of 1.44 ± 0.06 mm. As for the maximum mismatch value, it was as high as 4.47 mm for one of the patient datasets following the affine registration, while it was always less than 1.7 mm for all patient datasets after the non-rigid registration step.

Dice Similarity Coefficient:

The Dice Similarity Coefficient was calculated for all datasets in order to quantitatively compute the degree of the overlap between prostate contours in US and MR images. Figure 4.27 illustrates DSC values for all patient datasets considered after the affine registration only (in blue) as well as after the non-rigid registration (in red).

As illustrated in the figure 4.27, DSC value between prostate contours in US and MR images following the affine registration was 0.955 ± 0.005 . DSC values were slightly better after the non-rigid registration, with a value of 0.977 ± 0.006 , given that DSC value ranges between 0 (no overlap) and 1 (complete overlap).

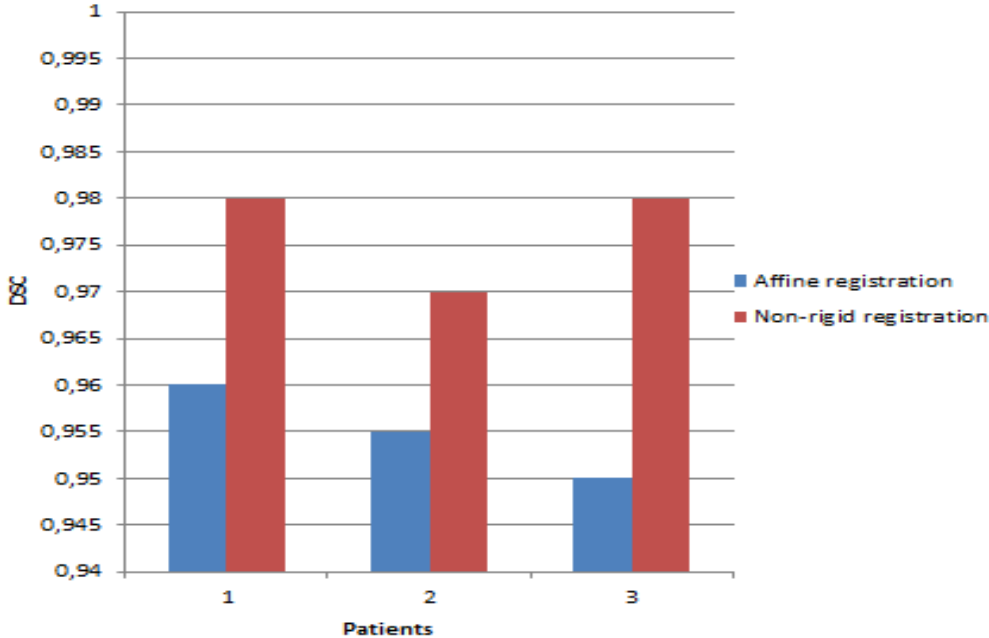


Figure 4.27. DSC values between prostate contours in US and MR images after the affine registration only (in blue) and after the non-rigid registration step (in red).

- Reproducibility and robustness:

The VOIs determined in chapter 3, section 3.2.2. were used to crop the US and MR images, as shown in figure 4.28, before the registration process.

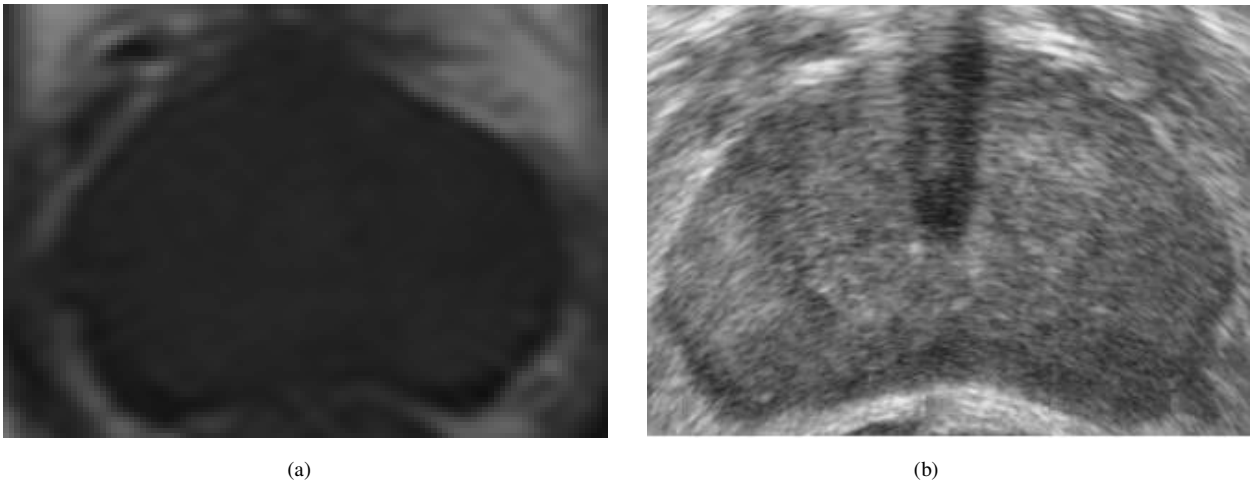


Figure 4.28. Prostate VOIs on (a) MR and (b) US images.

At first, the robustness of the VOI determination on the US image was evaluated by applying the RBR method on all of the US images for all patient datasets considered.

Figure 4.29 shows the prostate boundaries, extracted from the other two patient datasets, along with the corresponding US images containing the bounding boxes that define the prostate VOIs.

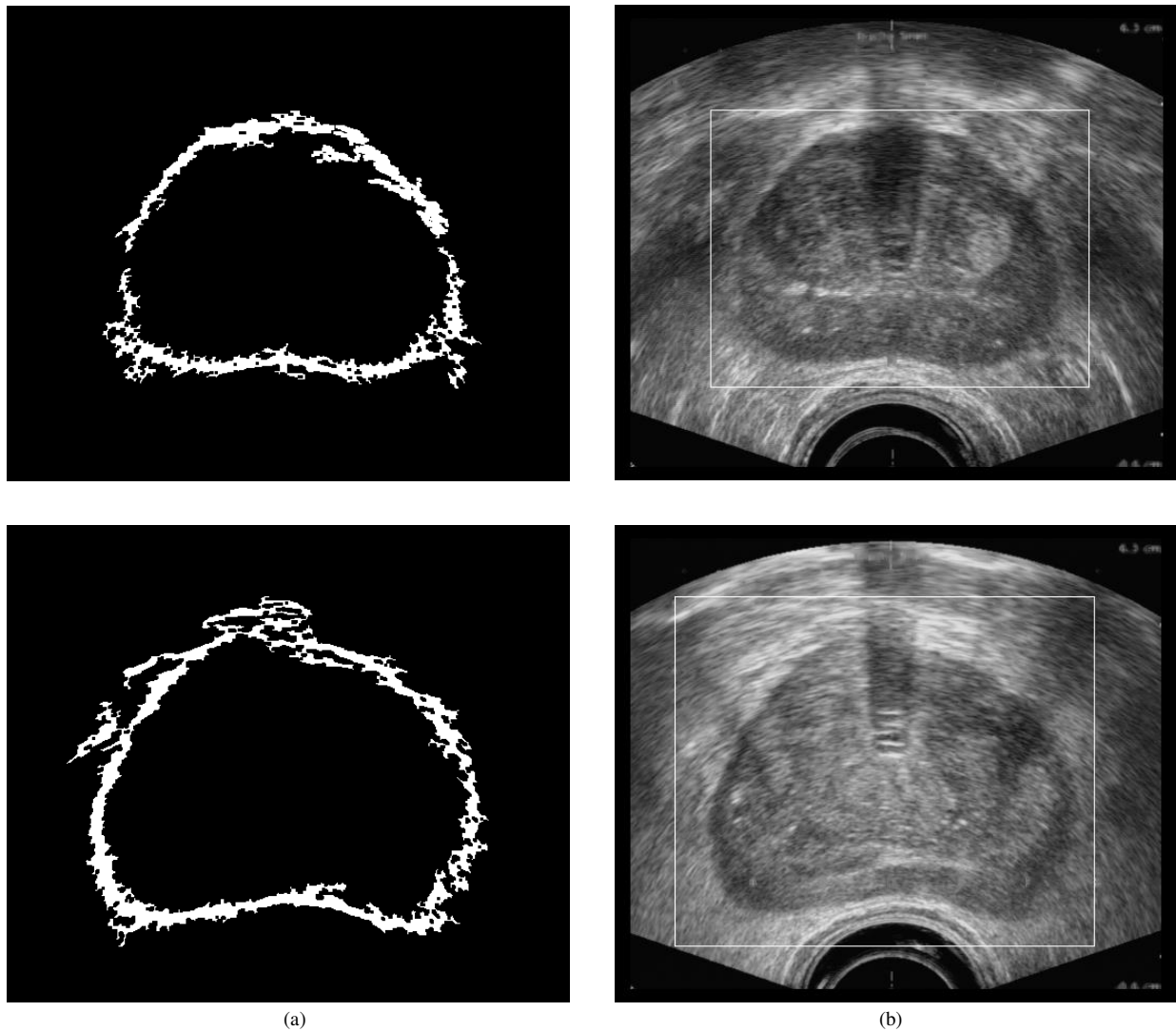


Figure 4.29. (a) Prostate boundaries, (b) prostate VOI on US.

As illustrated in figures 4.29, in some cases prostate boundaries were incomplete, due to morphological operations, (first row (a)), and sometimes the detected boundaries included structures other than the prostate, due to speckle noise present in the US image (second row (a)). Nevertheless, the bounding box defining the prostate VOI included the prostate for all datasets considered.

Consequently, regarding the reproducibility of the method, the manual segmentation is performed only on these small VOIs centered on the prostate, and on slices where the prostate boundaries on both modalities can be detected without any difficulties. Moreover, as illustrated in figure 4.26, the deviation of the mismatch between prostate contours in all datasets was not significant (difference between the minimum and maximum mismatch values was around 0.5 mm).

Therefore, only one expert was asked to perform the manual segmentation on both modalities, and the reproducibility was not studied for the US/MRI registration.

Concerning the robustness, similarly to the pre-operative registration, the resulting mismatch between prostate contours in US and MR images was less than 2 mm regardless of the magnitude of the deformations.

4.4.3. Final US/CT registration:

The two proposed registration methodologies may be combined, leading to a US/CT registration. The first transformation, determined in the pre-operative MRI/CT registration, was applied on the CT image. Then, the second transformation, that aligns the US with the MR image, was also applied on the CT image, resulting in a deformed CT image that is in alignment with the US. Once again, the assessment was done based on a segmentation approach, where an expert manually delineated the prostate on both images after the final registration step. Figure 4.30 shows a checkerboard between US and CT images of one of the patient datasets after the final registration step.

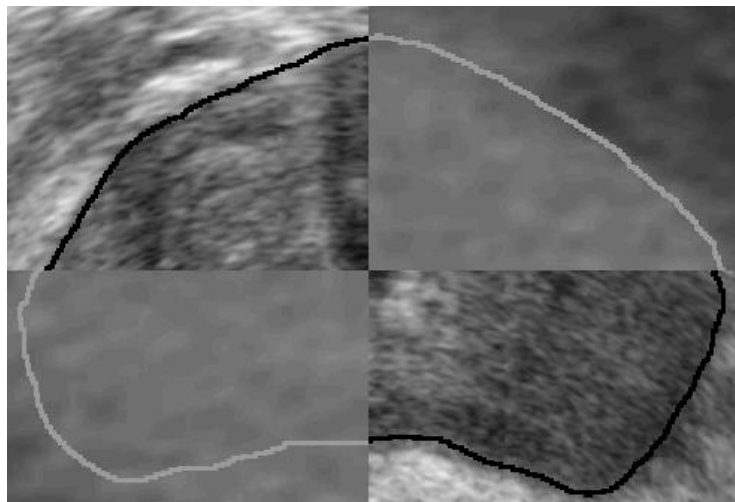


Figure 4.30. Checkerboard showing prostate contours on US and CT images after the final registration step.

Prostate contours between US and CT images following the final registration (pre- and intra-operative registration steps combined) were almost continuous for all patient datasets considered. Given the propagation of the error from the two registration steps as well as the uncertainties associated with the manual segmentation, this slight misalignment can be tolerated. This visual inspection indicates the ability of the proposed methodology to align these images in a prostate imaging context.

4.5. Conclusion:

In this chapter, the two registration methodologies described in the previous chapters were validated using both qualitative and quantitative evaluation criteria. Regarding the pre-operative MRI/CT registration, eight patient datasets were used for the validation, resulting in a registration error of 1.15 ± 0.20 mm. Concerning the intra-operative registration between US and MR images, a prostate phantom is at first used to test the feasibility of the method. Then, the method was validated using three patient datasets, resulting in a residual error value of 1.44 ± 0.06 mm. Finally, both registration methods were combined and the final US/CT registration was evaluated using visual inspection which indicated the ability of the proposed approach to register these kinds of imaging modalities in a prostate imaging context.

References:

- [1] D'Souza WD, Madsen EL, Unal O, Vigen KK, Frank GR, and Thomadsen BR (2001). "Tissue mimicking materials for a multi-imaging modality prostate phantom". *Medical Physics*. **28(4)**: 688-700.
- [2] Hungr N, Long JA, Beix V, and Troccaz J (2012). "A realistic deformable prostate phantom for multimodal imaging and needle-insertion procedures". *Medical Physics, American Association of Physicists in Medicine*. **39(4)**: 2031-41.
- [3] Bude RO and Adler RS. (1995). "An easily made, low-cost, tissue-like ultrasound phantom material". *Journal of Clinical Ultrasound*. **23(4)**: 271-3.
- [4] Hausdorff F. (1914). "Grundzüge der Mengenlehre" (German for "Basics of Set Theory"). Leipzig Viet.

Discussion and Conclusion

The objective of the future brachytherapy protocol is to have a multimodal approach that allows the physician to accurately determine the optimal positions of the radioactive sources, by taking into account the tissues heterogeneities, using CT images rather than the formalism TG-43. This in turn can lead to a more precise estimation of the personalized dose distribution (PDD). Moreover, this approach should provide a better visualization of the dose distribution with respect to the tumor, using the MRI with its superior soft-tissue contrast. The future protocol should also ensure the accurate insertion of the radioactive sources in their pre-planned positions. Since the US is the current modality of choice for seeds placement, and given the poor contrast associated with this modality that may lead to difficulties in distinguishing the boundaries of the prostate and the organs at risk, improving the visualization during the intervention is essential.

In this context, a multimodal approach was proposed in order to improve the overall accuracy of prostate brachytherapy procedures by providing a coherent and accurate solution, which explores the information provided by these different imaging modalities: US, MRI and CT. This proposed solution, illustrated in figure 5.1, involves the development of two modules. A first module in the pre-operative phase, which consists in aligning the pre-operative MR and CT images, aims to improve the precision in PDD estimation as well as the visualization of this dose distribution. During the intervention, a second module aims to accurately align the intra-operative US with the pre-operative MRI in order to improve the visualization during the seeds placement.

The proposed approach is fully automatic in order to save manual labor and therefore facilitate its integration in a clinical workflow. Moreover, the described approach is able to compensate for important prostate deformations which may occur between the acquisitions of the different modalities.

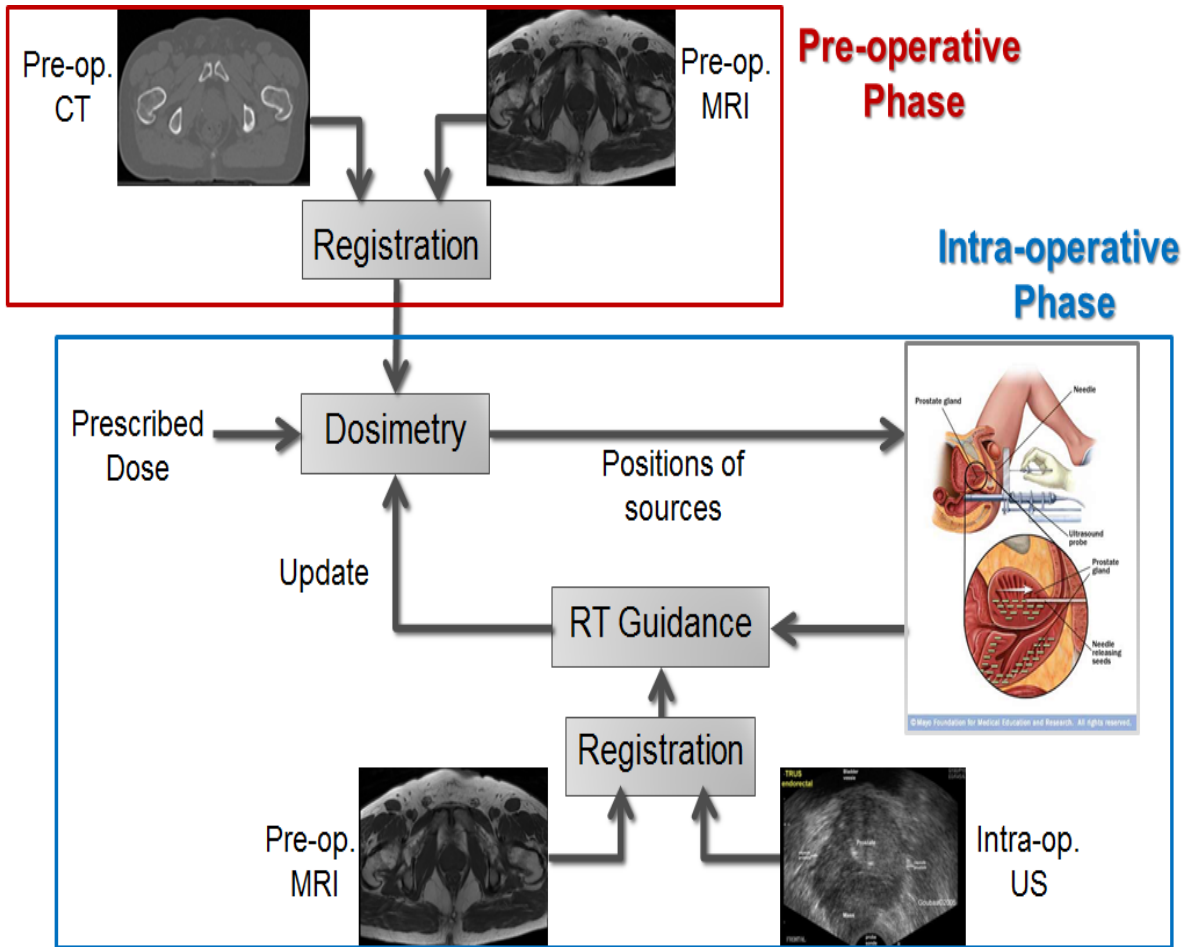


Figure 5.1. The workflow of the proposed approach.

Hereafter, we will discuss the results obtained from both modules during the pre- and intra-operative phases. We will also present solutions to overcome the limitations and the problems that may arise in these proposed approaches. Finally, we will conclude this work and propose some perspectives and future work.

5.1. Pre-operative phase:

In the pre-operative phase of prostate brachytherapy, the dose that needs to be delivered to the tumor is prescribed. Since the treatment efficiency is highly dependent on the treatment planning, an approach to improve the precision of the planning, by providing a personalized and more accurate dose distribution along with a better visualization, is proposed.

This would assist the physician in determining the optimal positions of the radioactive sources in a way that allows the delivery of a maximized dose radiation to the tumor while protecting the surrounding healthy organs at risk.

This proposed approach was focused on the registration of pre-operative MR and CT images. Registration techniques proposed in the literature require generally manual segmentation of the prostate, visual identification of landmarks or markers to be inserted in the prostate. This step can be time consuming and is associated to reduced reproducibility and robustness which in turn may lead to errors in the registration process and, subsequently, to a non-optimal dose estimation.

Considering the computational efficiency, this registration methodology was completed on an average of 2.0 ± 0.25 minutes. Since this registration is done in the pre-operative phase before the intervention, an average of 2 minutes is therefore compatible with clinical settings. The proposed approach was validated on eight clinical patient datasets using both qualitative and quantitative criteria. Considering the absence of a ground truth, the assessment was based on an expert manual segmentation approach. The registration method as well as the manual segmentation were assessed in order to provide relevant associated errors for each step. First of all, a visual inspection of the prostate boundaries' overlap indicated the accuracy of this method where the contours' overlap on both modalities was visually verified and no residual misalignment was found. Quantitative criteria such as the bounding box, the Hausdorff distance and the dice similarity coefficient confirmed the accuracy of the proposed method with a value of mismatch between prostate contours in MR and CT images of 1.15 ± 0.20 mm for all patient datasets considered. As for the dice similarity coefficient, a value of 0.96 ± 0.014 was obtained.

Subsequently, the robustness of the proposed registration method was also evaluated in the presence of changes in the initialization. The registration was performed following CT volume translations and/or rotations of ± 50 mm and $\pm 30^\circ$ respectively, with an associated maximum mismatch between prostate contours in MR and CT images systematically less than 2 mm.

Finally, in terms of reproducibility, two experts were asked to delineate the whole prostate volume on both MR and CT images twice and for all patient datasets. Inter- and intra-observer variability values were subsequently measured in order to determine the errors associated with the manual segmentation step. Considering the intra-observer variability, a mismatch of

1.64±0.79 mm and 2.01±0.68 mm was observed between both segmentations for the first and the second expert respectively. As for the inter-observer variability, the mean mismatch values were 2.19±1.46 mm and 1.93±1.26 mm for the two repeated segmentations performed by the two experts respectively. Overall, there was a trend towards bigger inter-observer variability on the CT images since they are characterized by low soft tissue contrast, which makes it difficult to detect the prostate boundaries (namely the base and the apex) or its interfaces with the surrounding organs.

A study by [1] on prostate volume and localization in MR and CT images showed that a mean volume overestimation of 34% is observed on CT compared with MRI. This was due to a significant difference along the anterior-posterior and superior-inferior direction where the mean prostate volume was 5 mm larger on CT compared to MRI.

Given that such mismatches can occur while delineating the prostate, the manual segmentation approach is not an accurate method for the evaluation of registration related mismatches. On the other hand, the measured errors for the proposed registration methodology were always within the limits of the uncertainties associated with the manual prostate delineation process.

Considering that the registration uncertainty has a significant impact on the calculated dose in brachytherapy, the aim of this work, as previously stated, is to propose an accurate registration method that can improve the overall treatment planning. [2] recently studied the dependence of dosimetry calculation on the registration uncertainty. They found out that the deviation in D90 (the minimum dose delivered to 90% of the prostate volume) is less than 5% for registration errors of less than 2 mm. Given that the residual mismatches using our proposed registration approach were below 2 mm, one could conclude that the proposed methodology can limit dosimetry errors associated with image registration residual mismatches to < 5%. Despite such encouraging results, more patient studies are necessary in order to further assess the reliability of the proposed method before integrating it in a clinical workflow.

Considering the current status in the field, the registration method proposed by [3] had the best performance with a maximum registration error of 2.2 mm. Not only that this method was limited to rigid transformations, but it also required manual identification of anatomic landmarks or implanted markers. Therefore, our fully automatic non-rigid registration method, with a maximum registration error of less than 2 mm, has a superior performance relative to the other methods proposed in the literature.

The proposed registration methodology was a two-step process; with the result of the first affine registration step being used as an initialization for the second non-rigid registration step. Both registration steps were constrained to a different VOI that was determined automatically. Regarding the VOIs determination process, it consisted in detecting the prostate location, based on the anatomy of normal pelvic bones. This automatic determination may be disturbed in cases where the patient has some anomalies such as hip prosthesis for instance. Another limitation could be in cases where the prostate width is bigger than pubic symphysis, and therefore the prostate VOI will not include the whole volume of the prostate. This can be solved by simply enlarging the prostate VOI and making it reaches the ischium. A study with more clinical datasets, including patients with these special cases, will be conducted.

5.2. Intra-operative phase:

During the intra-operative phase, the physician utilizes the US as a real-time guiding system in order to place the radioactive sources in their pre-planned positions. The US image however is not well suited for the visualization of the prostate due to its poor soft tissue contrast which may lead to inaccuracies in the seeds placement. Improving the visualization during these procedures could have a high impact on the overall accuracy of the treatment. An approach, which consists in accurately registering the intra-operative US with the MR images, is proposed to provide a better visualization during the intervention.

Similarly to the pre-operative registration, manual segmentation of the prostate or visual identification of landmarks is generally required in the registration techniques proposed in the literature. This step can be both time consuming and subject to intra- and inter- observer variability inaccuracies depending on the user's experience. A fully automatic non-rigid

registration method is therefore proposed. Moreover, the proposed methodology can compensate for prostate deformations caused by the pressure of the probe and the insertion of the needles. The proposed registration methodology was a two-step process. A first affine registration is applied to globally align the two images and then used to initialize a second non-rigid registration step which is responsible for detecting local deformations of the prostate. A similarity measure called linear correlation of linear combination (LC^2) was used for both steps. This metric has been only explored in neurosurgery applications, where deformations can be negligible. In this work, we used the LC^2 to align prostate images, where important deformations may occur. Moreover, we combined this metric with a multi-resolution approach that has the potential of improving the robustness of the method as well as avoiding local minima. In addition, both registration steps were constrained solely to VOIs determined automatically around the prostate in order to improve the computational efficiency.

The overall computational efficiency of the proposed registration methodology took an average of 2.75 ± 0.25 hours to perform both registration steps on a CPU. To be compatible with a clinical setting, the proposed methodology for the intra-operative phase should be a real-time process. Therefore, a solution on GPU was developed. Considering that the LC^2 metric is calculated on each pixel regardless of the results on other pixels, the registration process can be perfectly parallelized and an approach using GPU has the potential of improving the computational time. A first non-optimal implementation reduced the computational time by a factor of 40. Given the possibility of combining 4 GPUs in the same workstation, this time could be reduced to less than 30 seconds, which is compatible with time constraints in a clinical workflow.

The feasibility of the method was at first tested using prostate phantom, resulting in a registration error of 1.48mm and a DSC value of 0.98. Subsequently, the method was validated using clinical datasets. A visual assessment of prostate boundaries overlap demonstrated the accuracy of the proposed methodology since no significant misalignment was found between prostate contours in the two modalities. The degree of boundaries overlap was also computed quantitatively using the Hausdorff distance and the dice similarity coefficient. A mismatch between prostate contours in both images of 1.44 ± 0.06 mm was found. The DSC also confirmed the accuracy of the proposed method with a value of 0.977 ± 0.006 . In addition, the actual registration mismatch error may be even smaller, given the uncertainties associated with the manual segmentation of the prostate.

Concerning the reproducibility of the method, it was not evaluated for the intra-operative registration. First of all, both modalities were cropped automatically and the manual segmentation was done only in small VOIs around the prostate which facilitated the task. Moreover, the deviation of the mismatch (difference between minimum and maximum value) between prostate contours in both images was not significant (0.5 mm). Therefore, only one segmentation performed by one expert was enough to evaluate the results of this registration. However, a complete evaluation of the inter- and intra-observer variability will be conducted in the future; where we will ask two experts to delineate the prostate twice, and then compare the mismatches from the two segmentations performed by each expert.

The proposed registration methodology was focused on US images without the needles, a registration that takes the needles into account should be therefore proposed. One solution may be to remove the needles from the image by subtracting the image after the insertion from the one before the insertion of needles.

Considering the current state of the art, most of the previously proposed methods have worse, or at best equivalent, performance to that of our proposed approach. The non-rigid registration proposed by [4] resulted in an average RMS registration error of 1.93 ± 0.73 mm. However, a manual initialization, where 3 corresponding landmarks are placed in the two images, was necessary in order to initiate their registration. Therefore, our automatic method, with an average error of 1.44 ± 0.06 mm, has a better performance, considering the current status in the field. Although encouraging results were obtained following our registration methodology, a complete evaluation study using more patients is necessary. Since only three patient clinical datasets were used for validation, a conclusion cannot be made about the ability of the proposed method to align these modalities in a prostate imaging context before further assessing its reliability.

5.3. Conclusion and future work:

A multimodal registration approach for image-guided prostate brachytherapy is presented in this work. This approach can improve the overall accuracy by providing a coherent solution not only in the diagnosis but also in treatment planning and delivery. At first, and during the pre-operative phase, a method that can improve the precision in estimating a PDD is proposed. Another method

was proposed in order to improve the visualization, and therefore the treatment efficiency, during the diagnosis as well as the seeds placement. The described methodologies were fully automatic, where no manual segmentation or visual identification of landmarks is required. Moreover, the proposed methods could compensate for any prostate deformations that can occur during the intervention.

Future work will involve further evaluation of the proposed approach on a larger number of clinical datasets to further assess the reliability and robustness of this solution before integrating it in a clinical workflow. The process of recovering more clinical datasets is ongoing.

Concerning the evaluation of the proposed methodology, an expert manually segmented the images after the affine registration and after the non-rigid registration steps. Therefore, the segmentation was done on one of the two images after applying the transformation which aligns both images. This would introduce a bias on the results considering that if the registration was not good enough then the segmentation process would be difficult. To overcome this limitation, the initial images can be segmented, and then the transformation, which aligns the two images, can be applied on the initial contours to obtain the prostate boundaries on the registered images.

A new method for evaluating registration errors also need to be proposed, considering that the manual segmentation approach is not accurate. This can be done by inserting markers in the patient for example. Another solution would be to simulate the images and introduce a known deformation field which would be compared with the result obtained following the proposed registration methodology.

A few perspectives can be proposed concerning the intra-operative registration. First of all, the segmentation errors in the intra-operative registration need to be evaluated by studying the intra- and inter-observer variability. Moreover, the insertion of the needles needs to be taken into account for the registration. Another perspective would be to use a new US probe allowing the acquisition of more slices, and therefore the visualization in 3D.

Future methodological developments will focus on developing a solution on GPU in order to improve the computational time of the registration, especially the intra-operative US/MRI registration step. An approach using GPU has the potential of improving the computational time, resulting in an almost real-time process that is compatible with time constraints in a clinical

workflow. A first simulation on 2D images was already conducted, where only the LC^2 calculation was implemented on GPU. The calculation of the global LC^2 , for one iteration, took 3.23 seconds on an Intel® Core™ i7-3840QM CPU @ 2.80 GHz. However, implementing this approach on a GPU (NVIDIA TITAN X Pascal) reduced the calculation time to only 80 ms, resulting in a factor of x40. Therefore, by interpolating this factor over the whole registration process, the computational efficiency could be potentially reduced to 3.75 minutes using one GPU. Considering the possibility of using 4 GPUs in a workstation, this calculation time could be therefore reduced to 56 seconds. This first simulation was a non-optimal version of the implementation of LC^2 on GPU; therefore we believe that implementing the whole registration process, and optimizing the code, could improve the computational efficiency by at least a factor of two, resulting in an approach that is compatible with time constraints in a clinical workflow.

Although the proposed solution was dedicated to prostate brachytherapy procedures, our registration framework has potential benefits for a variety of image-guided radiation therapy (IGRT) applications, such as post-implant dosimetry and external beam radiotherapy. In IGRT, CT images are generally used to calculate the dose based on the electron density information. Although CT images provide good contrast for radioactive sources, soft tissues are poorly visualized. MRI, on the other hand, is being increasingly used in IGRT procedures due to its superior soft tissue contrast which allows a distinction between cancerous and healthy tissues. Therefore, a registration between MR and CT images is essential. In addition, in some MRI-guided targeted biopsies, a registration between PET/CT and MR images was proven to give better results than biopsies done under MRI alone [5]. Moreover, in MRI-guided radiotherapy, adaptive planning using a combined MRI-linear accelerator (linac) approach can allow for real time treatment delivery guidance. Nevertheless, dose calculations remain the main challenge here since, unlike CT, image intensity in MRI is not directly related to electron density. Therefore, an accurate MR/CT image registration would facilitate the mapping of electron densities to MRI for dose calculations. Concerning the US/MRI registration, it has a potential benefit for targeted prostate biopsies; which is usually done under the US guidance and therefore this registration is essential in order to improve the visualization. Moreover, in focal therapies of prostate, where the ablation is done under US guidance while the dose planning can be performed on MRI, a registration between US and MR images is also necessary. Finally, the VOIs determination on the US images can be used for applications where prostate segmentation is required. Although the

extracted prostate contours using the proposed method may be sometimes incomplete or even contain extra structures, some model-based segmentation algorithms only require a few points along the prostate contours as initialization, which can be easily determined on the extracted contours following our proposed method.

Image registration is a crucial step in any image-guided intervention. Therefore, the proposed solution can be used not only for prostate applications, but for other organs as well; such as breast and brain cancer for instance. The only change would be the VOIs determination, since our method was based on the anatomy of the pelvis.

Finally, the proposed multimodal registration approach will be combined with dose calculations and a method that automatically determines the positions of the sources to form a complete platform for a new and more precise treatment planning system.

References:

- [1] Sannazzari GL, Ragona R, Ruo Redda MG, Giglioli FR, Isolato G, and Guarneri A (2002). “CT-MRI image fusion for delineation of volumes in three-dimensional conformal radiation therapy in the treatment of localized prostate cancer”. *The British Journal of Radiology*. **75(895)**: 603-7.
- [2] Su Y, Davis BJ, Furutani KM, Herman MG, and Robb RA(2007). “Dosimetry accuracy as a function of seed localization uncertainty in permanent prostate brachytherapy: increased seed number correlates with less variability in prostate dosimetry”. *Physics in Medicine and Biology*. **52(11)**: 3105-19.
- [3] Servois V, Chauveinc L, El Khoury C, Lantoine A, Olivier L, Flam T, Rosenwald JC, Cosset JM, and Neuenschwander (2003) “Comparaison de deux méthodes de recalage d’images de scanographie et d’IRM en curiethérapie prostatique. Intérêt pour l’évaluation thérapeutique”. *Cancer/Radithérapie*. **7(1)**: 9-16.
- [4] Sun Y, Yuan J, Qiu W, Rajchl M, Romagnoli C, Fenster A (2015). “Three-dimensional nonrigid MR-TRUS registration using dual optimization”. *IEEE Transactions on Medical Imaging*. **34(5)**: 1085-95.
- [5] Piert M, Montgomery J, Kunju LP, Siddiqui J, Rogers V, Rajendiran T, Johnson TD, Shao X, and Davenport MS (2016). “¹⁸F-Choline PET/MRI: The Additional Value of PET for MRI-Guided Transrectal Prostate Biopsies”. *Journal of Nuclear Medicine*. **57(7)**: 1065-70.

List of figures

1.1. New cases diagnosed with cancer in Europe in 2012	1
1.2. The prostate (a) anatomy, (b) zones of the prostate	2
1.3. Prostate biopsy (a) transrectal approach, (b) needle trajectory in TRUS	5
1.4. Prostate biopsy using transperineal approach	5
1.5. Truebeam TM , a linear accelerator used for EBRT	8
1.6. Prostate radiotherapy using 7 beams	8
1.7. Radioactive sources used in brachytherapy	12
1.8. Needle insertion in brachytherapy using (a) TRUS, (b) the template	14
1.9. Clinical workflow of prostate brachytherapy	15
1.10. (a) CT and (b) TRUS images of the prostate	16
1.11. MRI of the prostate	16
1.12. The workflow of the proposed approach	17
1.13. Prostate deformations caused by needle insertion and TRUS probe pressure	18
2.1. Image registration	24
2.2. Classification of registration methods	25
2.3. Components of registration	28
2.4. Global workflow of the proposed MRI/CT registration method	34
2.5. Pelvis bones	35
2.6. MIP projection according to (a) x direction, (b) y direction and (c) z direction	36
2.7. MIP, (a) after thresholding, (b) after opening operation	37
2.8. (a) MIP containing a line connecting the two tips, (b) extracted CT slice	37
2.9. Thresholding of the extracted slice, (a) original image, (b) binary image	38
2.10. Pelvic ROI, (a) in the binary image, (b) original image	39
2.11. Prostate ROI, (a) in the binary image, (b) original image	39

2.12. Parzen windowing	42
2.13. 2D B-Spline, (a) B-Spline grid, (b) deformation vectors, (c) deformation field	43
2.14. Types of resampling, (a) forward, (b) inverse mapping	45
2.15. GUI showing MRI after MRI/CT registration	47
2.16. Placing sources on the MRI	47
2.17. Isodose lines on the MRI	48
3.1. Overview of the GMM-FEM method	56
3.2. Generating optimal correspondences in different resolutions	57
3.3. Overview of the method including MRI and TRUS segmentation, and MRI/TRUS fusion	58
3.4. The 3D shape-context spherical neighborhood	59
3.5. Global workflow of the proposed US/MRI registration method	61
3.6. TRUS image containing the grid	62
3.7. TRUS image after the preprocessing	63
3.8. Prostate VOI (a) on the CT, and (b) on the MRI	63
3.9. Bas-relief, (a) original image, (b) result of bas-relief	64
3.10. Types of offset, (a) bas-relief method, (b) RBR method	65
3.11. (a) The inverted image, (b) the result of RBR	66
3.12. RBR image, (a) after thresholding, (b) after boundaries smoothing	66
3.13. (a) Inverted image, (b) prostate boundaries	67
3.14. Prostate VOI on the US	67
3.15. LC^2 , (a) US, (b) MRI and (c) MRI gradient	68
3.16. Simplex method	71
3.17. Multi-resolution approach on 3 levels	72
3.18. Streaming multiprocessors	75
3.19. (a) Execution of a typical CUDA program, and (b) CUDA thread, block and grid	76
4.1. Prostate phantom model built using Blender, (a) 3D mold, (b) one half of the mold	82
4.2. Prostate MRI phantom model	83
4.3. MRI (T1) of the prostate phantom	83
4.4. The printed prostate phantom model to the right, and the mold made of plaster to the left	84
4.5. US phantom showing the prostate, the urethra, and the rectum wall	85
4.6. US prostate phantom showing two holes representing the rectum and the urethra	85

4.7. US image of the prostate phantom	86
4.8. Mutual information values at each iteration of the optimizer, during the affine registration, using different step values	91
4.9. Mutual information values at each iteration of the optimizer, during the non-rigid registration, using different factor values	91
4.10. Mutual information values at each iteration of the optimizer during the affine registration step	92
4.11. Mutual information values at each iteration of the optimizer during the non-rigid registration step	92
4.12. Checkerboard showing prostate contours on MR and CT images, (a) after affine registration, (b) after non-rigid registration	93
4.13. Checkerboard showing prostate contours on MR and CT images, (a) after affine registration, (b) after non-rigid registration	93
4.14. Checkerboard showing prostate contours on MR and CT images in sagittal view, (a) after affine registration and (b) after non-rigid registration	94
4.15. Box plots representing the 2D Hausdorff distances between prostate contours in MR and CT images following the affine registration step	96
4.16. Box plots representing the 2D Hausdorff distances between prostate contours in MR and CT images following the non-rigid registration step	97
4.17. DSC values between prostate contours in MR and CT images	98
4.18. VOIs determination on CT, (a) pelvic VOI and (b) prostate VOI	100
4.19. Box plots representing 3D Hausdorff distances between prostate contours in MR and CT images	101
4.20. Checkerboard showing prostate contours on US and MR phantom images after non-rigid registration	102
4.21. Checkerboard showing prostate contours on US and MR images after non-rigid registration using mutual information	103
4.22. LC^2 values at each iteration of the optimizer, during the affine registration, using different patch size values	104
4.23. LC^2 values at each iteration of the optimizer, during the affine registration, using different simplex size values	105
4.24. Checkerboard showing prostate contours on US and MR images (a) after affine registration, (b) after non-rigid registration	106
4.25. Box plots representing the 2D Hausdorff distance between prostate contours in US and MR images following the affine registration step	107
4.26. Box plots representing the 2D Hausdorff distance between prostate contours in US and MR images following the non-rigid registration step	108
4.27. DSC values between prostate contours in US and MR images	109
4.28. Prostate VOIs on (a) MR and (b) US images	109

4.29. (a) Prostate boundaries, (b) prostate VOI on US 110

4.30. Checkerboard showing prostate contours on US and CT images after the final registration step 111

5.1. The workflow of the proposed approach 116

List of tables

2.1. Hounsfield units	38
3.1. Parallelism in CPUs and GPUs	74
4.1. Dimensions of MRI/CT datasets of the patients	87
4.2. Dimensions of US/MRI datasets of the patients	87
4.3. Characteristics of bounding boxes enclosing the prostate in MRI and CT	95
4.4. Characteristics of bounding boxes enclosing the prostate in US and MRI.....	107

List of abbreviations and acronyms

PCa prostate cancer

DRE digital rectal examination

PSA prostate-specific antigen

TRUS transrectal ultrasonography

MRI magnetic resonance imaging

MpMRI multiparametric magnetic resonance imaging

DCE dynamic contrast-enhanced

DWI diffusion-weighted imaging

EBRT external beam radiation therapy

Linac linear accelerator

CT computed tomography

ADT androgen deprivation therapy

HIFU high-intensity focused ultrasound

FLA focal laser ablation

PDT photodynamic therapy

LTIT laser interstitial thermo therapy

HDR high dose rate

LDR low dose rate

AAPM American association of physicists in medicine

TG task group

IGRT image-guided radiation therapy

PDD personalized dose distribution

US ultrasound

ROI region of interest

DoF degrees of freedom

SSD sum of square differences

CC correlation coefficient

PDF probability density function

MI mutual information

ICP iterative closest point

MRSI magnetic resonance spectroscopic imaging

TPS this-plate spline

RMS root mean square

FoV field of view

MIND modality independent neighborhood descriptor

TRE target registration error

FEM finite element modeling

VOI volume of interest

MIP maximum intensity projection

HU Hounsfield units

KDE kernel density estimation

GUI graphical user interface

GPU graphics processing unit

GGEMS geant4-based Monte Carlo simulations

FRE fiducial registration error

GMM Gaussian mixtures model

EM expectation-maximization

PCA principal component analysis

RPM robust point matching
SDM statistical deformation modeling
FEA finite element analysis
SSM statistical shape modeling
LC² linear correlation of linear combination
RBR radial bas-relief
CR correlation ratio
CPU central processing unit
SM streaming multiprocessor
SP stream processor
CUDA compute unified device architecture

TMM tissue mimicking material
PVC polyvinyl chloride
d_H Hausdorff distance
DSC dice similarity coefficient

List of publications

National conferences:

- I. Hamdan et al. “3D MRI/CT non-rigid registration for image-guided prostate brachytherapy” Surgetica’2014: Computer-Assisted Medical Interventions: scientific problems, tools and clinical applications. 201-203.

International conferences:

- I. Hamdan et al. (2015) “3D MRI/CT Non-rigid Registration for Image-guided Prostate Brachytherapy” Computer Assisted Radiology and Surgery. 10(1): S12-S15.
- I. Hamdan et al. (2016) “Non-rigid MRI/CT Registration for Effective Planning of Prostate Brachytherapy” IEEE Engineering in Medicine and Biology Society. 1155-1158.

Journals:

- I. Hamdan et al. “Fully automatic deformable registration of preoperative MRI/CT for image-guided prostate brachytherapy” Medical Physics. (Accepted)
- I. Hamdan et al. “Fully automatic non-rigid US/MRI registration for image-guided prostate brachytherapy” Physics in Medicine and Biology. (Submitted)

Le cancer de la prostate est le cancer le plus fréquent chez l'homme en France et aux pays occidentaux. Il est la troisième cause de décès liés au cancer, étant responsable d'environ 10% des morts. La curiethérapie, une technique de radiothérapie, est liée à une meilleure qualité de vie après le traitement, par rapport aux autres méthodes de traitement. La curiethérapie de la prostate consiste à insérer des sources radioactives dans la prostate afin de délivrer une dose d'irradiation localisée à la tumeur tout en protégeant les tissus sains environnants. L'imagerie multimodale est utilisée afin d'améliorer la précision du traitement. Les images Tomodensitométriques préopératoires, appelées Computed Tomography (CT), peuvent être utilisées pour calculer une distribution personnalisée et plus précise de dose. Pendant l'intervention, le chirurgien utilise un système de guidage temps-réel par l'Ultrason Transrectale, Transrectal Ultrasound (TRUS), pour placer correctement les sources radioactives dans leurs positions souhaitées. Par conséquent, si les positions des sources sont déterminées sur l'image CT, elles doivent être transférées à l'image US. Cependant, un recalage US/CT direct et robuste est difficilement envisageable parce que les tissus mous, telle que la prostate, offrent peu de contraste en CT et en US. En revanche, l'Imagerie par Résonance Magnétique (IRM) fournit un meilleur contraste et peut, potentiellement, améliorer le traitement en améliorant la visualisation. Donc, ces trois modalités (IRM, CT et US) doivent être correctement alignées. Pour compenser les déformations de la prostate, due au changement de taille et forme entre les différentes acquisitions, un recalage non-rigide est nécessaire. Une méthode de recalage entièrement automatique est nécessaire, afin de faciliter son intégration au bloc opératoire. Nous proposons dans un premier temps un recalage IRM/CT basé sur la maximisation de l'information mutuelle en combinaison avec un champ de déformation paramétré par B-Splines. Nous proposons de contraindre le recalage sur des volumes d'intérêt (VOIs) afin d'améliorer la robustesse et le temps de calcul. L'approche proposée a été validée sur des jeux de données cliniques. Une évaluation quantitative a montré que l'erreur de recalage est égale à 1.15 ± 0.20 mm; qui répond à la précision clinique souhaitée. Ensuite, nous proposons un deuxième recalage US/IRM, où nous utilisons une approche multi-résolution pour éviter les minima locaux et améliorer le temps de calcul. Un critère de similarité, qui met en corrélation l'intensité de l'image US avec l'intensité ainsi que le gradient de l'image IRM, a été utilisé afin de trouver la transformation qui aligne les deux images. Cette méthode a été validée sur un fantôme de prostate dans un premier temps pour évaluer sa faisabilité. Ensuite, elle a été validée sur des jeux de données cliniques en utilisant des critères qualitatifs et quantitatifs. La distance Hausdorff a montré que l'erreur de recalage est égale à 1.44 ± 0.06 mm. L'approche proposée dans ce travail permet d'aller vers un protocole de curiethérapie guidée par l'imagerie multimodale qui puisse améliorer la précision globale de cette procédure. Malgré ces résultats plutôt encourageants, les travaux futurs impliqueront une évaluation plus approfondie sur plus de jeux de données afin d'évaluer la fiabilité et l'efficacité de cette méthode avant de l'intégrer au bloc opératoire.

Mots clef : Curiothérapie, Prostate, Imagerie multimodal, Recalage d'images

Prostate cancer is the most common cancer in men in France and western countries. It is the third leading cause of death from cancer, being responsible for around 10% of deaths. Brachytherapy, a radiotherapy technique, is associated with a better health-related quality of life after the treatment, compared to other treatment techniques. Prostate brachytherapy involves the implantation of radioactive sources inside the prostate to deliver a localized radiation dose to the tumor while sparing the surrounding healthy tissues. Multi-modal imaging is used in order to improve the overall accuracy of the treatment. The pre-operative Computed Tomography (CT) images can be used to calculate a personalized and accurate dose distribution. During the intervention, the surgeon utilizes a real-time guiding system, Transrectal Ultrasound (TRUS), to accurately place the radioactive sources in their desired pre-planned positions. Therefore, if the positions of the sources were determined on CT, they need to be transferred to US. However, a robust and direct US/CT registration is hardly possible since they both provide low soft tissue contrast. Magnetic Resonance Imaging (MRI), on the other hand, has a superior contrast and can potentially improve the treatment planning and delivery by providing a better visualization. Thus, these three modalities (MRI, US and CT) need to be accurately registered. To compensate for prostate deformations, caused by changes in size and form between the different acquisitions, non-rigid registration is essential. Fully automatic registration methodology is necessary in order to facilitate its integration in a clinical workflow. At first, we propose a registration between pre-operative MR and CT images based on the maximization of the mutual information in combination with a deformation field parameterized by cubic B-Splines. We propose to constrain the registration to volumes of interest (VOIs) in order to improve the robustness and the computational efficiency. The proposed approach was validated on clinical patient datasets. Quantitative evaluation indicated that the overall registration error was of 1.15 ± 0.20 mm; which satisfies the desired clinical accuracy. Then, we propose a second intra-operative US/MRI registration, where a multi-resolution approach is implemented to reduce the probability of local minima and improve the computational efficiency. A similarity measure, which correlates intensities of the US image with intensities and gradient magnitude of the MRI, is used to determine the transformation that aligns the two images. The proposed methodology was validated on a prostate phantom at first to assess its feasibility. Subsequently, the method was validated on clinical patient datasets and evaluated using qualitative and quantitative criteria, resulting in a registration error of 1.44 ± 0.06 mm. The approach proposed in this work allows going towards a multimodal protocol for image-guided brachytherapy which can improve the overall accuracy of this procedure. Despite such encouraging results, future work will involve further evaluation on a larger number of datasets in order to assess the reliability and the efficiency of this methodology before integrating it in a clinical workflow.

Keywords: Brachytherapy, Multimodal Imaging, Image Registration